Università degli Studi di Napoli "Federico II"

PhD in Novel Technologies for Material, Sensors and Imaging

Cycle XXVIII

Research and development of a pioneering system for single photon detection: the VSiPMT

Supervisors:
Prof. G. Barbarino
Dott. F. Di Capua

PhD Candidate:
Felicia Carla Tiziana Barbato

Years 2013-2016

Contents

Introduction

Photon detection is a key factor to study many physical processes in several areas of fundamental physics research (i.e. particle and astroparticle physics, biomedicine) as well as industrial application (i.e. medical equipment, environmental measurement equipment, quantum computing and oil well logging).
Different photon detection strategies are required for such a wide range of applications and, as a consequence, different classes of devices on the market.
In the astroparticle physics experiments panorama, PMTs hold the stage. The PhotoMultiplier Tubes are a one-century old technology which detection capabilities seem to be unrivalled up to now. These devices, neverthless, suffer of some intrinsic drawbacks that are independent on the technological progress and that impose a limit on the achievable perfomances.
On the other side, the future generation of experiments will require further improvement in linearity, gain, and sensitivity (quantum efficiency and single photon counting capability).
So, even though PMTs represents a cerified technology since 1936, an alternative solution should be found.
The solid state photodetectors, APDs and SiPMs, represent a technological progress that goes beyond PMTs' limits. In particular, SiPM technology has achieved a very high level of performances, but the size limited by the thermal noise partially compromises their application in astroparticle physiscs experiments.
A big challenge is, therefore, to find a way to use SiPMs to detect photons from large surfaces and/or volumes, as typically needed in many astroparticle physics experiments.
In this scenario an appealing solution is represented by the Vacuum Silicon PhotoMultiplier Tube. The VSiPMT is an original design for an innovative light detector invented in Naples to enlarge indirectly the SiPM sensitive surface and so to overcome the PMTs limits.
The VSiPMT is based on the combination of a SiPM with an hemispherical

PMT standard envelope.
The main idea is to replace the classical dynode chain of a PMT with a SiPM, the latter acting as an electron multiplier at low voltage.
The project started with a hard preliminary work aimed at prooving the feasibility of the device, the results obtained convinced Hamamatsu Photonics, world leader company in PMT and SiPM manufacture, to realize for us two prototypes of the device.
The results obtained by the characterization of the two industrial prototypes were so encouraging that leads to the realization of a larger and usable prototype.
In this thesis all the phases of the VSiPMT project are described, with a particular focus on the industrial prototypes characterization phase and on the realization of the larger prototype.
The thesis is organized in five chapters. The first one contains a state of the art about light detection technologies for astroparticle physics experiments. The second chapter is dedicated to the VSiPMT description. The third chapter contains a summary of the preliminary work done to proove the feasibility of the device and an accurate description of the VSiPMT industrial prototypes including the results obtained in the characterization phase. The fourth chapter includes the description of the engineering studies for the realization of a new generation of VSiPMT prototypes with a larger photocathode area, the chapter is organized in three main topics: optimization of the focusing, selection of the SiPM and study and realization of a transmission mode photocathode. In the last chapter there is a description of the pre-prototype obtained assembling the single parts mentioned in the previous chapter. The pre-prototype characteristics have been tested at the DaΦne Light Facility at LNF and then analyzed. Futher improvement are proposed at the end of the chapter.

Chapter 1

Photon detectors

The photodetectors are devices used to detect light. They are widely used in many areas of fundamental physics research (i.e. astroparticle physics, nuclear and particle physics) as well as in medical equipment and check-ups (i.e. PET, Radioimmunoassay and Enzyme immunoassay as luminescent, fluorescent, Chemiluminescent Immunoassay) and even in everyday stuff (Fiberoptics communication, Remote sensing for security and safety, Environmental sensing for pollution detection, Defence).
Depending on the application, a photodetector has to fulfill various requirements:

- it must be sensitive in some given spectral region. In some cases, the responsivity should be constant or at least well defined within some wavelength range. It can also be important to have zero response in some other wavelength range; an example are solar-blind detectors, being sensitive only to short-wavelength ultraviolet light but not to sun light;
- the detector must be suitable for some range of optical powers. The maximum detected power can be limited e.g. by damage issues or by a nonlinear response, whereas the minimum power is normally determined by noise. The dynamic range is often very important;
- the active area of a detector can be important e.g. when working with strongly divergent beams from laser diodes;
- the detection bandwidth may begin at 0 Hz or some finite frequency, and ends at some maximum frequency which may be limited by internal processes (e.g. the speed of electric carriers in a semiconductor material) or by the involved electronics (e.g. introducing some RC time constants);

- the time precision is an important requirement in the detection of pulses of light (possibly on a few-photon level). Some detectors have a certain "dead time"after the detection of a pulse, where they are not sensitive;
- different types of detectors require more or less complex electronics. Penalties in terms of size and cost may result;
- for some applications, one-dimensional or two-dimensional photodetector arrays are needed. For detector arrays, some different aspects come into play, such as dead areas and read-out techniques;
- the size, robustness and cost are essential for many applications.

As the range of application and thus the requirements vary considerably, there are many types of photodetectors which differ in many of these properties and which may be appropriate in a particular case. However, in typical application scenarios, some requirements totally rule out the use of certain detector types, and quickly lead to a fairly limited choice.
Now we will focus the attention on astroparticle physics applications and so we will analyse the mostly used categories of photodetectors in this field: the vacuum tubes, the solid state photodetectors and the hybrid photodetectors.

1.1 Vacuum Tubes: the PMTs

The photomultiplier tube, also known as PMT, is one of the oldest photodetector. Its birth dates back to the first decades of the last century, when Iams in 1935 [1] and Zworykin in 1936 [2] realized respectively the first phototube with a single amplification stage and the first one with a multiple amplification stage.
It consists in a vacuum glass envelope, a photocathode and a multiplication stage, see fig. 1.1.

The working principle of a PMT is the photoelectric effect linked to an amplification stage [3].
The light absorbed on the photocathode generates, by photoelectric effect, free electrons [4], [5] . Some focusing rings (with a potential difference set to hundreds of volts) generate an electric field in which the photoelectrons are accelerated and guided to the amplification stage.
In such a device the amplification stage consists of a series of electrodes each supplied by a voltage that is higher with respect to the one of the next electrode. This electrodes series is generally called dynode chain.
When the photoelectron hit the first dynode it extracts a certain number

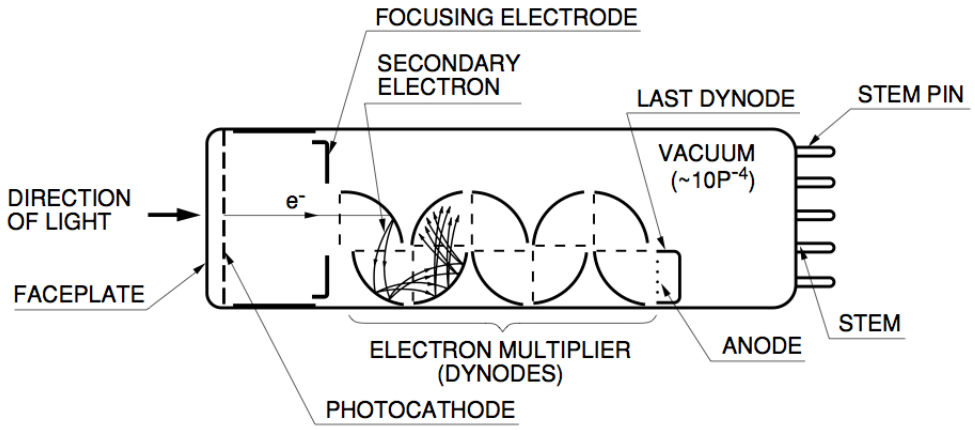

Figure 1.1: *Schematic view of a PMT. The incident light on the left impinges on the photocathode and by photoelectric effect it's converted in electrons. The primary electron coming from the conversion of a photon, is then accelerated and driven to the first dynode by an electric field. When the primary electron hit the dynode surface, it extracts a certain number of secondary electrons, and so on through the whole dynode chain. Finally all the secondary electrons produced in the dynode chain are collected by an anode and readout as electric signal.*

$\delta = kV_d$ of seconday electrons, this number is proportional to the accelerating voltage, V_d, of the primary electron. This process is repeated in the next dynodes. Due to this avalanche process, the detected photocurrent can be orders of magnitude higher than the one exiting from the photocathode. Ideally, the current amplification or gain of a photomultiplier tube, having the number of dynode stages n and the average secondary emission ratio δ, will be δ^n. Therefore, photomultipliers can be used for, e.g., single photon counting and can be highly sensitive detectors with high bandwidth ($> 1GHz$), and good linearity in a wide dynamic range [6].

1.1.1 Limits on performances

To date the PMTs are the most widely used in many particle physics experiments, showing apparentely unrivalled detection capabilities.
Neverthless it suffers of many drawbacks [6], [7], such as:

- fluctuations in the first dynode gain make single photon counting difficult;

- the linearity is strongly related to the gain and decreases as the latter increases;
- the transit time spreads over large fluctuations;
- the mechanical structure is complex and expensive;
- they are sensitive to the magnetic fields;
- the need of voltage dividers increases failure risks, complexity in the experiments designs and power consumption.

Multiplication noise
As said above, the amplification stage of a PMT consists of a series of dynodes. When the photoelectron hits the first dynode it can extract an average number of secondary electrons equal to δ. For every dynode there is a statistical spread in secondary emission coefficient around the mean value δ. The statistical effect is of greatest importance at the first dynode, d_1, more than at any subsequent dynode. This is because the number of secondary

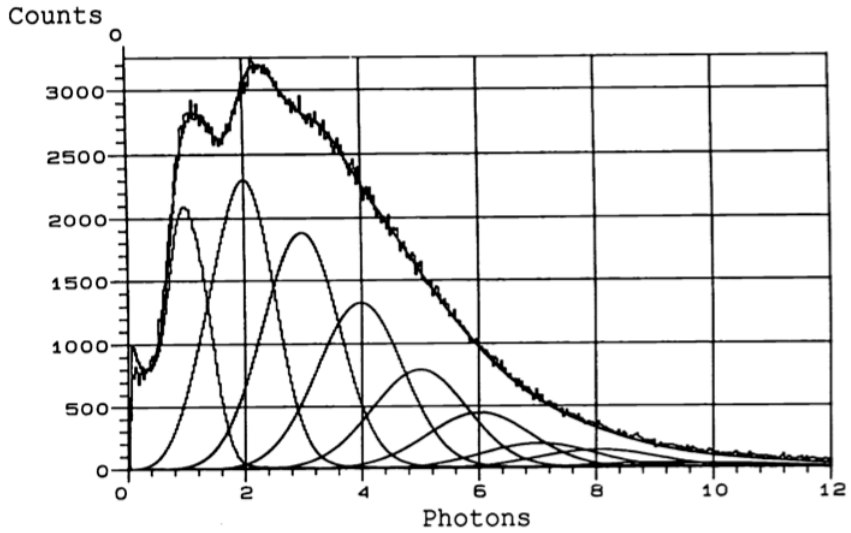

Figure 1.2: *A typical PMT signal. In PMTs the gain is obtained by placing the electrodes, the dynodes, in series. This kind of structure allows the fluctuations on the first dynode to propagate through the whole dynode chain. This produce an increase of the noise that results in a complicated photon counting.*

electrons, N, is relatively small at d_1 and hence subject to high fluctuation,

proportional $\sqrt{1/N}$. Thus, as the cascade develops in the dynode chain, it soon becomes statistically well defined since N increases quickly at each multiplication step. The fluctuations in the first dynode make the signal-to-noise ratio very low, therefore the output signal will be the convolution of many different gaussians (each corresponding to a certain number of photoelectrons) causing a complication in the photon counting, see fig. 1.2.

Linearity
In PMTs two kinds of linearity can be defined: the charge linearity is the ratio of the number of incident photons to the number of electrons collected at the anode; the current linearity is the proportionality between incident flux and anode current. As clear, in such a device linearity and gain are strictly connected. Limits on both charge and current linearity are set by internal and external factors.

Internal factors affecting linearity

- **Space Charge:** At high currents, space charge can influence the electron trajectories, causing collection losses; at still higher currents it can cause some electrons to return to the surfaces from which they originate. To avoid space charge formation the field between the next-to-last dynode and the anode is 3 to 5 times lower than that between the other dynodes. On the other side, a lower electric field in the last stage sets the limit for current linearity.

- **Cathode Resistivity:** The focusing system is designed on the assumption that the photocathode is an equipotential surface. Any departure from that condition is likely to alter the electron trajectories and affect the collection efficiency of the first dynode. This is what can happen, at least in the case of semitransparent bialkali cathodes having no underlying conductive layer, when the cathode current is too large in relation to the surface resistivity.

- **Gain Drift:** The gain may undergo more or less reversible variations when the mean anode current varies. Although also this constitutes a linearity error.

External factors affecting linearity

- **Power Supply Stability:** Changes in inter-electrode voltages affect gain by influencing the dynode secondary emission factors and the electron trajectories.

- **Divider Current:** When the electrode voltages are derived from a resistive divider across a stabilized power supply, the anode current tends to decrease the potential between the last dynode and the anode. This upsets the voltage distribution throughout the divider and causes an increase of gain comparable to what would be caused by increasing the high voltage by the same amount.

Transit Time Spread

PMTs time response depends on electron trajectories within the tube. Photoelectrons follow individual paths from the photocathode to the first dynode, depending on their point of origin and on their emission velocities. It follows that they land on the first dynode at different points and at different times. Secondary electrons, as a consequence, travel individual paths between dynodes, causing further time dispersion.
The time between the arrival time of a light pulse and that of the PMT output signal is called *transit time*. Because of the different paths followed by the primary and secondary electrons within the tube, the transit time has a spread depending on three architectural features of the device:

1. **The number of dynodes**. It's trivial to understand that the lower is the number of dynodes and the better is the timing.

2. **The photocathode diameter**. The higher is the size difference between the photocathode and the first dynode, the more different are the photoelectron paths. This point gives the main contribution to the spread in time.

3. **The overall voltage**. The higher is the electric field the faster are the electrons, thus reducing the spread in time. The best timing is obtained with a higher voltage between the photocathode and the first dynode, considering that, as said above, in this region the electron paths can be strongly different.

As clear from this quick analysis, the main limits on the PMTs performances are due to the dynode chain. So, even though PMTs represents a certified technology since 1936, it should be highlighted that the presence of the chain, and so of a serial-gain concept, leads many detriments, and so an alternative solution can be found.

1.2 Solid State Photodetectors: APDs and SiPMs

A considerable alternative to PMTs are the solid-state photodetectors, a new constantly developing technology. These devices differ from the vacuum tubes because of the working principle. In this case, the amplification mechanism occurs within a solid-state (semiconductor) material, rather than in a vacuum tube [8], [9], [10].
Currently the most used are the APDs, *avalanche photodiodes*, and the SiPMs, *Silicon PhotoMultipliers*.

1.2.1 Avalanche Photodiodes: gain concept

APDs are high-speed and high sensitivity silicon devices. These features make APDs a suitable device for a wide variety of applications requiring a high sensitivity also in low level light detection [11].
Such a device consists of a *pn* junction with a reverse bias voltage which allows to activate an internal avalanche mechanism who determines the gain. Photons entering an APD generate electron-hole pairs if their energy is higher than the band gap energy ($\sim 1.12\,eV$ at room temperature) [12]. When the

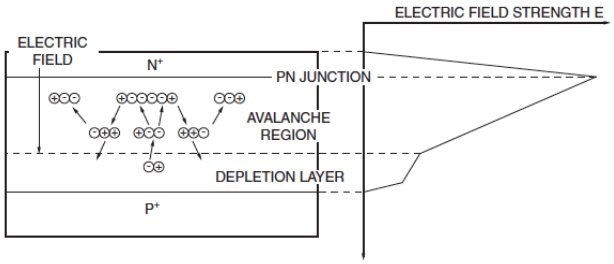

Figure 1.3: *A schematic diagram of the avalanche process in an APD. An electron-hole pair created in the depletion region cross the Silicon bulk with a high energy given by the reverse bias voltage. The carriers can consequently create additional electron-hole pairs giving rise to an avalanche process which generates an output signal proportional to the amount of incident light.*

electron-hole pairs are generated in the depletion layer of a photodiode, the electrons drift towards the N region, while the holes drift towards the P region because of the electric field generated by the reverse voltage. The drift speed depends on the electric field strenght and, thus, on the reverse voltage.

If the carriers speed is high enough they gain a great energy. When these carriers hit the Silicon crystal lattice, ionization in which new electron-hole pairs are generated takes place. The latters can create additional electron-hole pairs starting an avalanche process, see fig. 1.3.
As said above, the APD internal gain depends on the electric fields strenght. The higher is the reverse bias voltage, the higher is the internal gain. However, the APD has a maximum gain whose value depends on the photocurrent. As the internal gain introduces only a multiplication factor, the output signal will be proportional to the amount of light entering the Silicon bulk.

1.2.2 Avalanche Photodiodes: limits on performances

Also the APD shows some drawbacks:

- **Low gain**. The internal gain of APDs is limited to ~ 100. The limit come from the photocurrent. Indeed, if the reverse bias voltage is increased too much, a voltage drop occurs because the current flows through the device resistance, producing a decrease in the voltage applied to the avalanche layer. So, when the APD is operated in a region near the maximum gain, the voltage drop tends to increase, resulting in an unwanted phenomenon in which the output photocurrent is not proportional to the amount of incident light.

- **Gain depends on the temperature**. The gain at a certain reverse voltage becomes small as the temperature rises. This is because the silicon crystal lattice vibrates more heavily with an increasing temperature. As a consequence, the accelerated carriers tend to hit the crystal lattice before reaching an energy level sufficient to start the ionization. To obtain a constant output, it is necessary to adjust the reverse voltage according to the temperature variations or to keep the APD temperature constant.

- **Noise**. APDs generates noise in the multiplication process, there are some statistical fluctuations due to non-uniformities in the ionization. These fluctuations in the multiplication process, called *excess noise*, increase as the gain is increased. Since the gain exhibits a dependence from the energy of the incoming photon, and thus from its wavelenght, the excess noise differs according to the incident light wavelenght. At the same time, the photocurrent generated by a light pulse is also amplified by the gain. All these facts are clear indication that best signal-to-noise ratio exists only for certain gain values.

1.2.3 Silicon PhotoMultipliers: gain concept

The SiPM technology offers a highly attractive alternative that closely mimics the low light detection capabilities of the PMT and at the same time also all the benefits of a solid-state device, like low bias voltage operation, insensitivity to magnetic fields, mechanical robustness and excellent uniformity of response.
The SiPM turns up as a matrix in which each pixel is an APD operating in Geiger mode [13].
When photons enter into the depletion region of the silicon, they can produce an electron-hole pair, where a sufficiently high electric field ($> 5 \times 10^5\, V/cm$) is generated. The carriers created in this region will be accelerated to a point where they carry sufficient kinetic energy to create secondary charge pairs through a process called *impact ionization*. In this way, a single photoelectron can trigger an self-perpetuating ionization cascade that will spread throughout the silicon volume subjected to the field. The silicon will break down and become conductive, effectively amplifying the original photoelectron into a macroscopic current flow. This phenomenon is called *Geiger discharge*. In this configuration the gain of each pixel is $\sim 10^6$ and is constant regardless the number of photons hitting the pixel. This means that each pixel gives informations only on whether or not it has been fired. A quenching resistor is connected to the single pixel to allow the current to flow through it. All the pixels are connected in parallel. This means that in SiPMs only one readout channel is present and the output signal is given by the sum of the signals coming from the single pixels. A typical SiPM spectrum is shown in fig. 1.4. Looking at the figure 1.4 it's easy to notice the differences with a PMT spectrum (fig. 1.2). SiPMs exploit a new concept gain that is given by the connection of the pixels in parallel. In this case, there are no fluctuations propagating in the device and so the multiplication noise is close to zero, thus allowing to obtain very well separeted peaks.

1.2.4 Silicon PhotoMultipliers: limits on performances

Despite of the great benefits in single photon resolution caused by the new gain concept, also this device presents some drawbacks:

- **The dark noise**. As they are solid-state devices, SiPMs generate noise due to thermal excitation, the *dark counts*. Because they work in Geiger-mode also the noise is amplified at the same way of a photon signal, preventing the noise discrimination. The dark counts in SiPMs

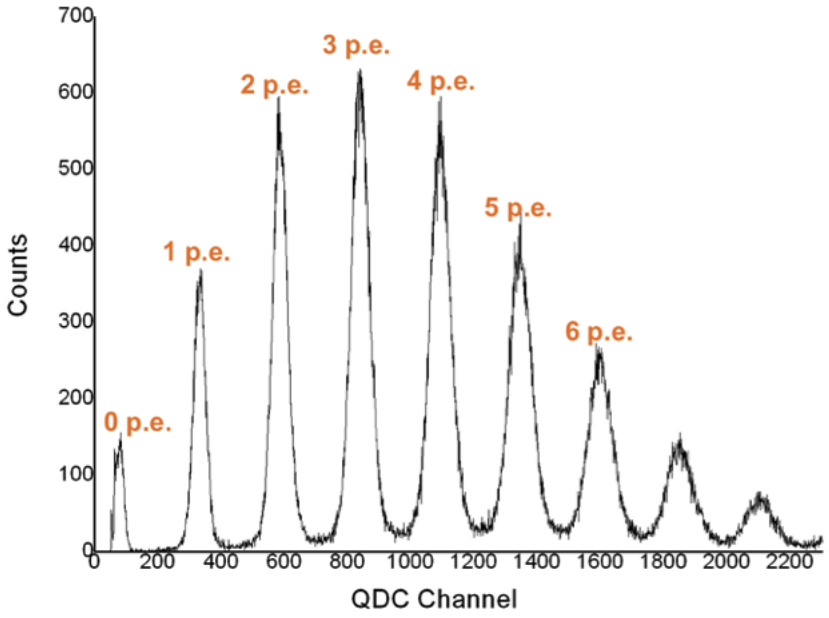

Figure 1.4: *A typical SiPM spectrum. The connection of the pixels in parallel allows to obtain well separated peaks, thus simplifying the photon counting.*

turn up as pulses of 1 p.e.[1]. The opposite is also true, currently the average behaviour is that for every 10°C reduction in device temperature, there is a 50% decrease in the dark count rate.

- **Gain depends on temperature.** An increase in temperature will increase the lattice vibrations of the Silicon. Consequently, the main carriers have a higher probability to hit the crystal before of gaining the right energy to start the Geiger avalanche. Thus, the breakdown voltage changes as a function of temperature and this will result in a change in the gain. It follows that for stable operation the detector should have its temperature regulated, if possible, or the bias voltage needs to be adjusted in order to mantain a constant over-voltage with respect to the altered breakdown voltage.

- **The size.** The SiPM size is limited by the dark noise. The thermal noise increases as the area increases, a good compromise between size

[1]p.e. is the acronym for *photon equivalent*. So 1p.e. corresponds to 1 fired pixel, 2p.e. corresponds to 2 fired pixels and so on.

and dark noise should be taken to obtain a device with reasonably good detection characteristics. Typical SiPMs sizes range between $1\,mm^2$ up to $16\,mm^2$.

This class of detectors will be the center of this thesis and so it will be object of additional discussions in the next chapters.

1.3 Hybrid Tubes: the HPDs

The Hybrid PhotoDetector, HPD, is a fusion of two preexisting technologies: the PMT and the APD [14].
Its structure is similar to PMTs, it has: a vacuum glass envelope, a photocathode to detect light and an electron multiplier.
At the same time, it differs from a PMT because of the operating principle. As said before, in a PMT the electron multiplier is the dynode chain and the multiplication occurs in series. In an HPD, instead, the dynode chain is replaced by an APD, see fig. 1.5. Recalling what already said in section

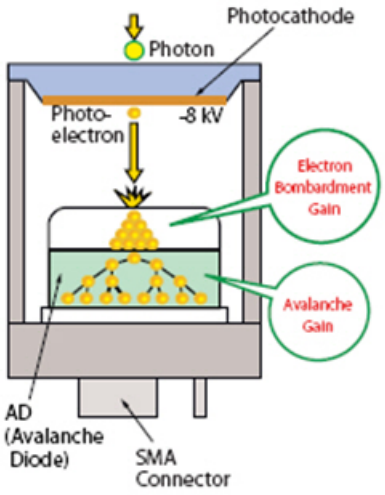

Figure 1.5: *A schematic view of the HPD operating principle. An APD substitutes the dynode chain of a classical PMT.*

1.2.1, the APD internal gain is low (≤ 100), consequently in such a device the total gain is obtained in two steps: electron-bombardment gain followed by avalanche gain.
In electron-bombardment, gain is proportional to the photoelectrons energy,

hence photoelectrons are accelerated towards the APD by a very large voltage difference ($\sim 8kV$ resulting in a gain of about 1600). Each photoelectron deposits its kinetic energy in the APD and produces many electron-hole pairs in the silicon substrate.
The electrons then drift towards the pn-junction, and avalanche gain occurs. In avalanche gain, the electrons collide with the crystal lattice of the silicon and create new electron-hole pairs which create more electron-hole pairs in a series of chain reactions. Depending on the reverse bias voltage applied to the APD, the avalanche gain can range from 10 to 100. The total gain of the HPD can reach the value of about 10^5.
The employment of the APD in substitution of the dynode chain leads to a huge improvement of the signal quality. Indeed, avoiding a gain in series also the propagation of the fluctuations in the dynode chain can be avoided and the resolution of the single photoelectron becomes higher, see fig. 1.6.

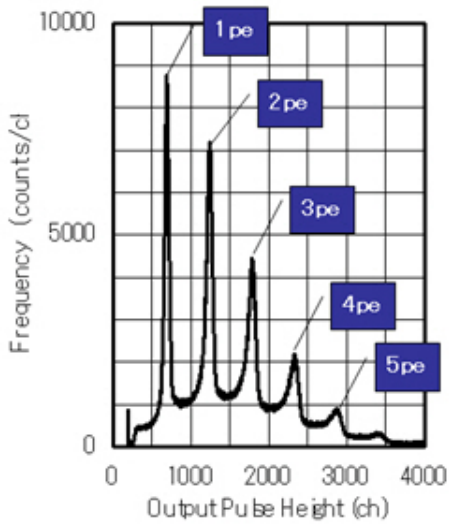

Figure 1.6: *A typical HPD spectrum. The signal quality is much higher with respect to that of the vacuum tubes thanks to the removal of the dynode chain.*

1.3.1 Limits on performances

Despite the APD is used in HPDs as electron detector and so as current amplifier, it maintains the same drawbacks it shows in its standard application.

- **Gain is limited by the noise**. As already said in section 1.2.2, there are some fluctuations in the avalanche process of APDs, causing the

generation of noise. This is also linked to the gain, the higher is the gain the higher is the noise. So, to avoid an excessive noise the gain has to be limited.

- **The high voltage.** Despite of the improvement of the signal quality with respect to PMTs, HPDs have a great weak point: the high voltage. Because of the low gain of the APD an additional gain is required. It is obtained with an electron bombardement of the APD. To accelerate the electrons towards the APD a very high voltage has to be supplied to the photocathode. It is of course very hard to stabilize the gain when it depends on a so high voltage.

Until now three classes of photodetectors have been analysed from the point of view of the amplification stage and its entailments, since it is the core of this thesis.
Anyway all those detectors have others important characteristics that have to be taken into account. A quick overview of the main characteristics of the photodetectors mentioned above is resumed in the following table.

	PMT	**APD**	**SiPM**	**HPD**
Gain	$10^6 \div 10^7$	≤ 100	10^6	$10^4 \div 10^5$
Operational Bias	High	Medium	Low	High
Temperature Sensitivity	Low	High	High	High
Mechanical Robustness	Low	Medium	High	Low
Ambient Light Exposure	NO	OK	OK	NO
Form Factor	Bulky	Compact	Compact	Bulky
Large Area Available	Yes	NO	NO	Yes
Magnetic Field Sensitive	Yes	Yes	NO	Yes
Noise	Low	Medium	High	Medium
Rise Time	Fast	Slow	Fast	Medium

Table 1.1: *Table of the main characteristics of a photodetector. In the table four typologies of photodetectors have been compared: PMTs, APDs, SiPMs and HPDs.*

Chapter 2

The VSiPMT: an original design for an innovative light detector

In the previous chapter a comparison between three classes of photodetectors have been done. From this analysis emerges that different multiplication processes can entail substancial differences in the detection features.
Indeed, even if PMTs boast almost one century of history, they show many defects.
The solid state photodetectors, APDs and SiPMs, represent a technological progress that goes beyond PMTs' limits. In particular, SiPM technology has achieved a very high level of performances that can meet the requirements of many experiments.
Despite all, both APDs and SiPMs have a size limited by the thermal noise, so their application to astroparticle physics experiment is partially compromised.
A big challenge is, therefore, to find a way to use SiPMs to detect photons from large surfaces and/or volumes, as typically needed in many astroparticle physics experiments.
Nowadays surface and volume reduction can be achieved in three ways:

1. collecting photons and conveying them towards a SiPM device;
2. enlarging the sensitive detector area by ordering several SiPMs in a pixelated matrix shape;
3. making a photon conversion by a photocathode which focuses photoelectrons on the small SiPM area.

In the first case one of the methods that can be used to obtain the geometrical area reduction is using wavelength shifter fibres embedded in a plastic scintillator body and connected at the other end to the SiPM [15]. This design allows to implement both tile scintillation calorimetry in strong magnetic fields and read-out for TOF[1] or trigger scintillators for the next high energy physic experiments.
In the second case the image compression from large surface detectors can be realized using matrices where each pixel is a SiPM [16]. This device would be of immediate utility in the experiments detecting the Cherenkov radiation or the fluorescence light produced in the atmosphere by interacting cosmic rays. However, making a matrix of SiPMs imply an enormous increasing in dark count rate.
An interesting option is represented by the third case, the VSiPMT (Vacuum Silicon PhotoMultiplier Tube), an innovative design for a modern hybrid photodetector based on the combination of a SiPM with an hemispherical PMT standard envelope, see fig. 2.1 [17].

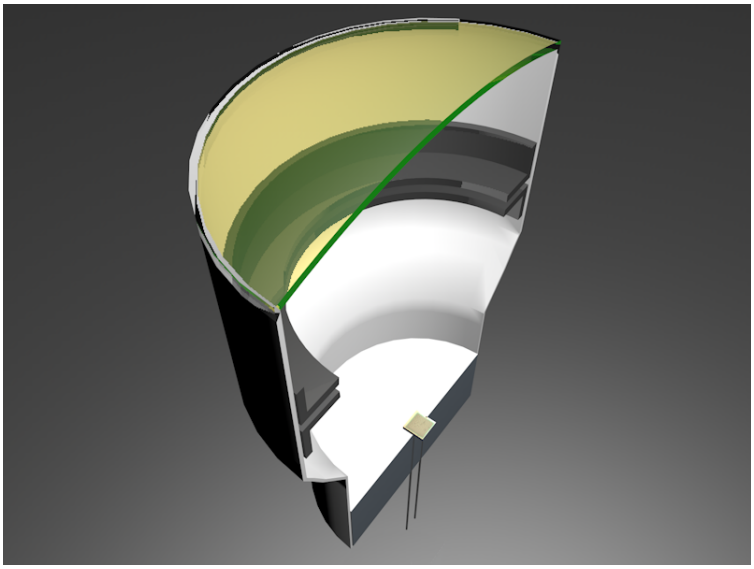

Figure 2.1: *A cutaway of the VSiPMT showing the interior composition of the device. On the top there is the light entrance window, then a photocathode for the photons conversion into electrons. In the middle there is a focusing ring producing an electric field which accelerates and focuses the photoelectrons on the SiPM surface. Finally, on the bottom there is the SiPM acting in this configuration as an electron detector and current amplifier. Everything is assembled into and hermetically sealed container.*

[1]TOF is the acronym for Time Of Flight.

The idea was born in Naples in 2007 exactly with the goal to enlarge indirectly the SiPM sensitive surface, thus exploiting its good detection features also in large astroparticle physics experiments [18].
In this device the multiplication stage is provided by the SiPM that acts as electron detector and so as current amplifier.
Taking into account the benefits in the detection features obtained with the introduction of HPDs, it seems that the hybridization can be the right road to follow to use solid-state photodetectors for large volume experiments.

2.1 Photocathodes

The VSiPMT design includes a photocathode to convert photons into electrons that will be than detected and thus multiplied by the SiPM.
Photocathodes are mostly made of compound semiconductors, consisting of alkali metals with a low work function, and can be operated both in reflection (opaque) and in transmission mode (semitransparent) [19].
In the former case, when the light enters and impinges on the photocathode a photoelectron is extracted in the same side of the incoming light and is driven on the multiplying sensor, fig. 2.2a, while in the latter case when the light impinges on the photocathode a photoelectron is extracted on the opposite side with respect to the incoming light, see fig. 2.2b. In both configurations,

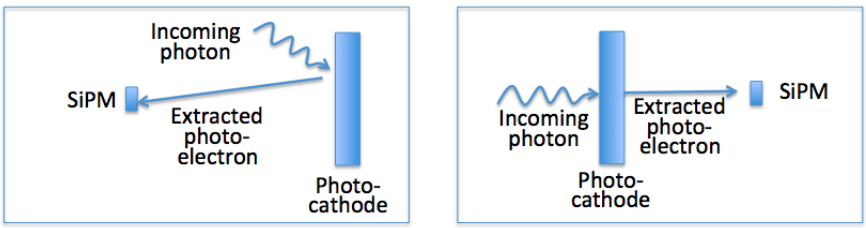

Figure 2.2: *Reflective and transmission mode photocathodes operating principle.*

different materials can be used. The materials can be chosen depending on the spectral region of sensitivity and on the achievable quantum efficiency. The spectral response of several materials is showed in fig. 2.3. Photocathodes operation can be described using the energy band theory expressed in terms of the energy gap (E_g), electron affinity (E_a), Fermi level (E_f), work function (ϕ), and so on. When a photon strikes a photocathode, electrons

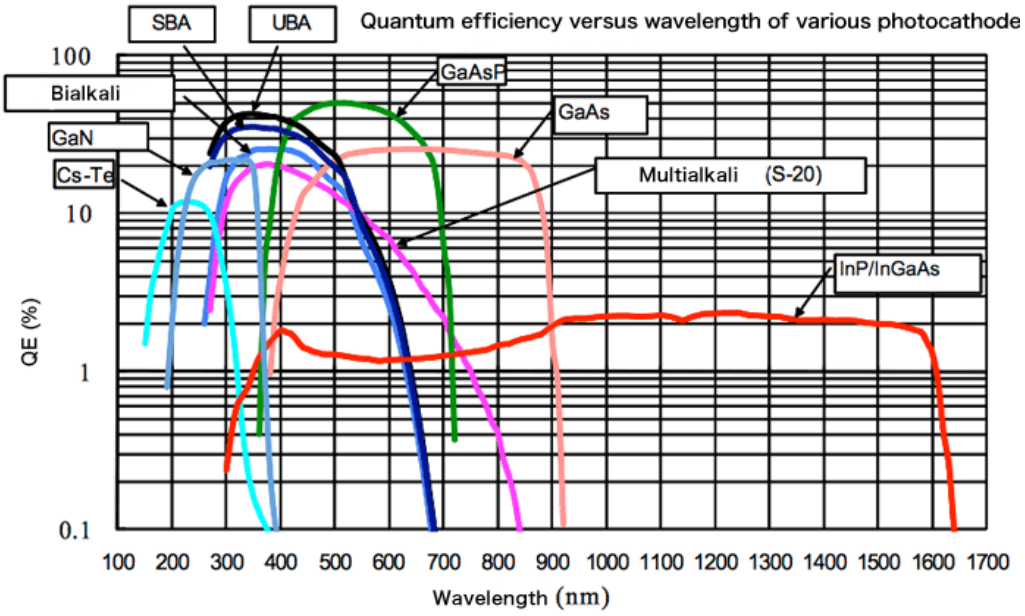

Figure 2.3: *Spectral response of photoelectron emissive materials.*

in the valence band absorb photon energy (E_γ) and become excited to the conduction band, diffusing toward the photocathode surface.
If the energy of these electrons overcomes the vacuum barrier, then they are emitted into the vacuum. This electron emission process was expressed as follows by W. E. Spicer [20].

$$\eta(\nu) = (1 - R) \cdot \frac{\alpha_{PE}}{\alpha} \cdot \frac{1}{1 + 1/\alpha L} \cdot P_s \tag{2.1}$$

$\eta(\nu)$	:	conversion efficiency of the photocathode material, i.e. *quantum efficiency*, function of the photon frequency;
R	:	reflection coefficient;
α	:	full optical absorption coefficient of photons;
α_{PE}	:	absorption coefficient when electrons are excited to a level greater than the vacuum level;
L	:	diffusion lenght of electrons;
P_s	:	escape probability of electrons;

This is called Spicer's three step model which explains the photoelectron emission process using three steps: optical absorption process, electron diffusion process, and escape process [21]. It is clear, from this expression that

it is possible to enhance the quantum efficiency by extending the diffusion length L to improve the crystalline properties of the photocathodes and also reduce the electron affinity by increasing the P_s (NEA-photocathodes).
It has been studied that a crystalline photocathode when activated by depositing a few monolayers of cesium and a strong oxidizer (such as fluorine or oxygen) gain the NEA (Negative Electron Affinity) property. This means that the Cs-O activation causes the energy band in the surface to curve downward so that the electron affinity has a negative value, thus allowing electrons at the bottom of the conduction band to escape, see fig. 2.4. The

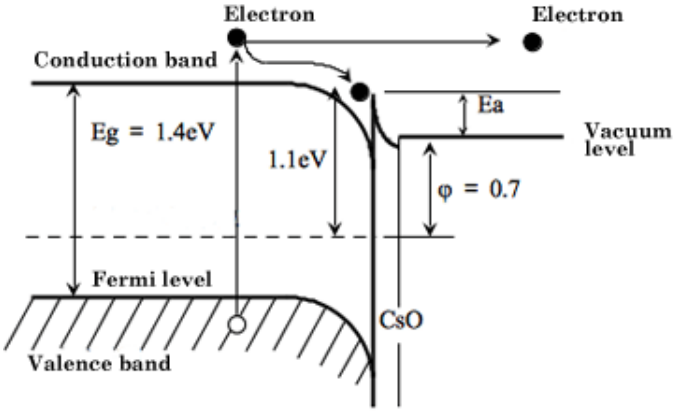

Figure 2.4: *NEA photocathode band model.*

most used photocathode materials are:

CsI Cesium iodide is not sensitive to solar radiation and therefore often called "solar blind". Its sensitivity sharply falls off at wavelengths longer than 200 nanometers and it is exclusively used for vacuum ultraviolet detection.

Bialkali (**Sb-Rb-Cs, Sb-K-Cs**) Since two kinds of alkali metals are employed, these photocathodes are called "bialkali". The transmission type of these photocathodes has a spectral response ranging between ultraviolet and visible region. On the other hand, the reflection-type bialkali photocathodes are fabricated by using the same materials, but different processing. As a result, they offer enhanced sensitivity on the long wavelength side, achieving a spectral response from the ultraviolet region to around 700 nanometers.

Multialkali (**Sb-Na-K-Cs**) This photocathode uses three or more kinds of alkali metals. Due to high sensitivity over a wide spectral response range from the ultraviolet through near infrared region around 850 nm.

Ag-O-Cs Transmission type photocathodes using this material are sensitive from the visible through near infrared region, from 400 to 1200 nm, while the reflection type exhibits a slightly narrower spectral response region from 300 to 1100 nm. Ag-O-Cs photocathodes are chiefly used for near infrared detection.

2.2 Entrance window

Each entrance window material transmit the incoming light in a different way depending on the wavelength.
In particular, these materials tend to absorb ultraviolet light and, as a consequence, the choise of the window material determins the short wavelenght sensitivity limit of the whole device [22].
The most used window materials are:

MgF_2 A magnesium fluoride crystal is used as a practical window material because it allows transmission of vacuum ultraviolet radiation down to 115 nm.

Synthetic silica It transmits ultraviolet radiation down to 160 nm.

Borosilicate glass This is the most commonly used window material. The borosilicate glass does not transmit ultraviolet radiation shorter than 300 nanometers. It is not suited for ultraviolet detection shorter than this wavelength.

A plot of the window material transmittance with respect to wavelenghts is in fig. 2.5 A final overview about how the entrance windows usually matches the photocathodes is given by the table 2.1.

2.3 The SiPM as an electron detector

As said above, the VSiPMT is a new configuration for an hybrid photodetector in which the dynode chain is replaced by a SiPM, which acts as electron detector and multiplier.
For this purpose a special SiPM has to be realized. Since photoelectrons produced by the photocathode need a certain energy to enter into the Silicon bulk starting the Geiger avalanche and so to give a signal, high voltage

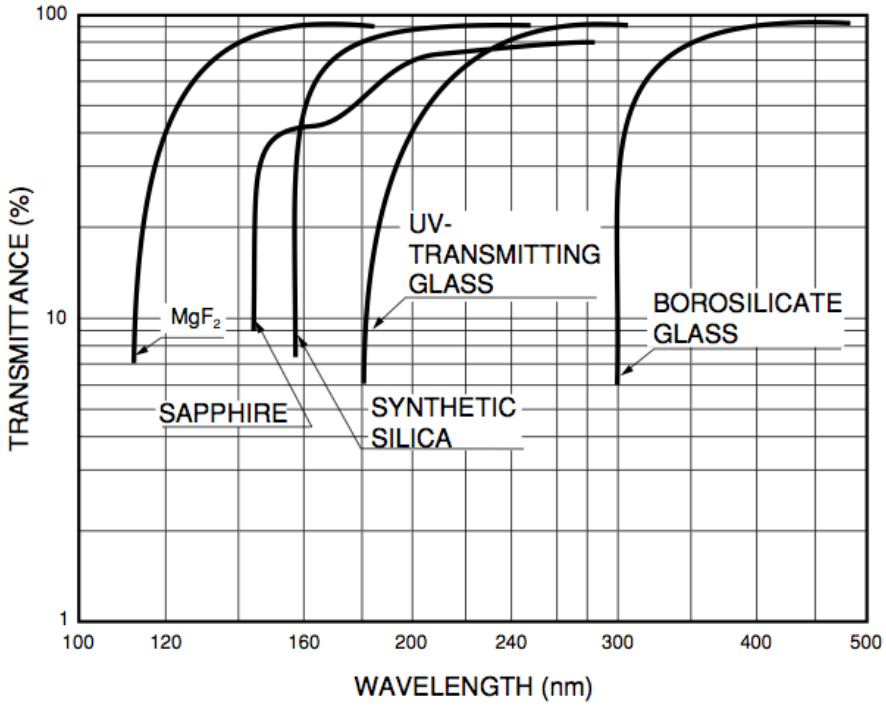

Figure 2.5: *A plot of the transmittance of several window materials with respect to wavelenght.*

Photocathode	**Window**	**Spectral Range (nm)**	**QE (%)**	**λ (nm)**
CsI	MgF_2	115-200	13	130
CsTe	Quartz	160-320	14	210
CsTe	MgF_2	115-320	14	200
Bialkali	Borosilicate	300-650	27	390
Bialkali	UV	185-650	27	390
Bialkali	Quartz	160-650	27	390
Multialkali	Borosilicate	300-850	20	375
Miltialkali	UV	185-850	25	280
Multialkali	Quartz	160-850	25	280
Ag-O-Cs	Borosilicate	400-1200	0.36	740

Table 2.1: Reference for spectral response of transmission mode photocathodes.

between photocathode and SiPM is required. A special windowless SiPM is necessary to minimize the threshold energy required.
When an electron enters into the Silicon bulk it generates electron-hole pairs

by ionization. In this case the Electron Detection Efficiency, namely EDE, can be evaluated as follows:

$$EDE = FF \cdot (1 - \eta)(P_e + P_h - Pe \cdot P_h) \tag{2.2}$$

From the equation 2.2, is clear that the probability that an impinging electron is detected depends on three factors: FF, the fill factor of the SiPM; η the backscattering coefficient; P_e and P_h are respectively the probability that the geiger avalanche is generated by an electron or a hole.
Since the SiPM is a matrix of cells the separation between the cells is a dead area, the percentage of active area of the device is,thus, given by the fill factor, FF, that represents therefore the geometric factor. When an electron impinges the SiPM surface, the entrance probability scales with the geometric factor FF.
An electron hitting the SiPM surface has a probability η to be backscattered. Hence, the probability that an electron enters in the Silicon bulk is $(1 - \eta)$, where η has been estimated to be ~ 0.17 with a Geant-4 based simulation.
Finally, once the electron is enter it produces an ionization track that generates electron-hole pairs. In such a device both electrons and holes can start the geiger avalanche. The probability that the geiger avalanche is triggered by an electron, P_e, is double with respect to the probability that the geiger avalanche is triggered by an hole, P_h. As a consequence in order to maximize the EDE, the SiPM needs a p over n structure. A more clear outline of the

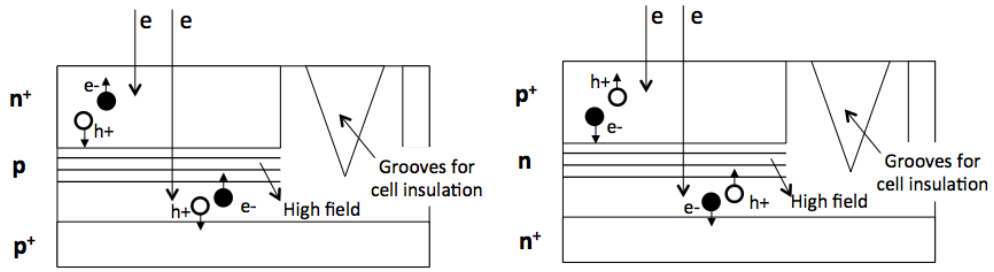

Figure 2.6: *LEFT: n-over-p internal structure of the SiPM. RIGHT: p-over-n internal structure of the SiPM.*

situation can be done by looking at fig. 2.6. On the left a scheme of the processes occuring in a n-over-p configuration are presented, while on the right picture there are those occurring in a p-over-n configuration of the SiPM.
The main difference between the two internal structures of the SiPM is that in the former case the incoming electron needs to cross the high field region

in order to let the electron start the geiger avalanche, while in the latter case is not necessary.
Actually, in a p-over-n SiPM the photoelectron ionization range lies in the p^+ region allowing electrons to cross the whole high-field zone p^+n, going to 0 voltage, and triggering the Geiger avalanche with high efficiency. This configuration is particularly suited for the VSiPMT application because allows to detect also electrons with a shorter range and so with a lower energy. This simplifies far and away the operation of the VSiPMT making possible to achieve a low operating voltage of the photocathode and focus ring ($\sim 3kV$). In addition, since few electron-holes pairs are sufficient to induce the micropixel Geiger discharge, the precise and very short range of the photoelectrons inside the SiPM allows a reduction of the thickness of the entrance layer of the junction p^+nn^+. This turns to be a great advantage, not only increasing the EDE, but also lowering the dark current (due to the reduction of the silicon volume).
Using a Silicon photomultiplier allows to reach a very high gain totally provided by the pixels working in geiger mode. This has many advantages:

- **Excellent photon counting**. The photocathode is only a passive intermediary. The photons are converted into electrons that are accelerated towards the SiPM surface. The electron entering into the Silicon bulk gives a standard output signal. So as for photons, the device shows an exellent resolution of the single electron allowing an easy photon counting.

- **High gain with low voltage**. Differently from a classical HPD, in this case the high gain is totally realized by the SiPM pixels operating in geiger mode. The electron crossing the geiger region gives an output standard signal with the typical gain of the SiPM $\sim 10^6$. This means that there is no need for an additional gain step provided by high energy photoelectrons. In such a device, indeed, the photoelectrons only need to enter into the Silicon bulk to produce a signal. Therefore it exists a threshold energy for the photoelectrons that is necessary to drive them in the geiger region of the device and is given by the voltage difference between the photocathode and the SiPM. The average voltage supplied to the photocathode in a VSiPMT is commonly $\sim 3\,kV$.

- **Negligible power consumption**. The absence of the dynode chain entails that also the voltage divider used to supply voltage to the dynodes is unnecessary. Removing the voltage divider means that in VSiPMT the power consumption is linked only to the photocathode and the SiPM. So thanks to this new configuration a substancial reduction

in power consumption is achieved, thus resulting now $\lesssim mW$. This is a great deal for such experiments operating in hostile environments (i.e. underwater, in ice or in space).

- **No gain dependence on the noise**. Since the SiPM operates in geiger mode, the gain is not anymore limited by the thermal noise, which is totally independent.

- **High speed**. The absence of a dynode chain means that the transit time is lower because it involves only the path from the photocathode to the SiPM. Moreover being the voltage difference between photocathode and SiPM much higher with respect to the one in a PMT ($\sim kV$ vs $\sim 100V$) means that in VSiPMT the photoelectrons have a higher energy and so are faster than in PMTs. As for transit time, also the spread in transit time (TTS) is simply due to the electron trajectories between the photocathode and the SiPM and so a sistematicalreduction of the VSiPMT TTS with respect to a classical PMT TTS is expected.

- **Compactness and simplicity**. Using a SiPM allows to obtain a device very compact and mechanically simple, having a lower number of connection with respect to a PMT.

Chapter 3

The VSiPMT Project

The VSiPMT project started with the study of feasibility of the device.
The first step was understanding the theoretical behaviour of an electron impinging on the SiPM surface [23]. This study was mandatory because it has reported fundamental informations about the energy threshold of photoelectrons and so on the operating voltage of the whole device.
The second part of this preliminary work was the experimental study of the response of a SiPM to an electron beam [24].
The experiment has been set up according to the results of the simulation and has been conducted at the TTT-3 accelerator, available at the Physics Department of the University of Naples Federico II [25].
The results obtained opened up to many possibilities about the VSiPMT feasibility, pushing Hamamatsu Photonics[1] to realize two industrial prototypes of VSiPMT [26].

3.1 The VSiPMT industrial prototypes

Two prototypes *EB-MPPC050 (ZJ5025)* and *EB-MPPC100 (ZJ4991)* have been realized by Hamamatsu Photonics. They have the same external case. A picture of one of them is shown in 3.1. As evident from fig. 3.1, the absence of the divider entails visible consequences:

1. the device is compact;

2. there are only three connections: two cables to supply power to the photocathode and to the MPPC (the thin red cable on the right and

[1]Hamamatsu Photonics is a world leader company in the production of photodetectors, both PMTs and SiPMs technology.

the lemo cable on the left, respectively) and one SMA output for signal readout.

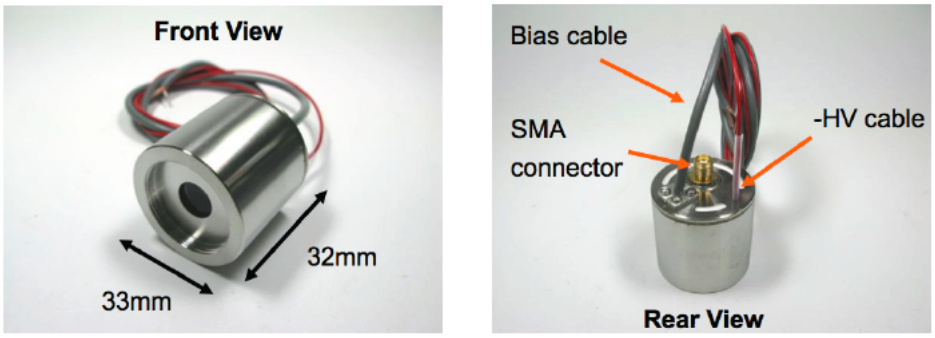

(a) (b)

Figure 3.1: *Front view (a) and rear view (b) of the prototype ZJ5025.*

The mechanical characteristics of the devices are shown in figure 3.2 a. On a Borosilicate Glass square window ($7 \times 7\, mm^2$) is deposited a circular GaAsP photocathode ($3\, mm$ diameter), where photon-electron conversion occurs. The GaAsP (Gallium Arsenite Phosphate) photocathode offers high

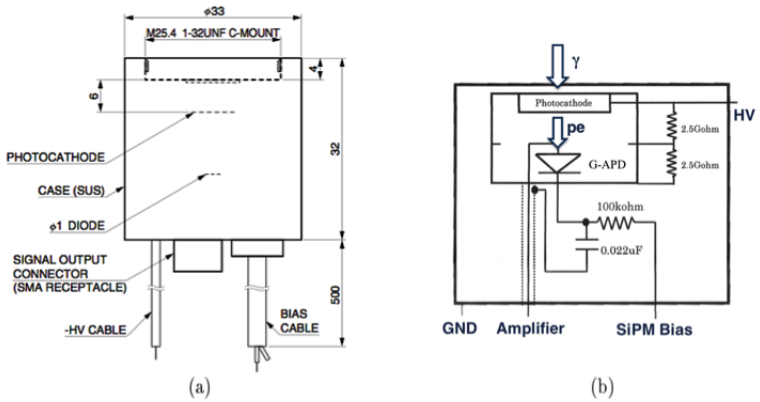

(a) (b)

Figure 3.2: *(a) The mechanical design of the prototypes. (b) The conceptual design of the prototype*

quantum efficiency optimized for the detection of visible light. The photo-

cathode spectral response is shown in fig. 3.3: the peak value of QE results to be about 50% for an incident wavelength $\lambda = 500\,nm$. A single stage

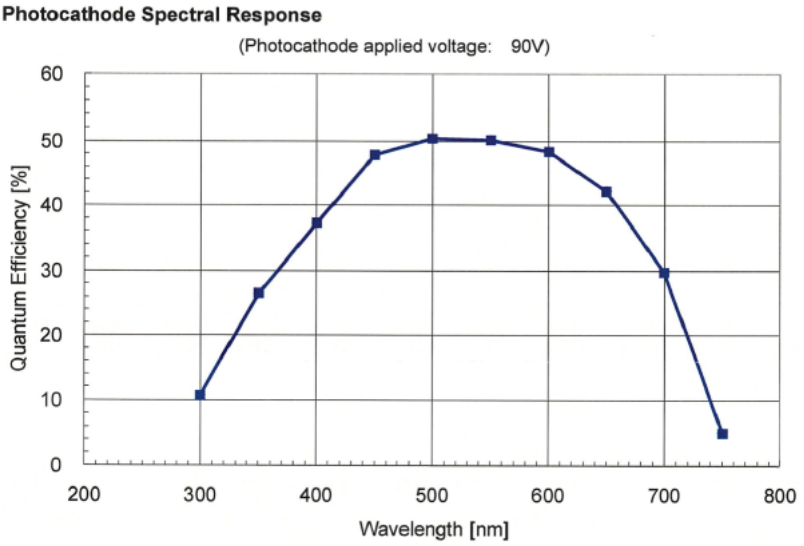

Figure 3.3: *The spectral response of the GaAsP photocathode.*

focusing system is present to drive the photoelectrons on the MPPC. It is composed by a focusing ring kept at half potential with respect to the HV applied to the photocathode, through a two-resistors voltage divider circuit ($2.5\,G\Omega$ each), see fig. 3.2 b.
The system is accomodated into a cylindrical Steel Use Stainless (SUS) case which dimensions are $\phi = 33\,mm$ and $L = 32\,mm$.
Only three connections are present on the bottom part, as said above: two power supply cables and one SMA connector for output signal readout.
On the top of the cylindrical case, a C-MOUNT thread has been realized in order to easily connect optical devices.
In each prototype a special windowless MPPC is mounted, the absence of the protective entrance window eases the entrance of the photoelectrons into the Silicon. Moreover, the MPPCs used is realized in a p^+nn^+ configuration for EDE optimization, as previously explained. Thanks to this a lower energy threshold is expected, with respect to what predicted in the simulation and then observed in the proof of feasibility.
The two devices differ only in the characteristics of the MPPCs used, see Table 3.1.

Table 3.1: *Table of the VSiPMT characteristics.*

Prototype	**ZJ5025**	**ZJ4991**
MPPC Area (mm^2)	1×1	1×1
Cell Size (μm)	50	100
Total Number of Cells	400	100
Fill Factor	61	78
Optimized Configuration	p^+nn^+	p^+nn^+
MPPC Operation Voltage (V)	72.5	72.4
Photocathode Power Supply (kV)	-3.2	-3.2

3.2 The amplifier

The typical VSiPMT single photoelectron (*spe*) signal amplitude is a fraction of mV, thus an external amplification stage is required.
Three custom amplifiers have been realized following the detection constraints: a moderate gain ($\sim 10 \div 20$) and a fast response (the rise time of the VSiPMT signal is $\sim ns$). An AD8009 OpAmp by Analog Device, a 5 GHz bandwidth Operational Amplifier used in non-inverting configuration has been selected for those purposes.
The final amplifier (see fig. 3.4) is set also to adapt the output signal of the prototype to the readout electronics so it has been realized with a $50\,\Omega$ input impedence and a $50\,\Omega$ output line. The three versions present different gains: 10, 15 and 20 V/V, respectively.

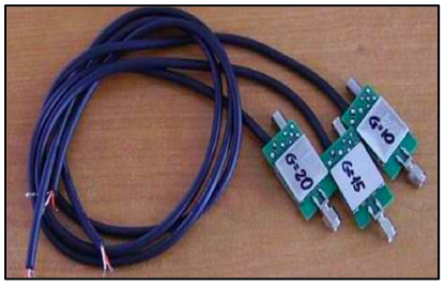

Figure 3.4: *The three versions of the custom amplifier realized to read the VSiPMT prototype signal.*

The shape of the output signal from the amplifier with gain 20 is shown in Fig. 3.5. The typical amplitude after the amplification turns out to be few tens of mV with rise time of few ns.
The amplifier, powered with $\pm 3.3V$, is the main source of power consumption. The overall system VSiPMT+amplifier has a $5 - 10\,mW$ power consumption.

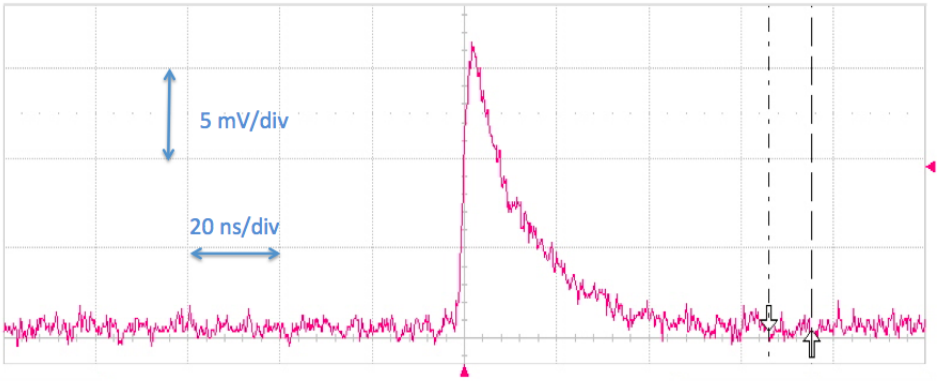

Figure 3.5: *Typical VSiPMT spe signal obtained with an amplifier with gain 20.*

This seems to be one of the main advantages that the VSiPMT exhibits with respect to a classical PMT, whose power saving is strongly limited by the voltage divider even in the latest series.

3.3 The VSiPMT characterization

The prototype underwent many tests summarized here below and discussed in the following sections [27], in order to achieve a full characterization of:

- signal quality, stability and photon counting capability;
- detection efficiency;
- gain;
- photocathode omogeneity;
- Transit Time Spread;
- afterpulses and dark counts;
- linearity and dynamic range.

Since both the prototypes exhibited similar performances, only the results of the ZJ5025 are presented in this thesis.

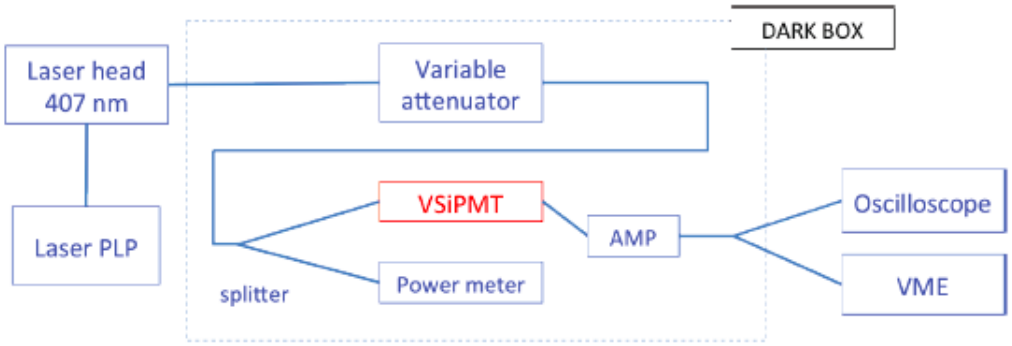

Figure 3.6: *Scheme of the experimental setup used fot the VSiPMT industrial prototypes characterization.*

3.3.1 Experimental setup

For the characterization of the two prototypes the experimental setup shown in fig. 3.6 has been realized. A picosecond light pulser (PLP C10196) by Hamamatsu has been used together with a laser head emitting in the blue region (407 nm).
The laser light is sent through a system of optical fibers inside the dark box, where the VSiPMTs tests take place. The laser light intensity can be varied by using a U-bench fiber port with a system of calibrated grey filters down to single photoelectron condition, see fig. 3.7 and is then sent simultaneously to the VSiPMT and to a power meter (Newport Model 2936-C, ∼10 pW resolution). The latter is an online monitor which ensures the laser stability for all the duration of the measurements. The VSiPMT is directly connected

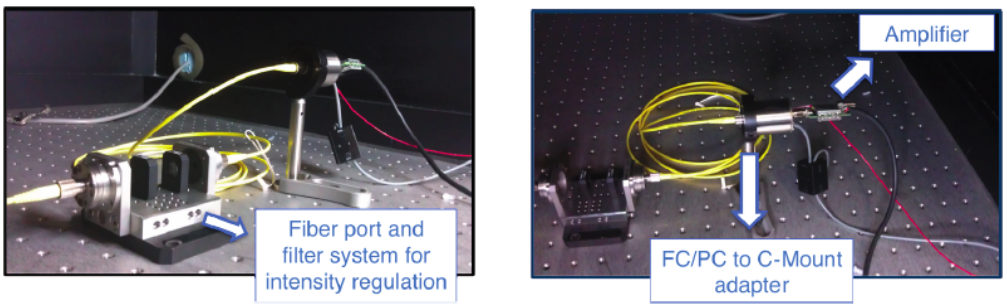

Figure 3.7: *LEFT: Light intensity regulation system. RIGHT: VSiPMT-fiber connection.*

to the optical fiber by a FC/PC to C-MOUNT adapter, guaranteeing for perfect alignment and good stability (see fig. 3.7, right picture). The output

signal of the VSiPMT is amplified by the circuit described in the previous section and is directly sent, through a lemo cable, to both an oscilloscope (LeCroy WaveRunner 104 Mxi, 1 GHz Analog Bandwidth, 8 bit resolution) and a VME chain, based on a flash ADC Waveform Digitizer (CAEN V1720E, 8 Channel 12bit 250 MS/s).

3.3.2 Signal properties and photon counting capability

First of all the VSiPMT signal properties have been studied.
A typical output waveform of the device is shown in fig. 3.5. As clear from the oscilloscope screenshot, the pulse duration is $\sim 40\,ns$ with a very short rise time (of the order of the nanosecond) and a fall time of $< 40\,ns$. The ZJ4991 prototype has the same rise time but a larger fall time ($\tau_R = C_D \cdot R_Q \sim 100\,ns$), due to the larger diode capacitance (C_D) arising from the larger active volume of each micro-cell.
One of reasons of utmost importance that led to the VSiPMT design is the expectation of a remarkable single photon resolution. With this purpose, a study of the photon counting capabilities of the device has been done by illuminating the photocathode with a very low intensity laser beam.
Figure 3.8 shows the output waveforms of the ZJ5025 device and the corresponding amplitude spectrum. For this measurement the synchronization

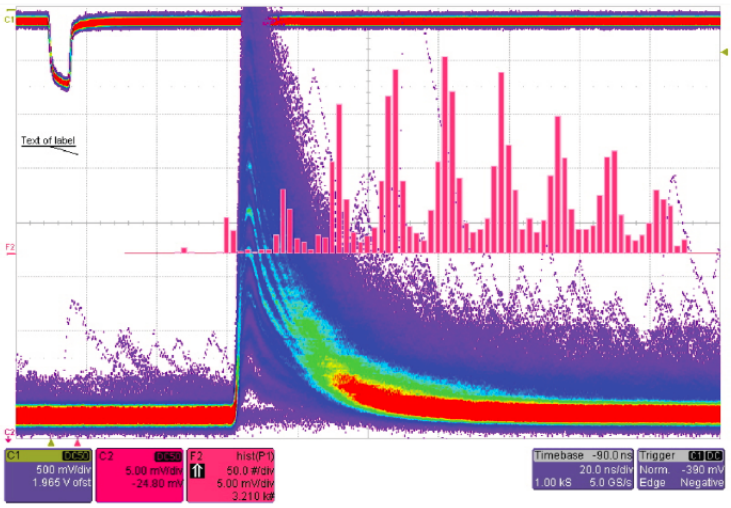

Figure 3.8: *Oscilloscope printscreen of the ZJ5025 prototype waveforms and its amplitude histogram.*

signal of the laser source has been used as trigger in the oscilloscope-based

acquisition system and the responses for multiple triggers have been overlayed in an infinite persistency.
Looking at the oscilloscope printscreen it is undeniable that waveforms corresponding to different numbers of fired pixels are very well separated, the same goes for the amplitude spectrum. This is a demonstration of the excellent photon counting capabilities of the VSiPMT prototypes. In fig. 3.8, as well as in the related amplitude spectrum it is possible to count separately the number of simultaneously fired pixels going from a single pixel up to nine, a performance simply unreachable by standard PMTs and even by the recently developed HPDs.
An additional test aimed at the measurement of the charge spectrum has been done by using the VME DAQ chain. In this case, lower light intensity conditions have been preferred. The charge spectrum plot in fig. 3.9

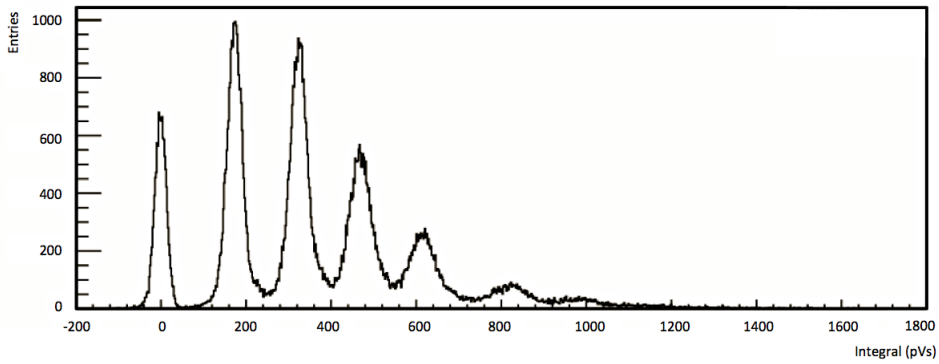

Figure 3.9: *Charge spectrum plot of the ZJ5025 VSiPMT prototype realized by Hamamatsu Photonics.*

has been obtained by acquiring 100.000 waveforms and, for each of them, calculating the integral in a time window of 100 ns, the value of the baseline introduced by the amplification circuit has been subtracted to them. The resulting charge spectrum confirmed the outstanding photon counting performances of the device.

3.3.3 Single photon detection characteristics

The single photoelectron (*SPE*) detection capability and resolution are two key factors that make the VSiPMT take the lead of large area photodetectors.
Therefore a test of the above mentioned detection characteristics of the VSiPMT industrial prototypes has been done. By illuminating the device

under SPE conditions a measurement of the peak-to-valley ratio and the SPE resolution have been obtained. The results shown in fig. 3.10 are excel-

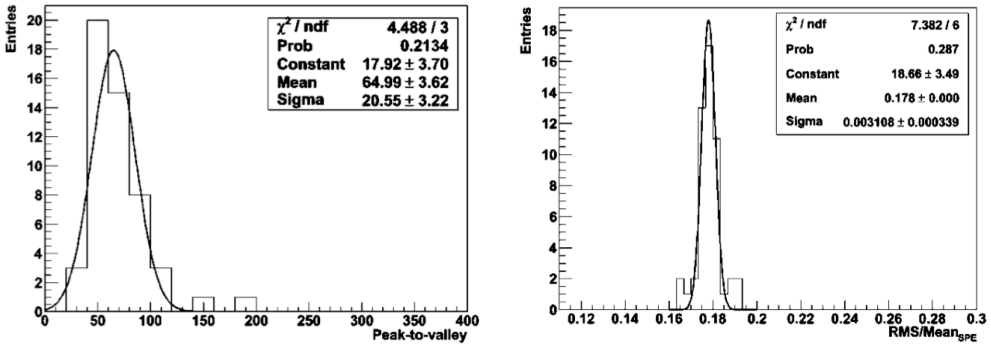

Figure 3.10: *LEFT: Peak to valley ratio plot. RIGHT: SPE resolution plot.*

lent: the peak-to-valley ratio results to be 65, with an improvement factor of several tens ($\simeq 30$) with respect to a standard PMT, while the measured SPE resolution (less than 18%) turns out to be improved of a factor $\simeq 2$. In PMTs the peak to valley ratio and, thus, the photon detection capabilities are strongly affected by the non-uniformities of the multiplication process, as already discussed in section 1.1.1. On the contrary, in the VSiPMT the fluctuations due to the dynode chain are no more present and therefore the high peak to valley ratio value is only a consequence of the excellent photon counting capabilities of the SiPM.
These results confirm, as expected, that a VSiPMT achieves far and away superior signal discrimination.
The stability of the signal has been proved by acquiring 100.000 waveforms, with low intensity laser light, every 20 min for 20 hours. The VSiPMT exhibits an extremely stable SPE response, with a mean deviation not exceeding the 2% over the whole data-taking period, see fig. 3.11. The time stability of the two prototypes has been tested also for high intensity illumination, in order to investigate possible fatigue effects of the device. Three different light levels have been set for this measurement, corresponding to 26, 52 and 65 detected photoelectrons, respectively. For each light level 100.000 waveforms have been acquired every 20 minutes for 100 minutes in total. Figure 3.12 shows the multi-photon response on the 100 minutes of data-taking time. It is evident that there is a flat trend on each measurement batch. This is an unequivocal proof that on this time scales the VSiPMT shows no fatigue effect on high illumination.

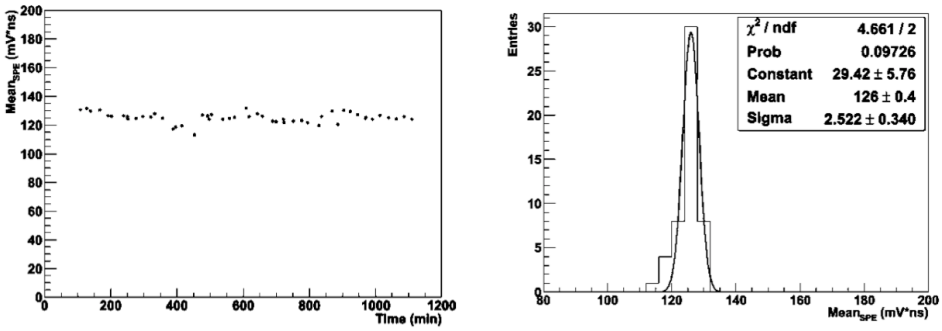

Figure 3.11: *LEFT: SPE stability in time plot. RIGHT: SPE distribution plot.*

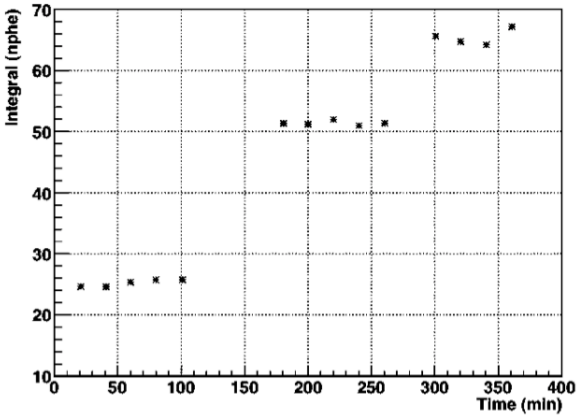

Figure 3.12: *Multiphoton stability in time plot.*

3.3.4 Detection efficiency: operating point and uniformity

The Photon Detection Efficiency (PDE) of the VSiPMT can be defined as the product of the photocathode quantum efficiency and the SiPM electron detection efficiency (see eq. 2.2) :

$$PDE_{VSiPMT} = QE_{PC} \cdot EDE_{SiPM} \tag{3.1}$$

The EDE can be considered, in a first approximation, to be coincident with the fill factor of the SiPM. Therefore, the PDE of the VSiPMT turns out to be:

$$PDE_{VSiPMT} = QE_{PC} \cdot FF_{SiPM} \tag{3.2}$$

The fill factors of the SiPMs used for the ZJ5025 and the ZJ4991 prototypes are 0.61 and 0.78, respectively, and the quantum efficiency of the photocath-

ode is 38% at $\lambda = 407\,nm$. Taking into account these values, the expected PDE for the two prototypes are $PDE_{ZJ5025} = 23\%$ and $PDE_{ZJ4991} = 30\%$. The PDE with respect to the high voltage supplied to the photocathode has been measured as follow.
The device has been illuminated with few photons per pulse (~ 70) by using an optical fibre, during the test the laser beam intensity has been monitored by the power meter. The PDE is experimentally defined as:

$$PDE = \frac{N_{pe}}{N_{ph}} \tag{3.3}$$

where N_{pe} is the number of fired cells and N_{ph} is the number of photons per laser pulse hitting the photocathode.
Once we set the light conditions, we tested the PDE as a function of HV, by varying the photocathode power supply in steps of 100 volts. The PDE behaviour has been measured, see Fig. 3.13. As evident from the figure, the

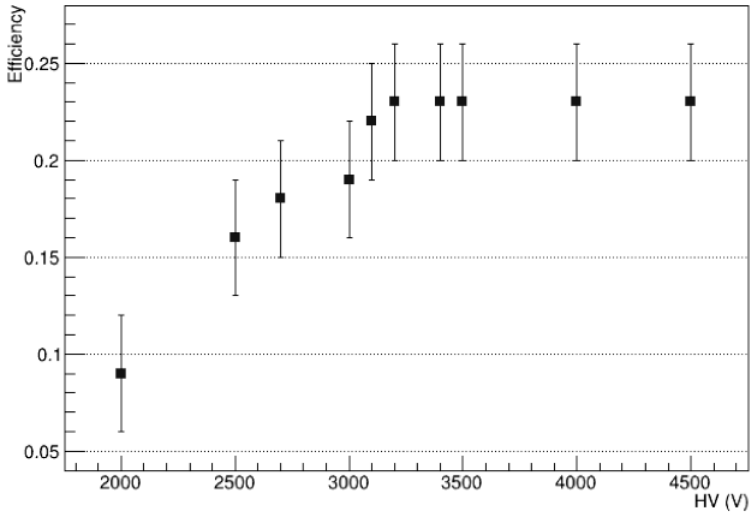

Figure 3.13: *Results of the photon detection efficiency test in function of the HV. The PDE errors are obtained by the propagation of the errors on N_{pe} and N_{ph}.*

PDE of the device becomes stable around $-3\,kV$, with a plateau till $-5\,kV$. The operating point for the high-voltage supply has been fixed to $-3.2\,kV$, corresponding to $\sim 23\%$ PDE value, as we expected.
Even lower operating points can be achieved by simply reducing the SiO_2 layer of the SiPM.
In such a device, the plateau region is linked to the energy threshold of the

photoelectrons, see section 2.3. The photoelectrons need a minimum energy to enter into the silicon bulk and, consequently, to produce a signal. Therefore, the high voltage is required only to drive photoelectrons to the SiPM surface and to give them the right energy. This is one of the biggest differences and advantages of the VSiPMT with respect to other photodetector categories (see section 1.1 and 1.3.1. This behaviour comes from the different gain concept applied in the VSiPMT where, as already exstensively illustrated, the high gain is provided by the geiger avalanche occurring in the SiPM and therefore the PDE doesn't depend on the photoelectrons energy once they are over the threshold. This means that once the device is operated in the plateu region further calibrations due to high voltage fluctuations are not necessary.
On the contrary, both for PMTs and HPDs the gain strongly depends on the photoelectron energy. For those devices the higher is the voltage supplied to the photocathode and the higher is the gain, implying the necessity of frequent calibrations.
An x-y scan of the photocathode has been done to probe the uniformity on the entire sensitive surface by estimating the local PDE. For this measurement a micrometric x-y motorized pantograph has been used, see fig. 3.14. Figure 3.14 (right side) shows the result of the x-y scan of the $3mm \varnothing$

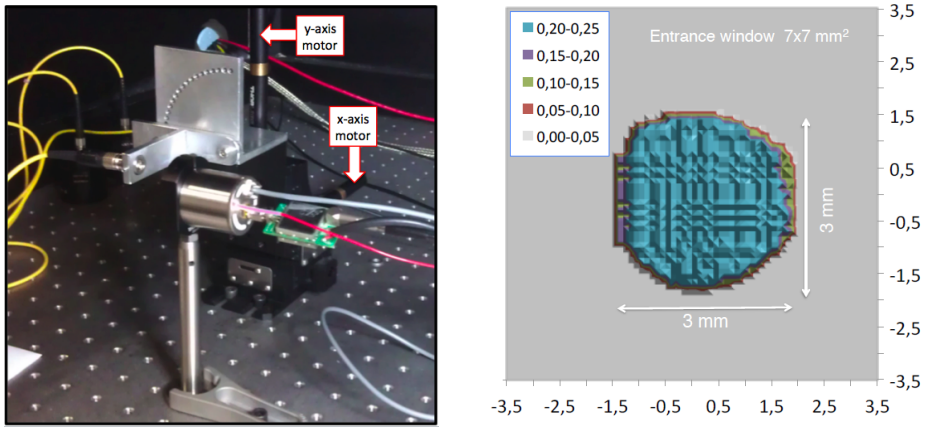

Figure 3.14: *LEFT: Experimental setup used for the x-y scan of the photocathode. RIGHT: Results of the x-y scan of the photocathode of the prototype.*

GaAsP photocathode in the $7 \times 7\ mm^2$ entrance window. The measured PDE ranges between 20% an 25% confirming a good uniformity through the whole photocathode surface. Boundary effects are negligible.

3.3.5 The gain

In a VSiPMT the gain is obtained by the electrons crossing the Geiger region of the SiPM. Thus, a standard current signal is given for each fired cell. Therefore, for the two prototypes under test the gain coincides with the gain of the SiPMs used.
According to the above description, the gain of the SiPM can be defined as the fraction between the charge of the pulse generated from each pixel during the breakdown process and the charge of the electron. The charge of a single fired pixel can be calculated as the difference between all the possible couples of adjacent peaks in the charge spectrum shown in figure 3.8. A measure of the SiPM gain as a function of the applied bias voltage in the range [72.1, 73.0] V has been performed, keeping HV = -3.2 kV. The result-

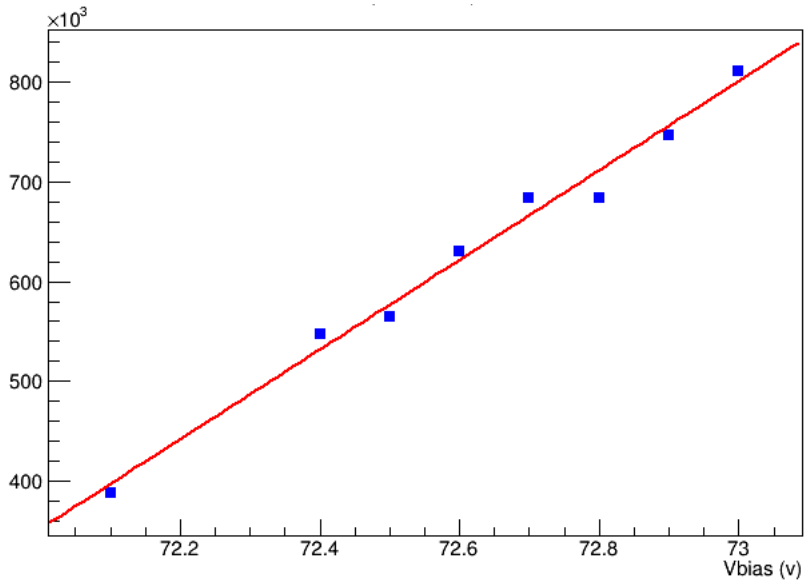

Figure 3.15: *Gain plot of the ZJ5025 VSiPMT prototype.*

ing curve (see fig. 3.15) exhibits a very linear trend, with values ranging between $[4 \cdot 10^5,\ 8 \cdot 10^5]$, in fairly good agreement with expectations. The uncertainty on the gain, estimated from the least observable error of 1 mV over a signal on the oscilloscope trace, is very simple to propagate to the calculated charge, and leaded to a 7% error, not shown in the graph.
A measurement of the gain value with respect to the voltage supply has been carried out at $-2.2kV$ (in the ramp up region) and at $-3.2kV$ (in the plateau region) and keeping the MPPC bias voltage at $72.5\,V$. As expected we found that the value for the gain at $72.5\,V$ is about $5.6 \cdot 10^5$, that is the expected

value for the MPPC. Then, we performed a further measurement by setting the HV to $-3.2\,kV$ and varying the MPPC bias voltage from $72.1\,V$ to $73.0\,V$ in steps of $0.1\,V$.
Taking into account the additional gain provided by the external amplifier (see section 3.2), the overall gain of the two prototypes under test ranges between 10^6 and 10^7. These values are comparable with the gain of a standard PMT, with the strong advantage of a much easier low voltage-based stabilization.

3.3.6 Transit Time Spread

The timing plays a crucial role in all those experiments and techniques where particle direction has to be reconstructed with high accuracy, like water Cherenkov neutrino telescopes for astroparticle physics and PET for medical equipments. From this point of view, a short TTS is mandatory to disentangle different events and to reconstruct the particle direction with a good angular resolution.
In all the vacuum photodetectors (PMTs, HPDs, VSiPMTs) the main contribution to TTS is given by the spread in electron path length. Neverthless, in VSiPMT the TTS is expected to be systematically lower with respect to that measured in standard PMTs, since the former lacks the contribution provided by the spread generated in the dynode chain. In a VSiPMT, indeed, the electron multiplication obtained by means of a breakdown is a very fast process with negligible time spread. The TTS measurement has been performed by using the experimental setup shown in Fig. 3.16. The synch

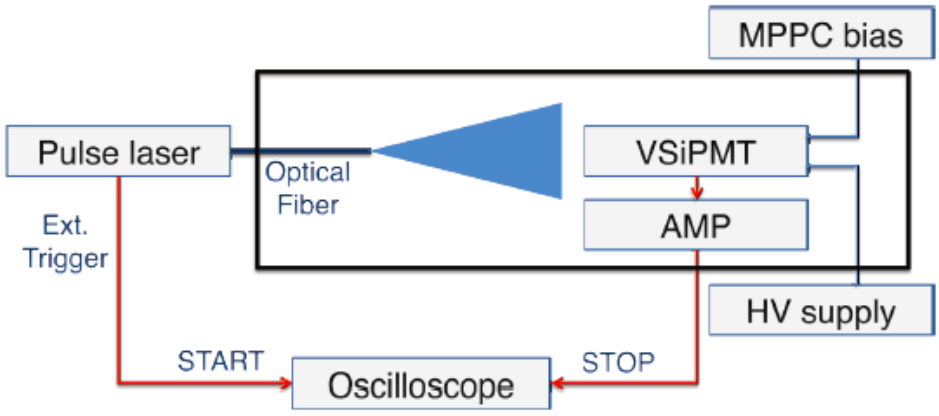

Figure 3.16: *Experimental setup scheme for the TTS measurement.*

pulse of the laser is used as trigger, while the output signal of the VSiPMT is fed as stop signal via a discriminator. The time difference between the start and the stop signal has been measured. Taking into account an eventual laser jitter, we estimated the TTS upper limit, as the σ of the distribution, to be $< 0.5\,ns$, see fig. 3.17.

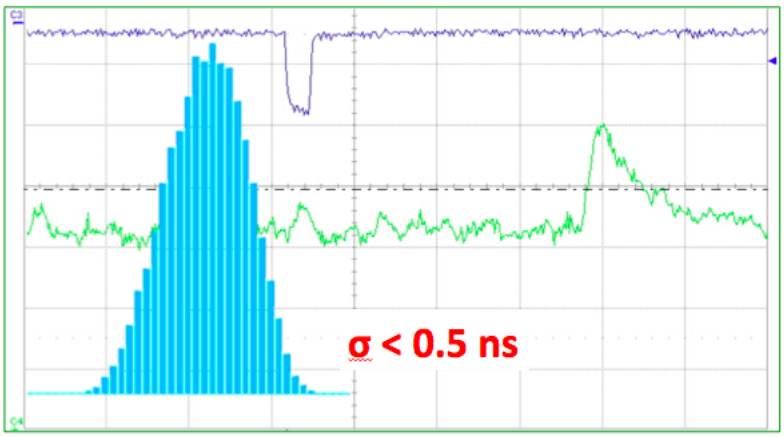

Figure 3.17: *Printscreen of the oscilloscope. The blue squarewave is the trigger signal from the oscilloscope. The green waveform is the VSiPMT spe signal. The x-axes unit is* $20\,ns/div$ *while the y-axes unit for the green line is* $5\,mV/div$*. The histogram is the distribution of the arrival time of the VSiPMT signal with respect to the laser trigger.*

3.3.7 The noise: dark rate and afterpulses

The main noise source in a VSiPMT is represented by dark pulses. Two contributions can be taken into account: thermal electrons emitted at the photocathode and intrinsic SiPM dark pulses. The latters represent the main contribution, since they have a typical rate ranging between few tens and some hundreds of kcps per mm^2 of active surface, depending on the applied bias voltage. In addition to the strong dependence on the bias voltage, SiPMs dark rate relies heavily on the pe threshold. For this reason, measurements of the dark count rate at different bias voltage and different thresholds have been done.
The photocathode voltage has been set to -4 kV and the bias voltage to three different values: 72.2V, 72.5 V and 72.8 V. For each of those values has been measured the number of events with peak amplitude above 0.5, 1.5 and 2.5 photoelectrons threshold. The results for both the prototype are shown

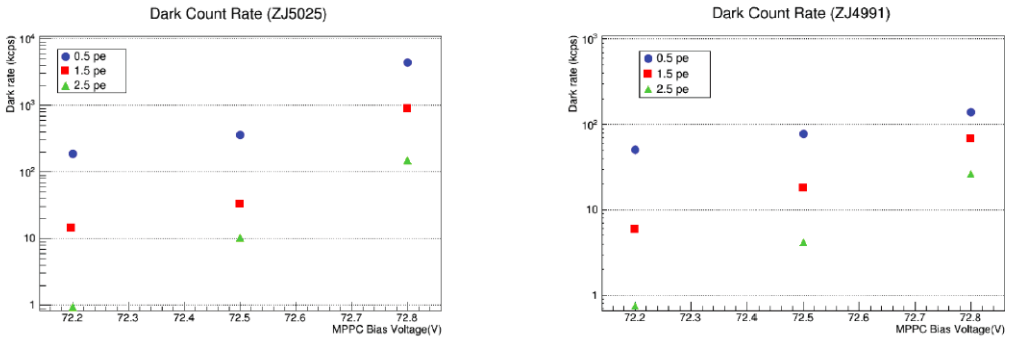

Figure 3.18: *LEFT: Dark counts rate plot for ZJ5025 VSiPMT prototype. RIGHT: dark counts rate plot for ZJ4991 VSiPMT prototype.*

in fig. 3.18. In both cases, the results are in excellent agreement with the expected dark count rate of the SiPM alone. In order to confirm the assumption that the main source of dark noise is the SiPM itself, the measure has been repeated in the same experimental conditions but with no high voltage applied to the photocathode. The results were essentially unvaried, see table 3.2.

A further noise source for the VSiPMT is represented by afterpulses. Also

Threshold (pe)	$Rate_{DC}$ (kcounts/s)	HV
0.5	348 ± 0.6	ON
0.5	361 ± 0.6	OFF
1.5	35 ± 0.2	ON
1.5	33 ± 0.2	OFF
2.5	10 ± 0.1	ON
2.5	11 ± 0.1	OFF

Table 3.2: VSiPMT dark counts at $V_{bias} = 72.5\,V$.

in this case, the combination of two technologies gives rise to a double contribution: vacuum related afterpulses and SiPM afterpulses.
The former are produced by the ionization of residual gases left in the tube after evacuation or degased materials present in the vacuum silicon photomultiplier tube after the evacuation. In this case the arrival time of the afterpulse depends on the ion mass and on the HV applied between the photocathode and the SiPM, while the afterpulse amplitude depends only on the HV [3]. The second class of afterpulses is intrinsically related to the SiPM technology. In this case, secondary pulses are generated by charges carriers that are temporarily trapped by some impurities inside the crystal lattice and

then released again after some delay which can last from few nanoseconds up to several microseconds. Typically, SiPM afterpulses are characterized by small amplitudes (corresponding to up to 3 photoelectrons) and high frequency.
A measurement to explore both afterpulse classes in VSiPMT and to get an estimate of the corresponding rates has been performed.
The prototype has been exposed to intense light conditions (corresponding to 32 photoelectrons detected), 100.000 waveforms have been acquired. The peaks above 3 Root Mean Square (RMS) of the noise level distribution have been collected and their arrival time, integral and pulse height have been reconstructed. The results are shown in fig. 3.19. The peaks found before

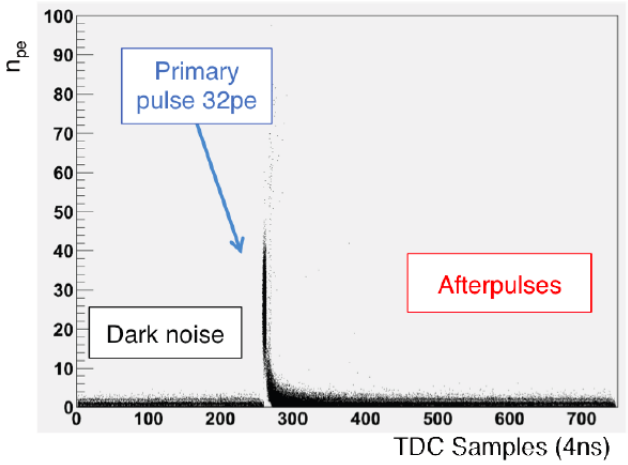

Figure 3.19: *Signal arrival time distribution plot for the ZJ5025 VSiPMT prototype.*

and relatively long after the primary pulse ($> 50\,ns$) occur almost uniformly. However, it is possible to observe a band of high intensity afterpulses (more than 10 photoelectrons) at a fixed 38.4 ns delay with respect to the primary pulse. These features are better displayed in fig. 3.20. As it can be observed in fig. 3.20 (left picture), the peaks detected before the primary pulse are uniformly distributed and characterized, in most cases, by single photoelectron amplitude. Only few two-photoelectrons and three- photoelectrons peaks have been found, suggesting a dark noise origin. On the other side, the uniformly distributed peaks detected long after the primary pulse correspond, on average, to a slightly higher number of photoelectrons.
This increase is given by the contribution of the SiPM-related afterpulses. Indeed, the measured afterpulse rates in this time interval (10.41%, 9.40% and 7.34%, corresponding to 0.5, 1.5 and 2.5 photoelectrons thresholds, respec-

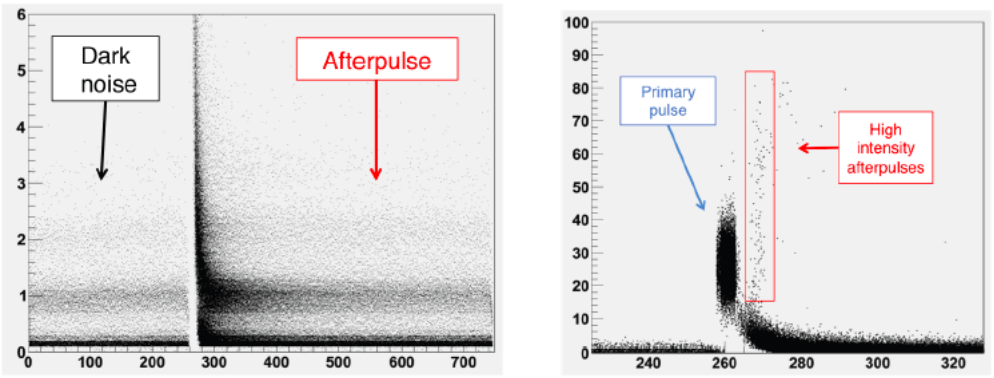

Figure 3.20: *LEFT: SiPM afterpulses for the ZJ5025 VSiPMT prototype. RIGHT: Residual gases afterpulses.*

tively) are in fair agreement with the typical afterpulse rates of a standard SiPM.
The high amplitude band shown in fig. 3.20 (right picture) is populated by peaks ranging from 10 to more than 80 photoelectrons and can be attributed to the contribution of vacuum-related afterpulses. In order to test this hypothesis, several runs have been taken keeping the same experimental conditions and varying only the HV applied to the photocathode. The results obtained are in table 3.3. It has been observed that, as the value of the

HV(kV)	Delay(ns)	Amplitude (N_{pe})
2	52.8	10-25
3	43.6	18-60
4	38.4	22-80

Table 3.3: *Measured values for afterpulses arrival time and amplitude.*

HV increases, the high amplitude band appears with a decreased time delay with respect to the primary pulse and an increased mean intensity, a result perfectly compatible with the expected behavior for afterpulses generated by the ionization of residual gases in the tube. However, the contribution of these afterpulses is really negligible, with a measured rate of < 0.02

3.3.8 Linearity and dynamic range

The dynamic range of a VSiPMT depends on the total number of cells of the SiPM and on the capability of focusing uniformly photoelectrons over the SiPM surface.

Given the total number of available cells (N_{cells}) of the SiPM, the number of fired cells (N_{pe}) as a function of the number of incident photons (N_{ph}) and of the PDE is given by:

$$N_{pe}(N_{cells}, \lambda, V) = N_{cells} \times \left[1 - \exp\left(\frac{-N_{ph} \times PDE(\lambda, V)}{N_{cells}}\right)\right]. \quad (3.4)$$

The exponential trend of the SiPM dynamic range sets a strict constraint on the performance of the VSiPMT. Indeed, the Eq. 3.4 represents the ideal maximum dynamics for the prototype under test, with $N_{cells} = 400$.
Another major contribution to the dynamic range of the VSiPMT is provided by the focusing. The GaAsP photocathode of the VSiPMT prototype has a circular shape. Therefore, taking into account the axial symmetry of the electric field generated by the focusing ring, an approximately circular photoelectron spot is reasonably expected. This means that an optimal focusing condition is achieved if the photoelectron beam spot is perfectly inscribed in the SiPM square target. In this case, no more than the 85% of the total number of cells of the SiPM can be fired, therefore the optimized dynamic range for the prototype is that plotted in Fig. 3.21 (green curve), corresponding to $N_{cells} = 340$.
Measurements of the dynamic range of the prototype have been performed. As a first step, the prototype has been kept in single photoelectron condition attenuating the incident laser light with an appropriate combination of the grey filters. Then, the number of the expected photoelectrons (PE_{exp}) has been gradually increased reducing the attenuation. At each step, the VSiPMT output has been measured (number of fired cells, N_{pe}). The experimental points are plotted in fig. 3.21. The measured values are distributed accordingly to the optimal dynamic range curve up to $\sim 20\,pe$. In correspondence to this value, a saturation effect starts to appear, with the following points increasingly deviating from the theoretical curve. This represents a robust hint for a too strong focusing. If such condition holds, the effective number of fired SiPM cells (N_{eff}) is smaller with respect to the optimal case, therefore the VSiPMT dynamic range curve is given by Eq. 3.4 with N_{eff} replacing N_{cells}.
N_{eff} has been estimated fitting the measured points to the theoretical curve of Eq. 3.4. The resulting curve, plotted in fig. 3.21 (blue), indicates a number of effective cells of ~ 80, corresponding to a photoelectron beam spot size of $\approx 0.4\,mm$. Such value is in fair agreement with the indications provided by the manufacturer. It is undeniable that the linear range of the ZJ5025 prototype results to be much smaller than expected. A similar results has been obtained by testing the ZJ4991 prototype.
The VSiPMT linearity is strongly related to the total number of pixels of the

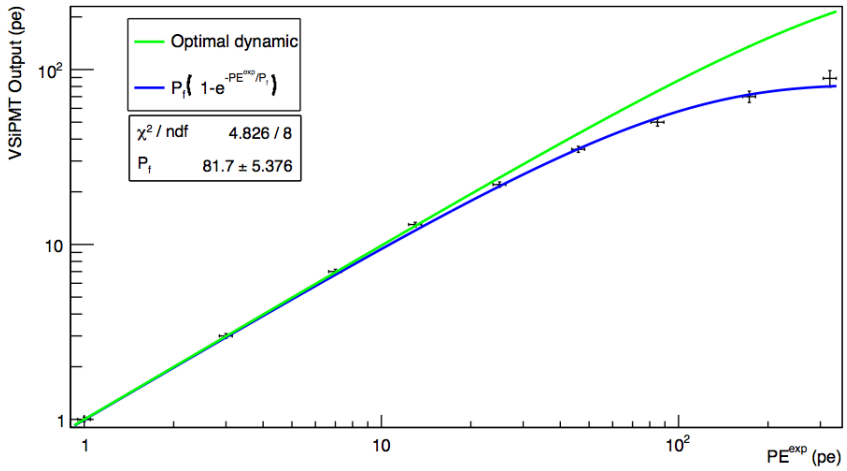

Figure 3.21: *Dynamic range of the prototype: experimental points, fit curve (blue) and optimal dynamic curve (green).*

SiPM used. Until the number of detected photons is much smaller than the number of cells, the output of the SiPM (and so of the VSiPMT) is fairly linear. As the number of detected photons increases, the output linearity starts to degrade until saturating when the number of photons is about equal to the number of cells.
Electrostatic focusing plays a crucial role in the definition of the dynamic range of a VSiPMT. Indeed, the output linearity of the SiPM is maximized if all its pixels are hit by the accelerated photoelectrons. In fig. 3.22 three

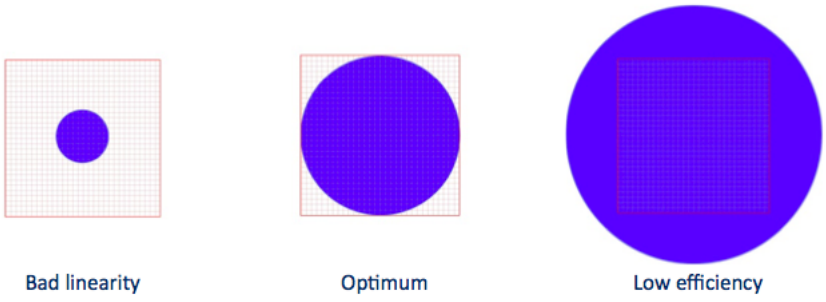

Figure 3.22: *Three exemples of the focusing effects.*

different focusing solution are proposed. On the left, a too strong focusing is the cause of a photoelectron spot smaller than the SiPM active surface. Differently from the cases of PMTs or HPDs, in VSiPMT the amplification

stage begins with a pixelated surface (the SiPM), as a consequence a too strong focusing would be deleterious. In this case, indeed, a too squeezed photoelectron spot means that a fraction of the SiPM pixels is not involved, this therefore drastically reduces the linearity of the device.
On the right, a too weak focusing causes a photoelectron spot larger than the SiPM surface. This means that a fraction of the photoelectron is sistematically missed, thus implying a reduction of the photon detection efficiency of the device.
In the center, the optimum solution for the focusing. The photoelectron spot is a circle inscribed in the SiPM surface, this is the configuration that exploits the maximum number of pixels leading to an optimized use of the device.
It should be clearly said that both the prototypes under test have been costless realized with the primary aim of testing the working principle of the device and hence its feasibility. No dedicated study has been performed about focusing, therefore the adopted solution is not optimized, thus explaining the reduced dynamic range with respect to the optimal case.
It is worth to notice that there is plenty of room to improve the dynamic range in a second generation of VSiPMT prototypes, with the adoption of a SiPM with a larger number of pixels (striking a balance with the fill factor) and with the realization of an optimized focusing for the maximization of the effective number of fired SiPM cells.
This was actually the starting point for the realization of a homemade larger and usable prototype.

Chapter 4

Realization of a larger prototype

The characterization of the first two prototypes of VSiPMT put up exceptionally encouraging results. The devices exhibit outstanding properties and performances beyond expectations, such as: excellent photon counting capability, fast response ($<$ ns), low power consumption ($\sim$ mW), great stability compactness and robustness.
The realization of the VSiPMT with a photocathode size ranging between 25 and 75mm$\varnothing$ will have a tremendous impact on astroparticle physics experiments and applied science by starting a new generation of photodetectors. All these attractive features lead to go ahead with a 2.0 phase aimed at the realization of a new optimized and usable version of the device with a larger photocathode area.
The starting point for the realization of such a device is the improvement of the focusing system.

4.1 The focusing system

As highlighted in section 3.3.8, although the industrial prototype has very good performances it has a lack in the dynamic range and linearity, due to a non optimized focusing.
In this phase a specific attention has been payed to that.
Since the SiPM is a pixelated device, electrostatic focusing is an awkward point for the whole VSiPMT performances in terms of dynamic range, linearity and so PDE. Indeed, the photoelectron beam size depends strongly on the electrostatic focusing field. If the focusing is too weak, the photoelectron spot exceeds the size of the SiPM, in this case a fraction of the photoelectrons

misses the target and is systematically lost, thus decreasing the overall PDE of the device.
On the other side, a too strong focusing produces a too much squeezed photoelectron beam, therefore the photoelectron spot intercepts only a fraction of the active surface of the SiPM, with a consequent reduction of the linearity.
In order to fully and correctly exploit the VSiPMT features the photoelectrons coming from the photocathode should:

- have a spot size comparable with that of the SiPM;
- be uniformely distributed on the SiPM surface.

The former requirement is to maximize the dynamic range exploiting all the SiPM surface. The latter, instead, is necessary in order to optimize also the linearity of the device, avoiding that more than one photoelectron fires the same cell.
These precautions are not necessary for PMTs and HPDs and represents the main problem for VSiPMTs and one of the determining goals of the engineering phase.
SimION 8.0-based simulations have been implemented in order to find a configuration that meets this requirements.
Obviously, the focusing fine-tuning becomes more difficult as the size of the photocathode increases. For this reason, together with a larger photocathode, a larger SiPM has been chosen.
A study of the focusing system for a 25 mm ⌀ photocathode over a $3 \times 3\,mm^2$ SiPM, is presented. Figure 4.1 shows the CAD model used for the simulations. The proposed solution is preliminary and consists of a single stage focusing system. Therefore, the device can be schematized as follows, see fig. 4.1:

- flat 25 mm ⌀ photocathode;
- focusing ring 25 mm in external diameter, 10 mm in height and 1.5 mm in thickness;
- $3 \times 3\,mm^2$ SiPM target.

The photocathode and the focusing ring are kept at the same voltage HV, while the SiPM is at its nominal operating voltage, i.e. 67.2V.
The electric field inside the model has been calculated selecting a stationary solver. Starting from the stationary solution of the electric field, it has been performed the simulation of electrons trajectories, see fig. 4.2. HV and SiPM position have been varied to observe changes in the electron spot shape. HV

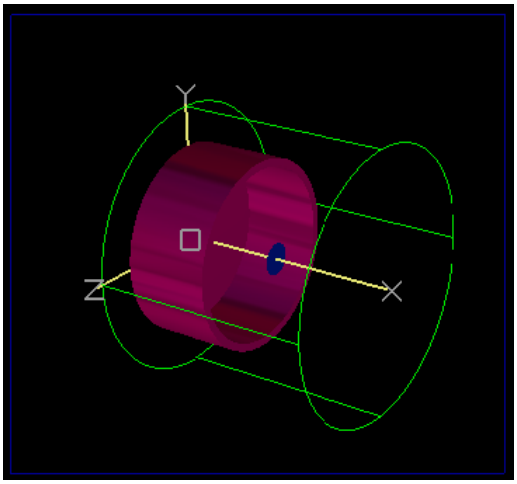

Figure 4.1: *CAD model of the VSiPMT used in the SimION-based simulations.*

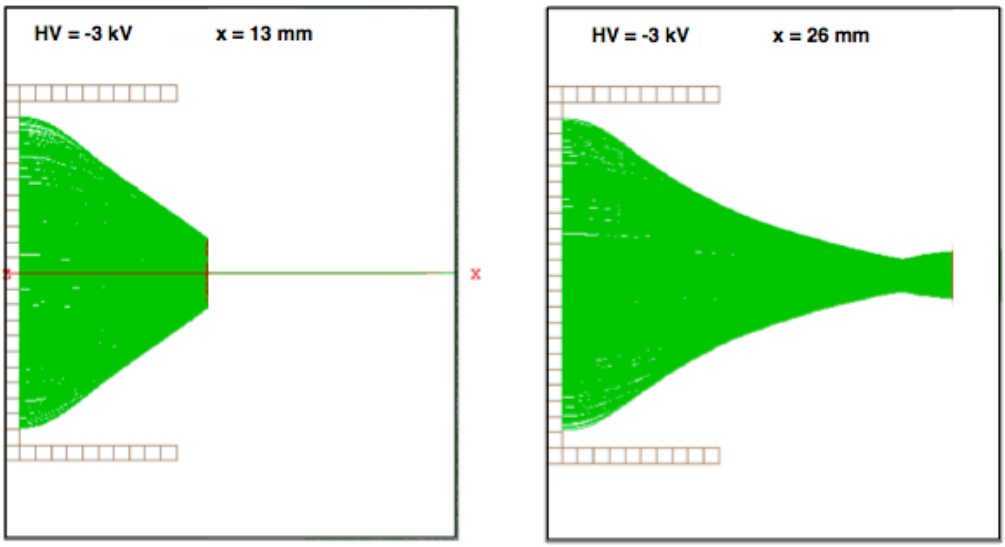

Figure 4.2: *Simulation of the electron trajectories, photocathode and focusing ring are kept at -3 kV and the SiPM position varies. LEFT: the SiPM is 13mm far from the photocathode surface. RIGHT: the SiPM is 26 mm far from the photocathode surface.*

has initially been set to -3 kV.
For each HV value, the distance between the SiPM and the photocathode has been modified and four parameters have been observed and evaluated: spot size and uniformity, transit time and transit time spread. To evaluate

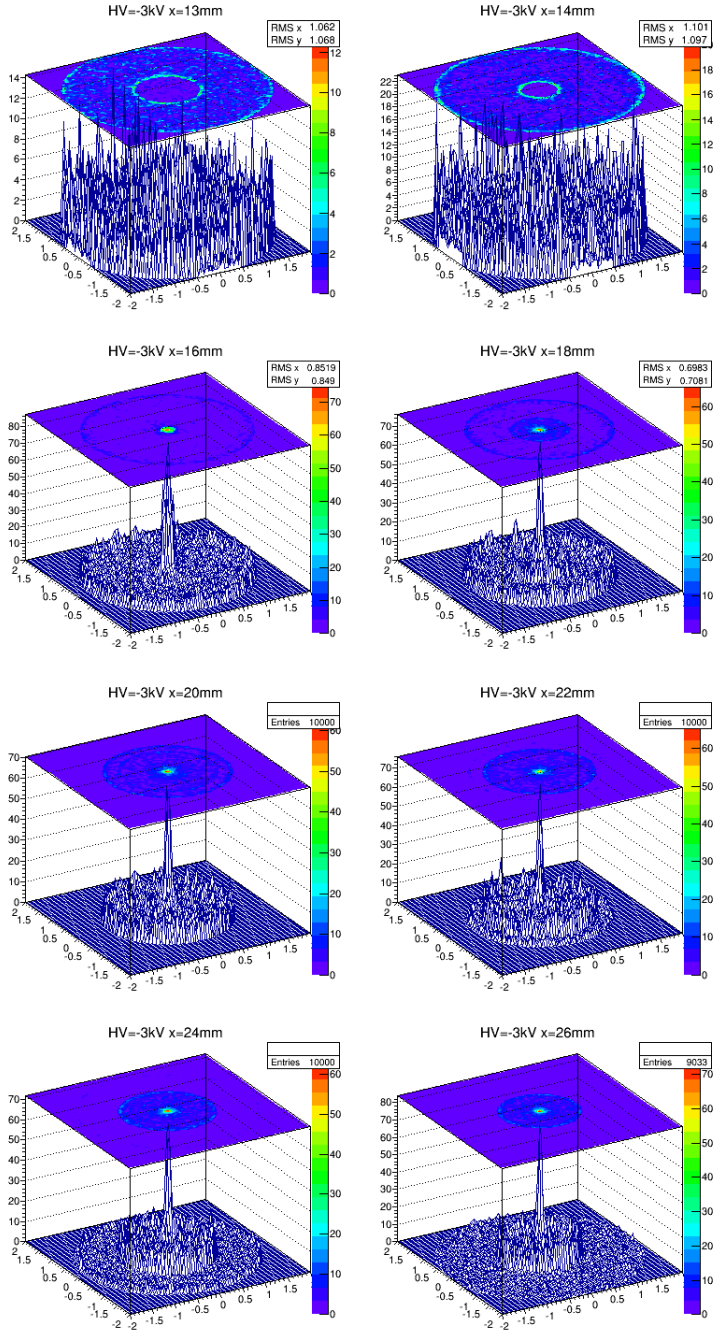

Figure 4.3: *Plots of the spot size and distribution on the SiPM surface. HV is set at -3kV and the SiPM position with respect to the photocathode varies in the range [13,26] mm.*

size and uniformity of the spot a square mesh, with pixels size of 50 μm, has been created on a surface dimension of $4 \times 4\, mm^2$ in correspondence of the SiPM longitudinal position. A circular uniform distribution with 10000 electrons is created on the photocathode and is then sent to the SiPM. The photoelectrons initial energy is set at 1 eV, with random initial speed directions.
The distribution of fired pixels of the mesh is shown in fig. 4.3. Additional 2D histograms have been plotted in order to ease the evaluation of the position that optimize operation of the device. Since the simulated electric field has a cylindical symmetry, in fig. 4.4 only the y-axis distribution of the photoelectrons on the SiPM surface is reported. From fig. 4.4 is evident that

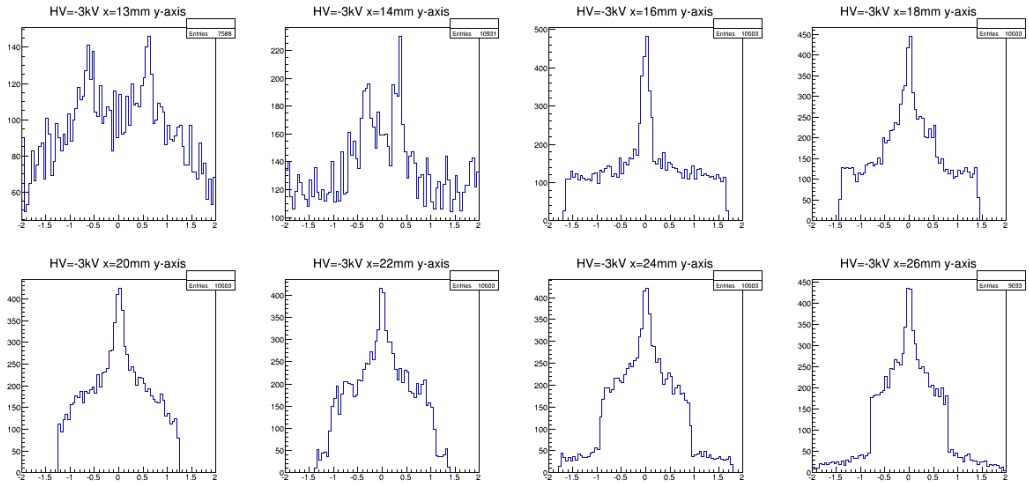

Figure 4.4: *y-axis distribution of photoelectrons on the SiPM when HV = -3kV and the SiPM distance with respect to the photocathode varies in the range [13,26]mm.*

the size of the electron spot decreases as the distance between photocathode and SiPM increases. The initial position of the SiPM (x=13mm) and the final ones (x>20mm) represent the two extreme situations that should be avoided: in the former case the focusing is too weak and as a consequence the spot is larger than the SiPM area leading to a reduction of the PDE; in the latter case the focusing is too strong and the spot is too squeezed leading too a reduction of the linearity.
The ideal case is the one with a flat distribution. Taking into account a sample of 10000 photoelectrons and a 50μm cell size, the photoelectron average per cell is 125 in the ideal case.
Therefore, the position of the SiPM in which the spot size is better cut to

fit the SiPM area and the distribution of the electrons in the spot is sufficiently uniform results to be x= 16 mm. In this configuration the spot size is expected to be $\sim 3.2\, mm\varnothing$ with a distribution that is flat almost on all the SiPM surface except for a limited central area.
For this position the transit time and the transit time spread have been evaluated to be $TT \simeq 2.6\, ns$ and $TTS \simeq 0.5\, ns$ respectively, see fig. 4.5.

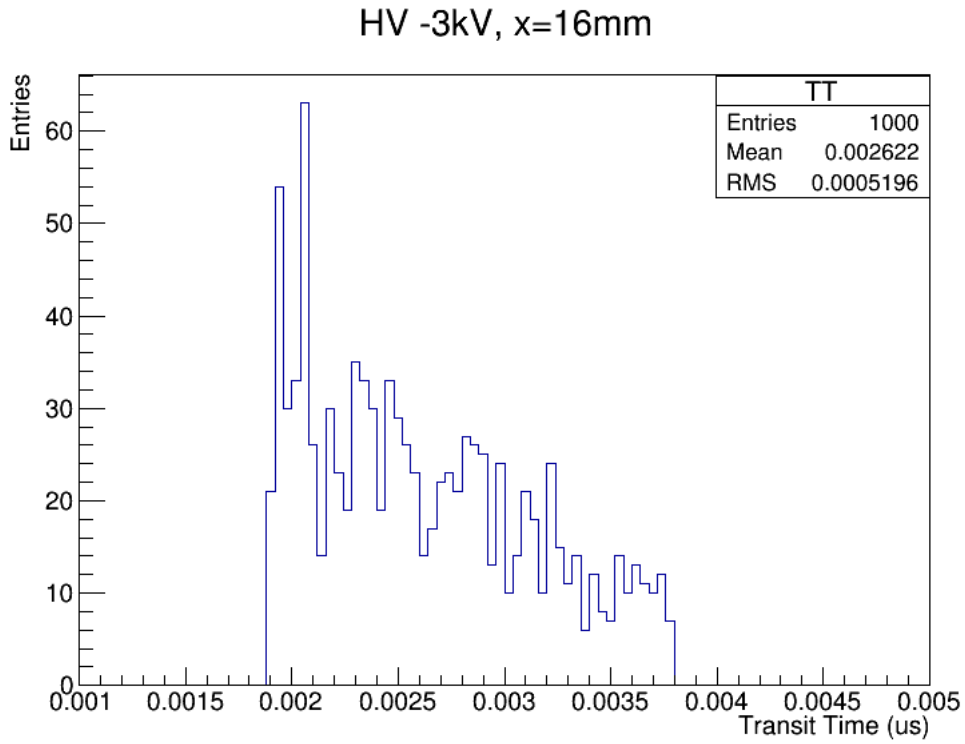

Figure 4.5: *Histogram of the transit time of the electrons in the path between the photocathode and the SiPM. The parameters used in the simulation are HV = -3 kV and x = 16 mm.*

Once fixed the SiPM position to 16 mm, the same study has been done for HV = [-3, -8.5] kV. Negligeable changes in the spot properties have been observed by varying HV when the SiPM position is fixed (see fig. 4.6). On the other hand, a reduction of the transit time and of the TTS has been observed as the HV increases. These last observations have a particular relevance for the VSiPMT prototype, meaning that the HV can be incresed to obtain a faster device and it has no consequence on the focusing and so on both the PDE and the linearity of the device.

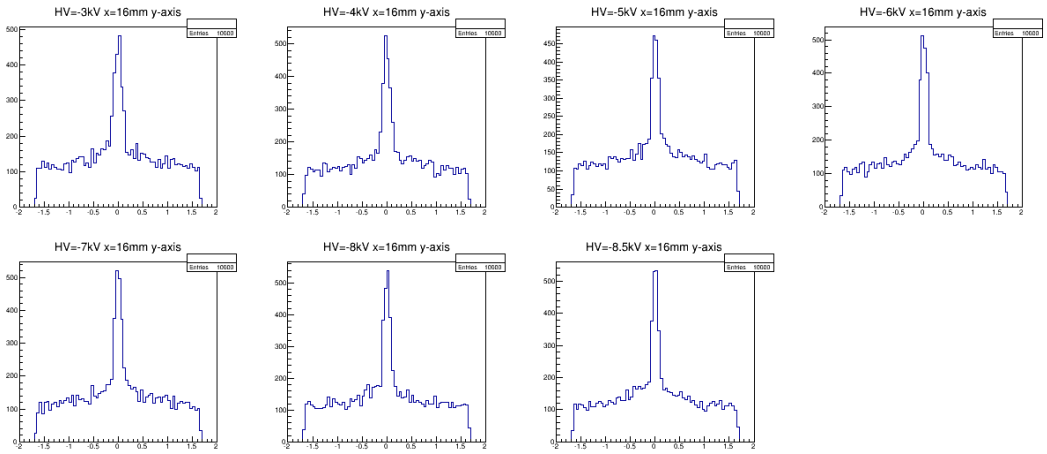

Figure 4.6: *y-axis distribution plot when the SiPM distance from the photocathode is set to 16mm and the HV varies in the range [-3,-8.5]kV.*

4.2 The selected SiPM

As already said in section 2.3, in order to allow a correct operation of the VSiPMT is necessary to design a custom SiPM specifically for this application. Indeed, a standard SiPM needs some modification in order to be operated as electron detector, it should be:

- windowless;
- p over n type;
- circular shaped.

In VSiPMT, high voltage between photocathode and SiPM is required to drive photoelectrons inside the SiPM. As a consequence, the latter must be windowless in order to minimize the threshold energy required to allow the photoelectrons entrance into the silicon bulk and the consequent production of a signal. At present, windowless SiPMs are produced by Hamamatsu, SensL and FBK.
In order to maximize the triggering probability, the SiPM needs a p over n junction. In this configuration, indeed, the photoelectron ionization range lies in the p^+ region allowing the ionized electrons to trigger the Geiger avalanche with high efficiency.
Finally, a circular shape will allow to find the best fit between the SiPM and the photoelectron spot and as a consequence to maximize linearity and PDE and to minimize the dark counts rate.

A detailed analysis has been conducted between the three above mentioned companies, on the basis of these possible modifications and also taking into account that a SiPM with very good performances (low dark rate, high dynamic range, fast response) and a reasonable price is preferred.
The selected SiPM is an MPPC S10943-3360(X) realized by Hamamatsu. It has been fully characterized with a light source before being used in the VSiPMT [28].

4.2.1 V-I Curve

As first step a V-I curve of the device has been done, in order to find the operating voltage. Figure 4.7 shows the characteristic V-I curve of the device

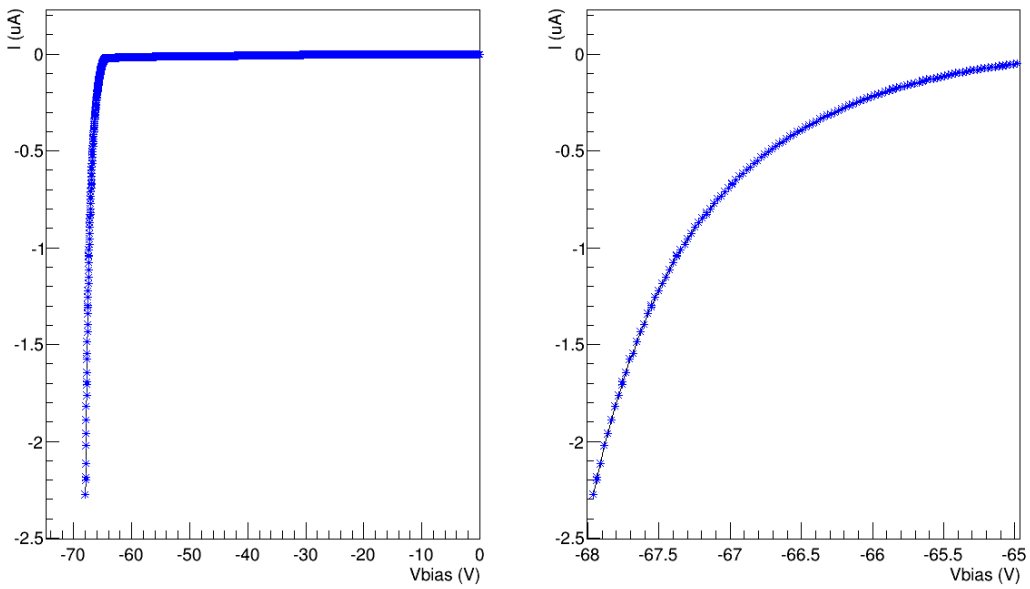

Figure 4.7: *LEFT: V-I curve of the selected SiPM: MPPC S10943-3360(X). RIGHT: Zoom of the V-I curve in the region where Geiger avalanche starts.*

and a zoom in the region where Geiger avalanche starts. The point where the curve flexes has been evaluated and the operating voltage has been set at that value, in this case 67.2V.

4.2.2 On-detector electronics: the amplifier

SiPMs and, as a consequence, VSiPMT are current sources with an high nominal internal gain ($\sim 10^6$). Neverthless, depending on the experiment

requirements a voltage readout could be preferred with respect to a current readout. In this situation, a conversion of the SiPM output current to a proportional voltage is required.
With this aim, two designs for a custom amplifier have been studied in order to find the best configuration. They are both based on the current-to-voltage conversion made by an operational amplifier and, respectively, forsee a current and a voltage feedback op-amps.
The general design of the circuit is shown in fig. 4.8. A low noise circuit is

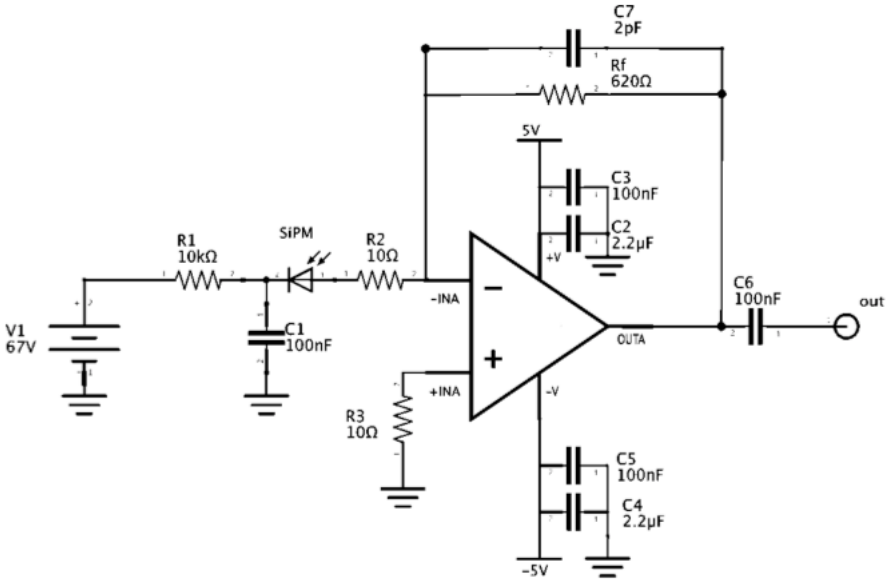

Figure 4.8: *General scheme of the amplification circuit.*

necessary to properly analize the device features during the characterization phase that will follow. Since op-amps with high bandwidth integrate a large amount of noise, several op-amps have been considered with different bandwidth and slew rate, see table 4.1: The amplified output SiPM signal shape of all the configurations has been compared. Three parameters have been observed: the electronic noise, the rise time and fall time. The two latters have been listed below in addition to the peak height, see table 4.2. Some minor revisions of the circuit have been done in each configuration.
From this study emerges that the TSH3001I op-amp is the best solution in terms of noise, timing and gain.

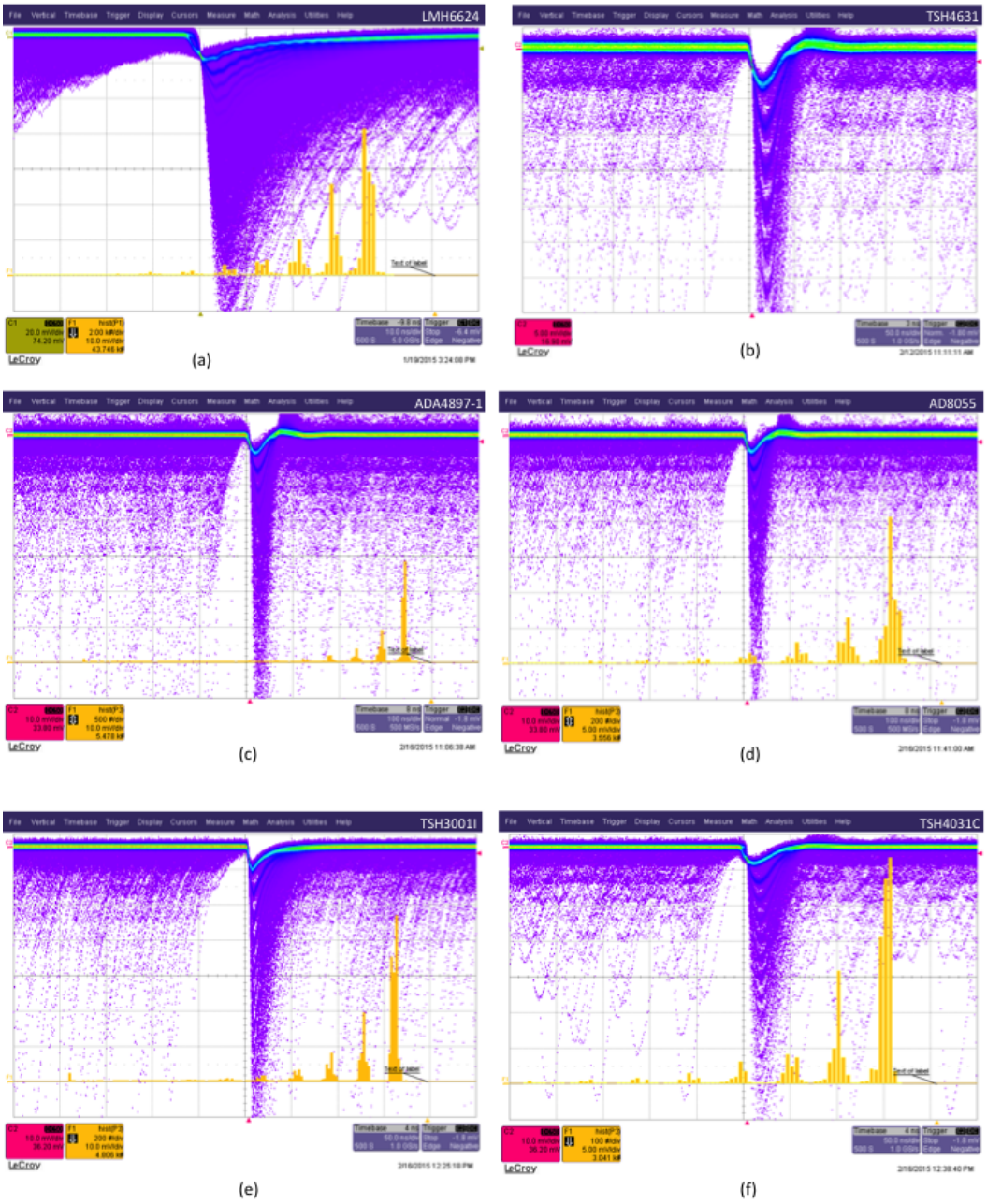

Figure 4.9: *Oscilloscope printscreen of the amplified SiPM signal in all the circuit configurations.*

Op-amp	Bandwidth (MHz)	Slew Rate (V/μs)	Output
LMH6624	1500	400	4.9a
TSH4631	325	900	4.9b
ADA4897-1	230	120	4.9c
AD8055	300	1200	4.9d
TSH3001I	420	6500	4.9e
TSH4031C	100	100	4.9f

Table 4.1: *Table of the main characteristics of the tested op-amps.*

Op-amp	Rise Time (ns)	Fall time (ns)	Peak height (mV)
LMH6624	4	13	7
TSH4631	10	38	5
ADA4897-1	13	27	5
AD8055	11	28	5
TSH3001I	4	15	10
TSH4031C	7.5	14	5.2

Table 4.2: *Table of the main characteristics of the SiPM readout signal for all the tested op-amps.*

4.2.3 Main characteristics of the selected SiPM

Figure 4.10 shows the raw signal and the output height spectrum of the MPPC S10943-3360(X), located into a dark box and and powered at the selected bias voltage, V_{bias} = 67.2V. The MPPC is read by an oscilloscope which is triggered in synch with the dark pulses of the MPPC. The responses

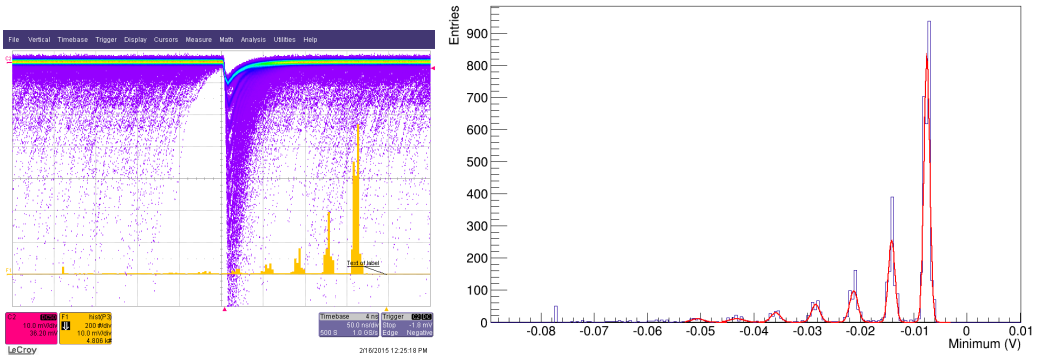

Figure 4.10: *LEFT: MPPC S10943-3360(X) raw signal. RIGHT: the related height spectrum.*

for multiple triggers are overlaid in the figure. The related height pulse spectrum shows well separated peaks.
This indicates that the gain of each pixel is uniform, demonstrating as expected the excellent photon counting capability of the device.
Keeping the MPPC in this conditions the dark count rate has been measured at different signal threshold levels. Results are listed in table 4.3. The gain

Thr (pe)	**Dark Rate (kcps)**	σ **(kcps)**
0.5	371	29
1.5	195	13
2.5	113	39
3.5	69	19
4.5	42	14
5.5	27	10
6.5	17	9

Table 4.3: *Table of the MPPC S10943-3360(X) dark count rate at different peak threshold levels.*

of the MPPC is measured by lighting it with a pulsed laser. The general scheme of the experimental setup is shown in fig. 4.11.
The MPPC and the amplifier are located into a dark box. The laser is pulsed at a typical frequency of 100 kHz, and the emitted light wavelenght is 407 nm. The laser output window is connected to two beam splitters in order to reduce the beam intensity and control, for very low intensities, the number of photons. The output optical power is measured using a Newport mod. 815 power meter having a sensitivity of 1 pW.
The gain of the MPPC has been measured at different bias voltages of the device. With this aim the distance between two consecutive peaks (1-2 pe, 2-3 pe, 3-4 pe, ...) have been measured and a weighted average of them, V_{out}, has been calculated. The gain, G, has been obtained as:

$$G = \frac{V_{out} \cdot ROI}{R_f \cdot e} \tag{4.1}$$

where,

- $ROI = 50\,ns$ is the selected region of interest for the measurements;
- $R_f = 1\,k\Omega$ is the feedback resistor of the amplifier circuit;
- $e = 1.6 \cdot 10^{-19}\,C$ is the electron charge.

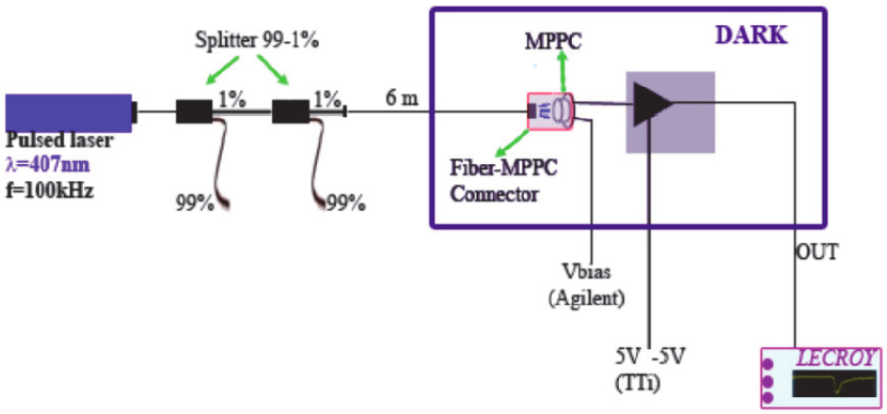

Figure 4.11: *Schematic view of the experimental setup for the characterization of the MPPC S10943-3360(X).*

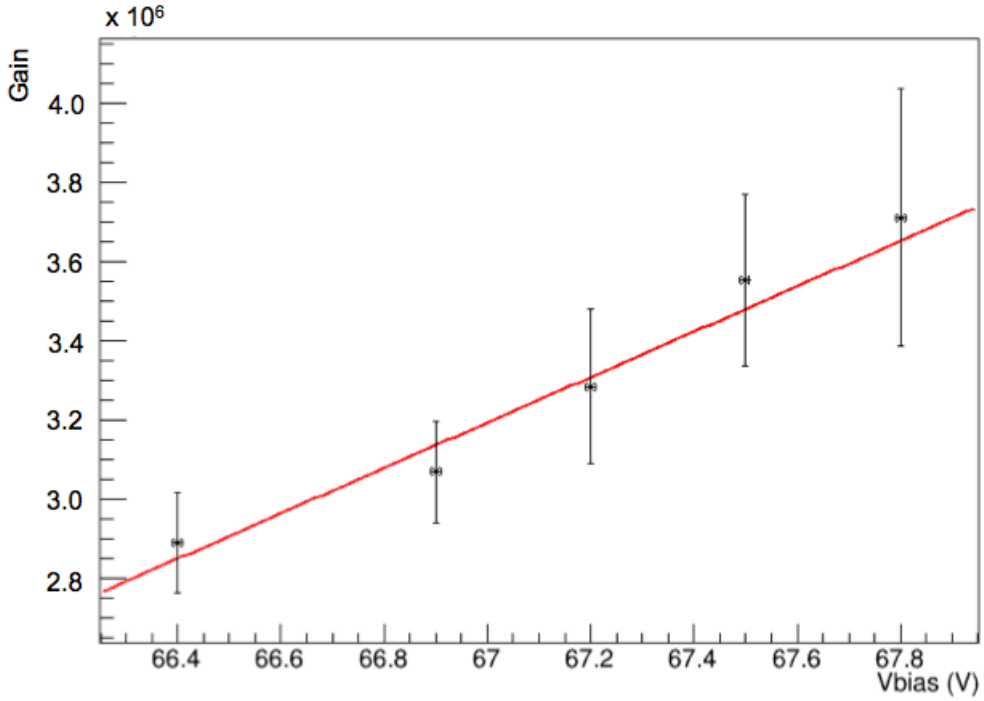

Figure 4.12: *Plot of the MPPC gain with respect to the bias voltage.*

The results obtained have been reported in fig. 4.12. The gain has been directely measured to be $G_{meas} = 3.28 \cdot 10^6$ when the bias voltage is set to

67.2 V, and it has then been exstimated by using the linear fit

$$G = 6.66 \cdot 10^5 \cdot V_{bias} - 4.14 \cdot 10^7 = 3.3 \cdot 10^6$$

.

4.3 Study and realization of a photocathode

For the realization of the prototype the Cesium Iodide (CsI) has been selected as photocathode material, because differently from other materials (see section 2.2) it is not sensitive to the oxigen present in the air and therefore it allows an easier handling in the assembling phase [29]. Neverthless it's well known that CsI is highly hygroscopic, so to ensure a good performance of the photocathode some precautions to dry the working environment should be taken.
The parameters to study to obtain a good photocathode are: conductive layer thickness and material, CsI film thickness and distribution [30].

4.3.1 The entrance window

The starting point for the realization of a photocathode is to choose the substrate where to deposit the photosensitive material. Since the VSiPMT is a transmission mode photodetector, the photocathode substrate coincide with the interface with the incoming light, known as entrance window. It is, therefore, necessary that the substrate material is transparent in the spectrum region of interest.
As said previously, the CsI spectral response has a cut-off around 200nm, meaning that it operates in the VUV region.
Two different materials have been selected as entrance window for the realization of the photocathodes: quartz and MgF_2. Both the windows have a circular shape with 25mm ∅ and a thickness of 2mm for the MgF_2 and 3mm for the quartz. Their transparency has been analyzed using the setup in fig. 4.13. The monocromator selects the wavelength of the light coming from the deuterium lamp allowing to scan a wide range of wavelengths. The collimated light is sent to a NIST calibrated photodiode, read by a picoammeter. The photodiode is mounted on a plastic pillar which provides a special mounts for the windows, see fig. 4.14. The transparency of both the material have been evaluated by measuring their transmittance, as follow:

$$T = \frac{I_{win}}{I_{NIST}} \cdot 100 \tag{4.2}$$

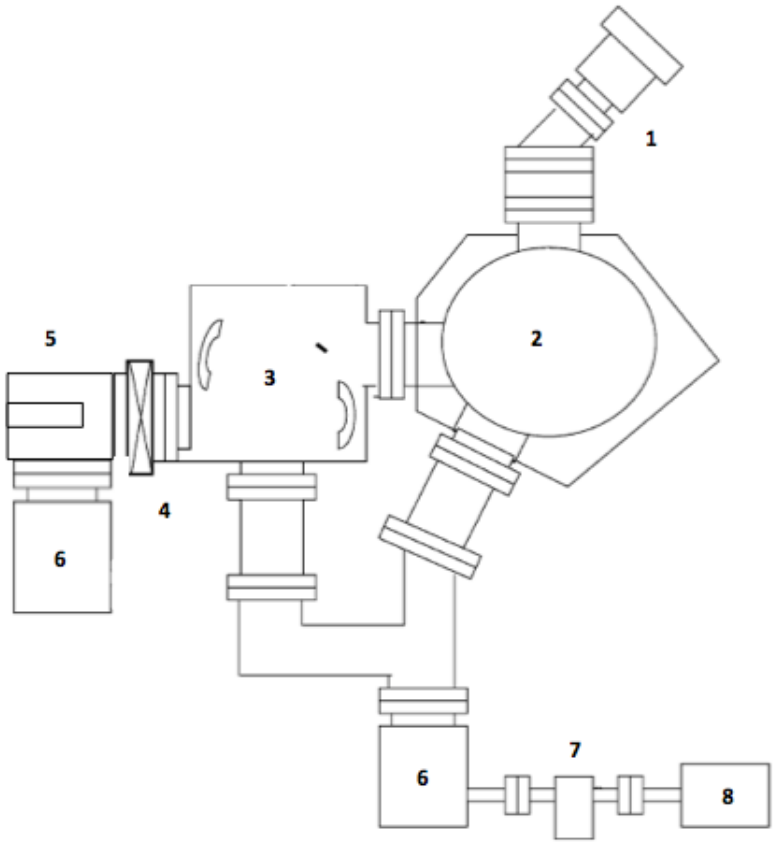

Figure 4.13: *Scheme of the experimetal setup used to measure the trasmittance of the entrance windows.* ***1.****Deuterium Lamp,* ***2.****Monocromator,* ***3.****Collimator,* ***4.****Lock Gate,* ***5.*** *NIST calibrated photodiode,* ***6.****Turbo Pump,* ***7.****Trap,* ***8.****Rotative Pump*

where, I_{NIST} is the photocurrent generated on the photodiode directly from the light of the deuterium lamp, while I_{win} is the photocurrent generated on the photodiode from the light filtered by the window. The measurement has been repeated for all the wavelenght in the range [130-202]nm each 2nm.
The results are plotted in fig.4.15. Although quartz transmittance is higher than MgF_2 one, this latter has a wider range of transmittance and so it allows to enlarge the spectral range of sensitivity of the photocatode that will be deposited on it. For this reason, quartz windows have been used for the study of the conductive layer and photocathode thickness, while the MgF_2 windows have been set aside to deposit the photocathode that will be mounted in the prototype.

Figure 4.14: *Picture of the quartz window mounted on the support.* ***1.****Plastic Pillar,* ***2.****Special mounting for the windows,* ***3.****Quartz window,* ***4.****NIST calibrated photodiode.*

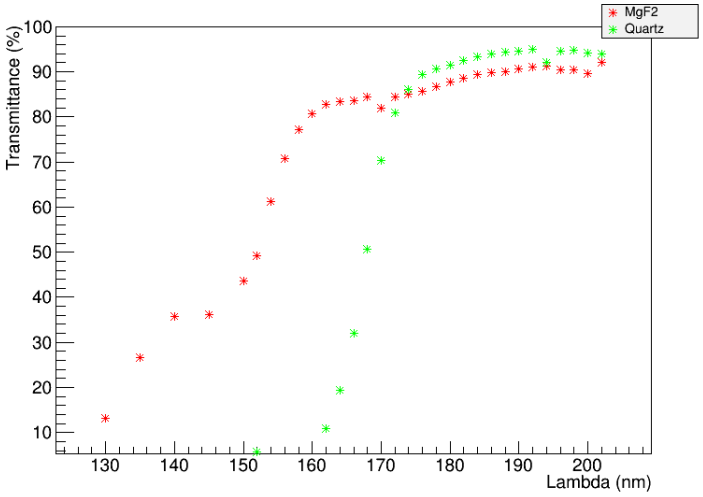

Figure 4.15: *Plot of the transmittance measurement of both the MgF_2 and the quartz windows. The estimated error is less than 1% and is not graphically reported.*

4.3.2 Study of the conductive layer

Since the CsI is an insulating material, a layer with a good electric conductivity and very high transparency to the VUV photons is required [31]. Several materials with different thickness have been deposited by using an Ion Beam Sputtering technique, in a dedicate chamber at the Physics Department of the University of Bari "Aldo Moro", see fig.4.16. An ion beam is sent towards

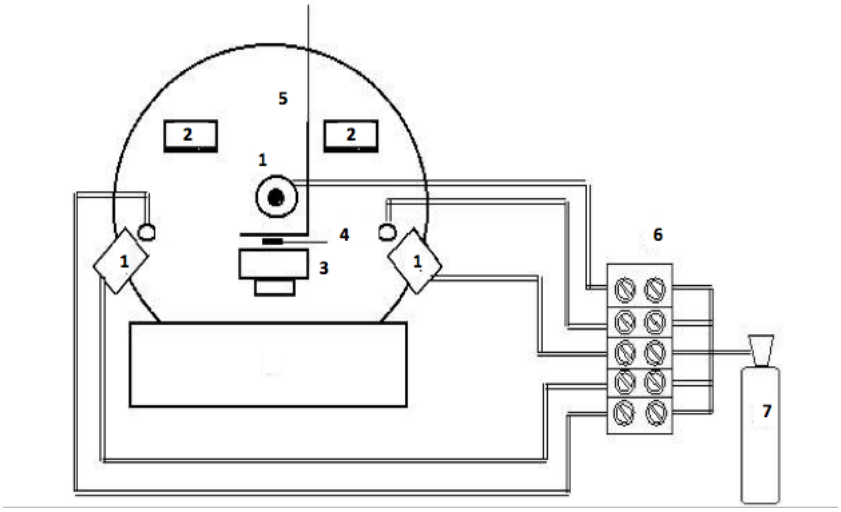

Figure 4.16: *Scheme of the ion beam sputtering chamber.* ***1.****Ion source,* ***2.****Target material,* ***3.****Rotating sample holder,* ***4.****Quartz microbalance,* ***5.****Removable mask,* ***6.****Gas control unit,* ***7.****Argon gas*

a solid target of the desired material, the extracted atoms are deposited on the quartz window. A calibrated quartz microbalance is used to monitor online the thickness of the deposited material.
To remove organic surface contamination, windows have been chemically cleaned with a standard procedure just prior to their introduction into in the IBS chamber.
A list of the prepared samples and their characteristics is reported in table 4.4. Where ITO is Indium Tin Oxide and NiC is a superposition of Nichel and Carbon. Samples with the same number have been realized during the same deposition exploiting the rotation of the sample holder (n.3 in fig.4.16), except sample n. 1533ox. In this particular case, it refers exactely to the sample 1533. The specification "*ox*" stays for "*oxigenate*". Actually since during the sputtering process the oxigen present in ITO is the most volatile element of the compound, the sample n. 1533 has been left for $\sim 12h$ in an oxigenate oven at the temperature of $400°C$.

Sample	Material	Thickness (nm)
1532	ITO	10
1533	ITO	5
1533ox	ITOox	5
1534	Ni	5
1534	C	5
1535	Ni	3
1536	NiC	3 (NiC)+ 0.5 (Ni)
1537	NiC	2.5 (C)+ 0.5 (Ni)
1538	Ni	1
1538	Ni	3

Table 4.4: *Table of the samples prepared to choose the consuctive layer.*

The samples n. 1536 and n.1537 are made with the same elements but with a different procedure. For n. 1536, 3nm of Nichel and Carbon have been sputtered simultaneously using two targets and two ion sources, after 0.5nm of Nichel have been deposited on the NiC compound. For n. 1537, instead, 2.5nm of Carbon have been deposited on the window and a 0.5nm thick layer of Nichel has been added.
The transmittance of each sample has been measured as in eq.4.2, see fig.4.17. For the sake of clarity the plot 4.17 has been subdivided in three plots depending on the material used for the conductive layer, see fig 4.18, 4.19 and 4.20.

Taking into account the transparency and the conductivity of the layers the selected samples as possible solution were: Ni 1535, NiC 1536 and NiC 1537.

4.3.3 Study of the optimum thickness of the photocathode

For semitransparent photocathodes, the thickness of the CsI film has a critical optimum value. If the thickness exceeds the escape depth of the electrons, the quantum efficiency is unnecessarly reduced because photoelectrons produced by photons absorbed beyond the escape depth cannot be emitted into the vacuum. The probability that a photoelectron generated at a depth x from the surface can escape in the vacuum is known to be:

$$G(x) = T \cdot exp(-x/L) \tag{4.3}$$

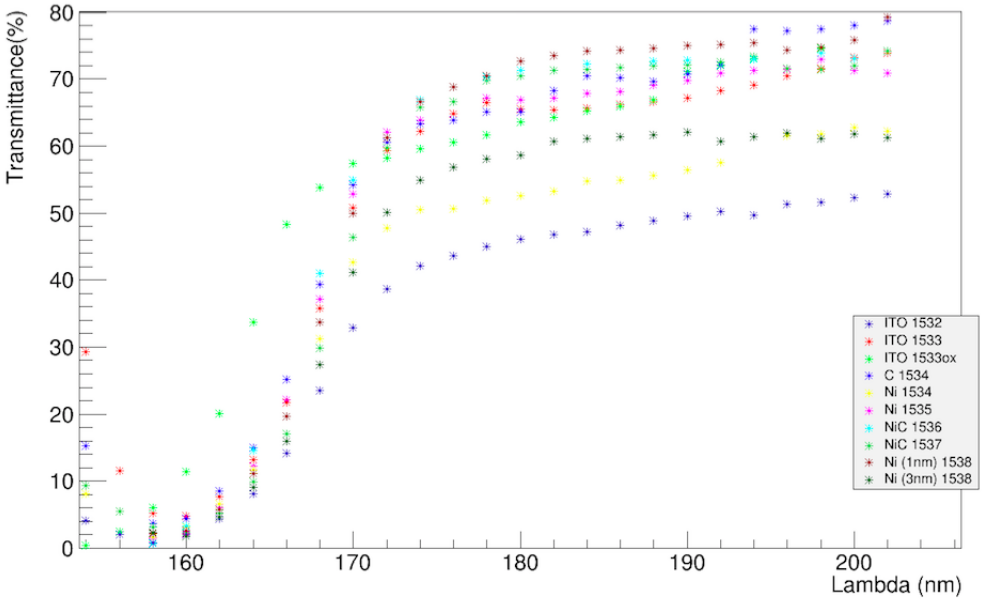

Figure 4.17: *Plot of the conductive layers transmittance function of wavelength.*

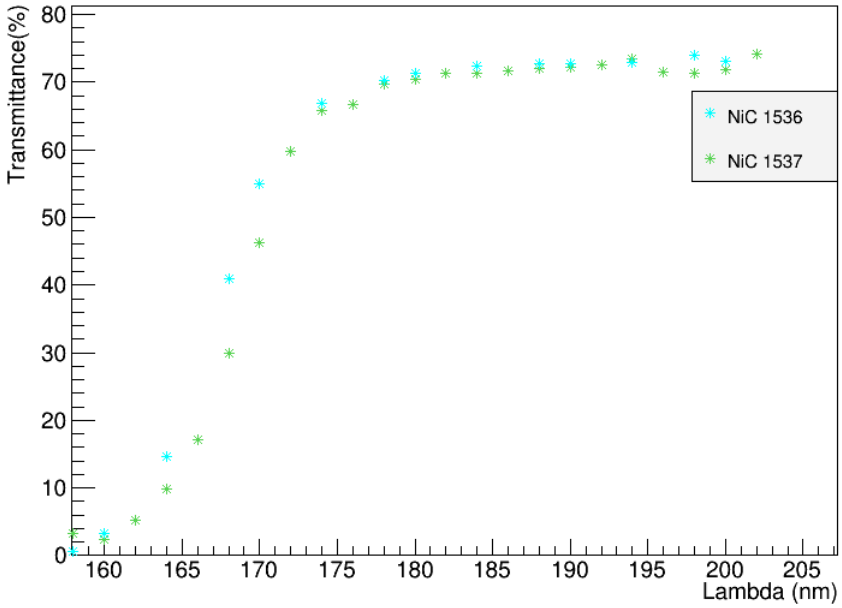

Figure 4.18: *Subplot of the conductive layers transmittance function of wavelength.*

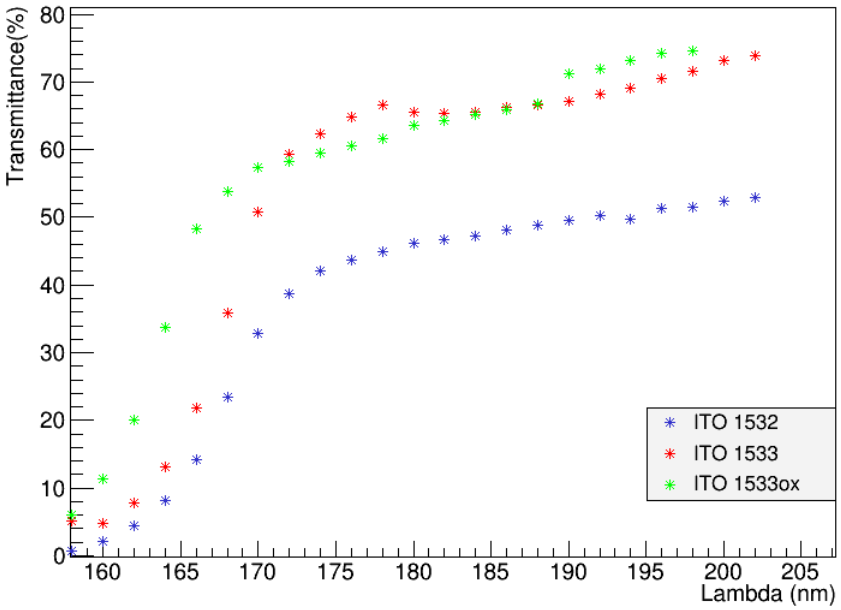

Figure 4.19: *Subplot of the conductive layers transmittance function of wavelength.*

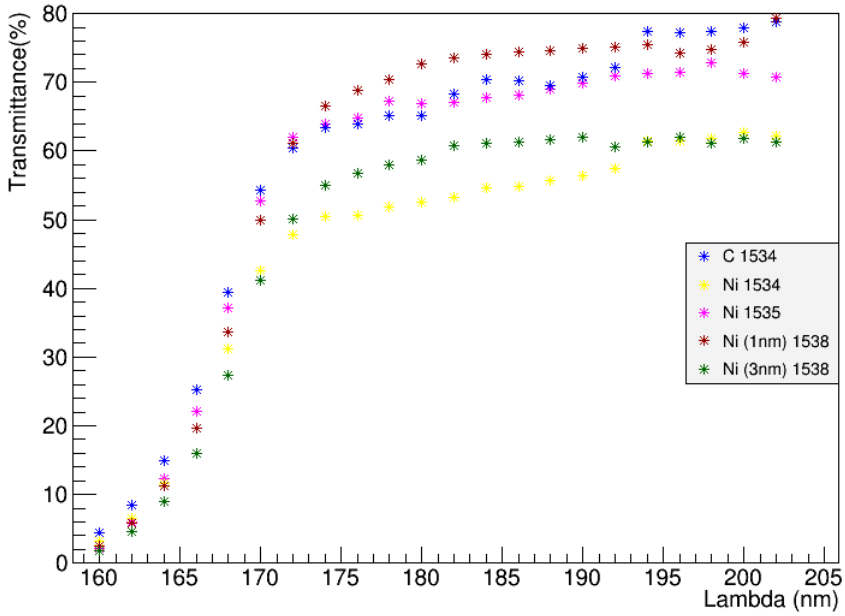

Figure 4.20: *Subplot of the conductive layers transmittance function of wavelength.*

where T is the probability for an electron produced near the surface and L is the electron escape length. The probability G has been calculated by Akkerman et al. [32], for 1 eV energy photoelectron in conduction band. The result shows that the probability decay to a value smaller than 7% for a photocathode thickness of about 40 nm. This means that the optimum thickness for a photocathode is of the order of 10 nm.
On the other hand, an additional parameter influences the quantum efficiency of the photocathode: the absorption length of the radiation in the material, *d*. If the thickness of the photocathode is much smaller than the escape depth, the quantum efficiency can be reduced because a fraction of the light can be transmitted rather than absorbed.
Although a small thickness gives rise to the enhancement of the escape probability, it also leads to a reduction of the absorbed radiation.
It is evident from this discussion that the optimum thickness of a semitransparent photocathode is not a unique number characteristic for a particular material. As a consequence, an additional study to identify this parameter is required.
With this aim, a set of CsI thin films have been grown by Thermal Evaporation technique, by using a CsI 99.999% pure powder, in a dedicate vacuum chamber, available at the Physics Department of the University of Bari "Aldo Moro" [33].
Only two different thickness have been explored, 30 and 20 nanometers, since with the second attempt the expected QE has been achieved. The QE has been evaluated for each sample as follow:

$$QE = \frac{I_{out}}{I_{in}} \cdot QE_{PD} \cdot 100 \tag{4.4}$$

where I_{in} and QE_{PD} are respectively the photocurrent and the quantum efficiency of the calibrated photodiode, while I_{out} is the photocathode current. In order to measure I_{out}, the photocathode is mounted on a dedicated frame (fig. 4.21) that will be placed into the same system used for the the transmittance measurement (fig. 4.13). The photocathode is fixed on a PCB frame and a picoammeter is connected to the conductive layer. On the back side of the PCB frame (fig. 4.21 b) a wire grid is set to 90V. The photons coming from the deuterium lamp impinge on the photocathode extracting photoelectrons. The photoelectrons are collected on the wire grid and, as a consequence, a positive current is read by the picoammeter connected to the photocathode. The measurement is made at the preassure of 10^{-4} mbar. In fig 4.22, the results of the absolute QE are shown. As evident, a 20nm thick CsI photocathode can achieve $\sim$ 18% of QE at 160nm. To evaluate which conductive layer is the best match for the photocathode, CsI films

Figure 4.21: *QE measurement frame. (a)Front side: the photocatode is fixed on a PCB frame and the consuctive layer is connected to a picoammeter. (b)Back side: a wire gride is connected to HV.*

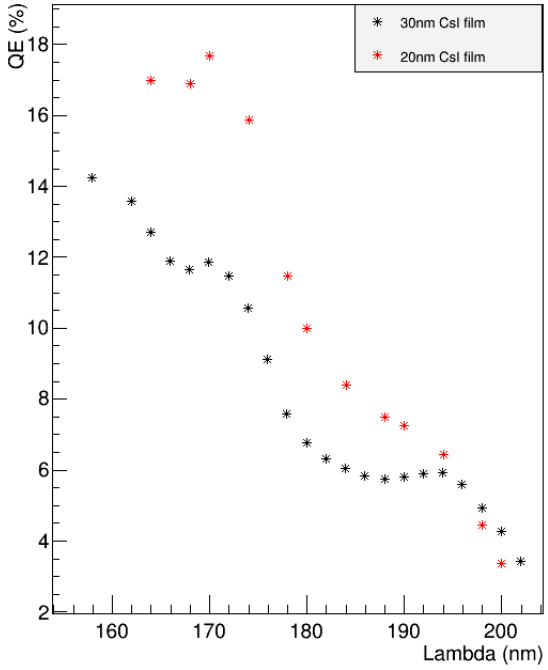

Figure 4.22: *Plot of the results of the QE measurement of CsI films with different thickness, 20 and 30nm.*

have been deposited on the various substrate listed in table 4.4. The quantum efficiency (fig. 4.23) and the transmittance (fig. 4.24) of each sample has been measured. In order to do the final choise, a direct comparison of all the possibilities has been done taking into account both CsI quantum efficiency, both the conductivity of the substratum and the overall transmittance. For the sake of clarity an additional plot with the several possibilities is reported.

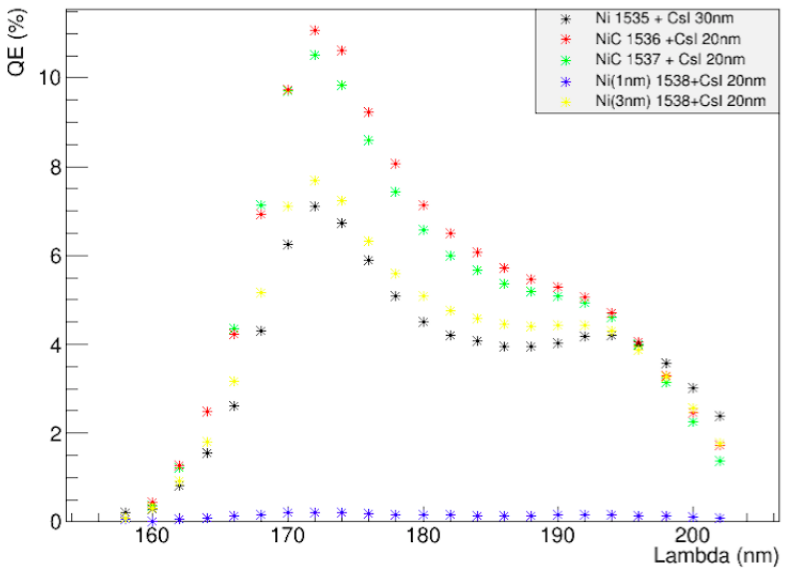

Figure 4.23: *QE plot of CsI films deposited on several conductive layer.*

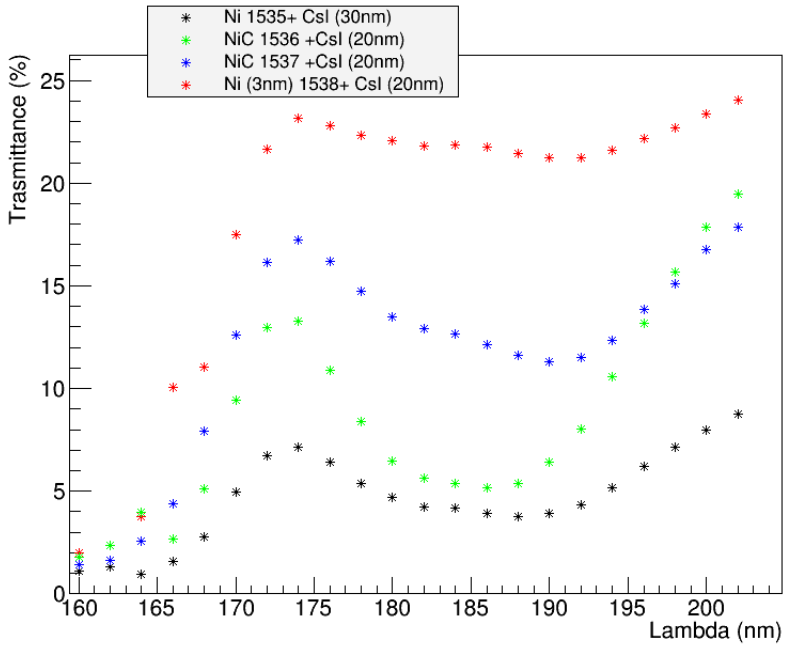

Figure 4.24: *Transmittance plot of CsI films deposited on several conductive layer.*

The three curves in fig. 4.25 have been obtained by plotting the quantum efficiency of two photocathode samples. The photocathode thickness is 20 nm

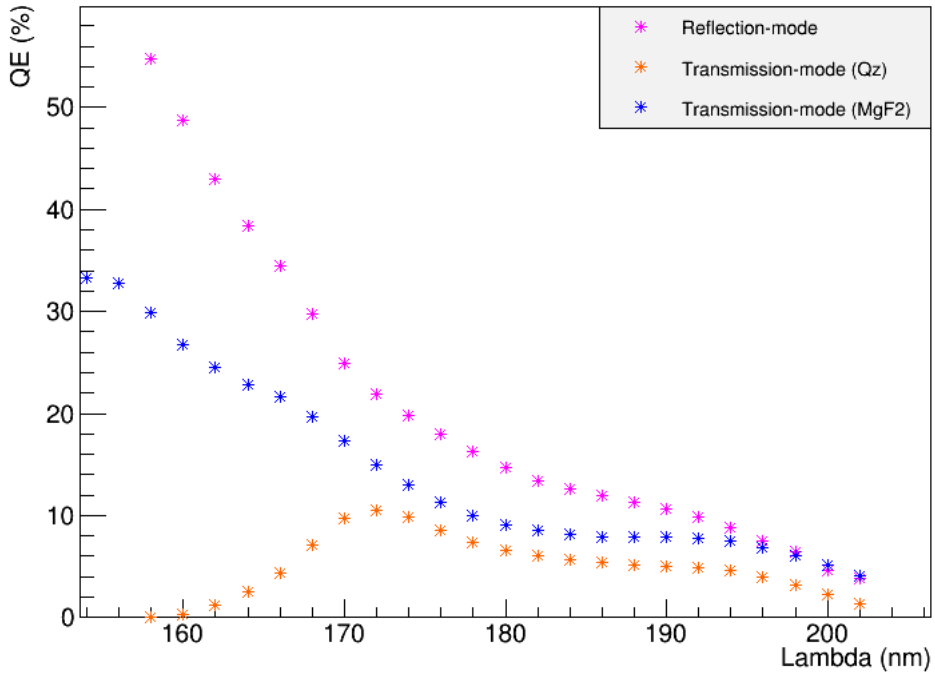

Figure 4.25: *QE plot of the CsI photocathode on both the substrates in reflection and in transmission mode.*

in both cases and the conductive layers are made by 2.5 nm of Carbon and 0.5 nm of Nichel. The two samples differ because of the entrance window. It is glaring looking at the plots that using a MgF_2 window (blue curve) is more fruitful than using a Quartz window (orange curve). The first, effectively, allows to push the photocathode spectral response towards lower wavelenghts and as a consequence to obtain an higher quantum efficiency.
An additional curve has been obtained by measuring the quantum efficiency using both the photocathodes in reflection mode. No considerable differences have been obtained by using the two semples in reflection mode, so only the one relative to the Quartz substrate has been reported in fig. 4.25.
At the conclusion of this study the choise for the photocathode that will be used in the final assembly has the following characteristics:

Window material : MgF_2;

Conductive layer material : Ni, C;

Conductive layer thickness : C$\rightarrow$ 2.5nm, Ni$\rightarrow$ 0.5nm;

CsI film thickness : 20nm.

Chapter 5

Measurements on the pre-prototype

In the previous chapter a description of the preliminary work that has been done on the single parts of the VSiPMT has been presented. Once the several parts that will compose the VSiPMT have been chosen, an intermediate phase between the preparation of the parts and the final assembly is necessary.
In view of the final assembly of the VSiPMT, a test bench aimed at testing the focusing and the overall working principle has been arranged in the DAFNE Light facility available at Frascati National Laboratories (LNF).

5.1 The pre-prototyping phase

To test the feasibility of a 1-inch VSiPMT with the characteristics chosen in the previous chapter, a pre-prototype has been designed and realized. The idea is to have a structure where the single parts of the VSiPMT can be positioned and modified.
With this aim, a special flange has been designed, see fig. 5.1. The flange, realized at the mechanic's workshop available at the Physics Department of the University of Naples "Federico II", shows a central opening that is the seat of a micrometric movable support for vacuum application. The MPPC is positioned on the movable support. The latter allow to modify the position of the MPPC.
In addition, three vacuum feedthrough are foreseen. These allow to supply voltage both to the photocathode both to the MPPC and to read the MPPC signal.

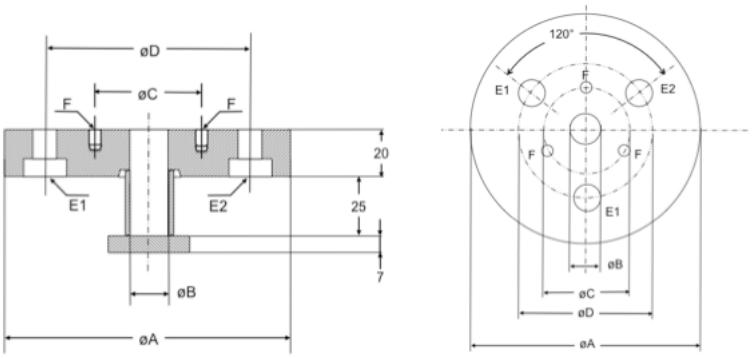

Figure 5.1: *Design of the flange. RIGHT: side section of the flange. LEFT: top view of the flange.*

Finally, three threaded metal bars are installed on the flange as support for the photocathode holder. The photocathode holder, instead, is realized

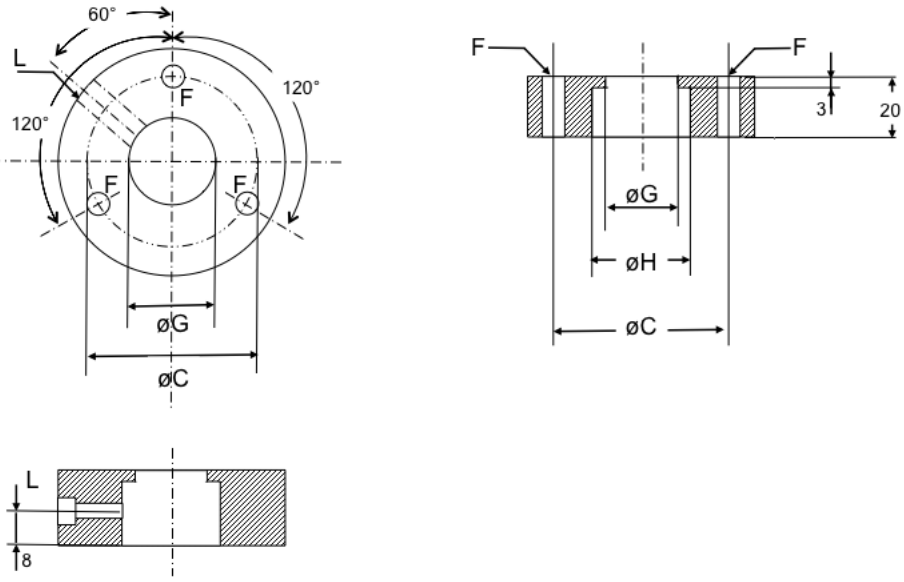

Figure 5.2: *Design of the photocathode holder. RIGHT: front view of the holder. LEFT and BOTTOM: side section of the holder.*

in teflon (see fig. 5.2) to guarantee the electrical insulation between the photocathode and the entire structure.

The photocathode is housed in the teflon frame together with a focusing ring. A side dig (fig. 5.2 bottom)is the seat of a screw that secure the focusing ring and supply the voltage at the same time.
The final structure is showed in fig. 5.3 and 5.4.

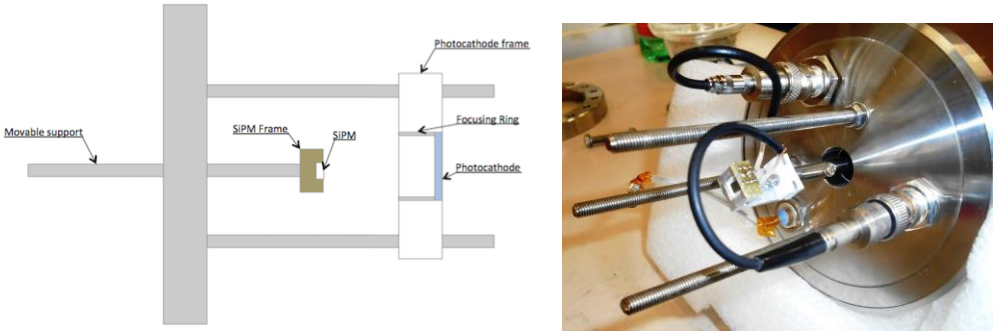

Figure 5.3: *RIGHT: scheme of the preprototype. LEFT: picture of the flange with the MPPC mounted on the movable support.*

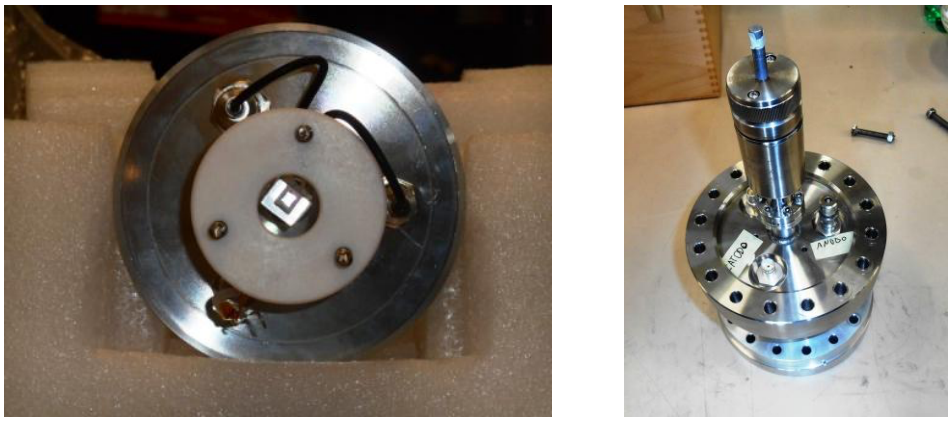

Figure 5.4: *RIGHT: picture of the photocatode frame mounted on the flange. LEFT: the preprototype assembled and vacuum sealed.*

5.2 The facility

DAFNE-Light is the Synchrotron Radiation Facility at the Laboratori Nazionali di Frascati (LNF) [34].
It offers the possibility to provide measurements both in continuous both in pulsed mode. The former solution is provided by a deuterium lamp, while the latter exploits the intense photon emission from Daϕne, the 0.51 GeV

storage ring circulating over 1 A of electrons. Three beamlines are dedicated to the VUV, visible and IR regions.
The test starts with the deuterium lamp and is used as benchmark for the following measurements with the synchrotron light.

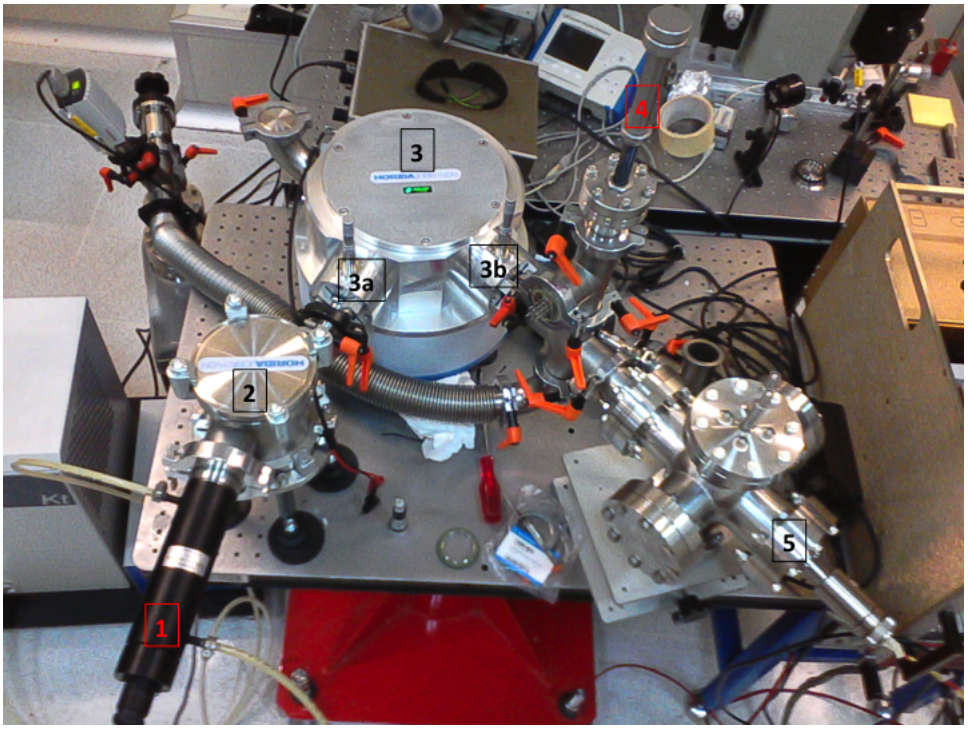

Figure 5.5: *Picture of the continuous mode test bench in the DAFNE Light Facility at Frascati National Laboratories.*

The test bench, see fig. 5.5 is equipped with:

1. a deuterium lamp;
2. a set of collimator mirrors;
3. monochromator, (a) entrance slit, (b) exit slit;
4. NIST calibrated photodiode mounted on a movable support;
5. pre-prototype.

The two slits placed respectively at the entrance and at the exit of the monochromator allow to control the light flux, while the monochromator allows to select the wavelenght. The calibrated photodiode is mounted on a

movable support in order to provide an online monitoring during the measurements, it is a $1 \times 1\, cm^2$ with internal gain 1. A cooling system is applied on the deuterium lamp and everything is kept under vacuum at $\sim 10^{-5} mbar$.

5.3 MPPC characterization in the VUV region

Since the MPPC under test is a custom device, it has an unexplored behaviour in the spectral region of interest. As already illustrated in section 2.3, a SiPM, and so the MPPC in use, is born as a light detector but is used in this application as an electron detector. Since a transmission mode VSiPMT exploits a semitransparent photocathode, a certain amount of photons, that are not absorbed by the photocathode, can hit the SiPM causing a prepulse, given that photons are faster than electrons.
So the first test consists into measure the MPPC response to the VUV light. A light beam in the wavelenght range [120, 400]nm has been sent first on the calibrated photodiode and then on the MPPC.
Both the devices are read with a Keythley 6847 picoammeter. The two currents are plotted in fig. 5.6. The spectral response, SR, of the MPPC is

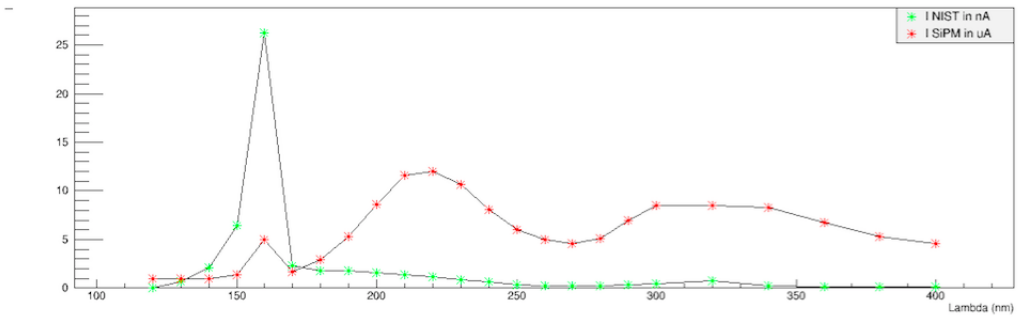

Figure 5.6: *Plot of the deuterium lamp spectrum read by the calibrated photodiode (green dots) and by the MPPC (red dots).*

obtained as follow:

$$SR_{MPPC} = \frac{I_{MPPC} \cdot QE_{pd}}{I_{pd} \cdot G_{MPPC}} \cdot \frac{A_{pd}}{A_{MPPC}} \tag{5.1}$$

Where I_{MPPC} and A_{MPPC} are respectively current and surface of the MPPC, while I_{pd} and A_{pd} are respectively current and surface of the calibrated photodiode. G_{MPPC} is the internal gain of the MPPC at 67.2 V.

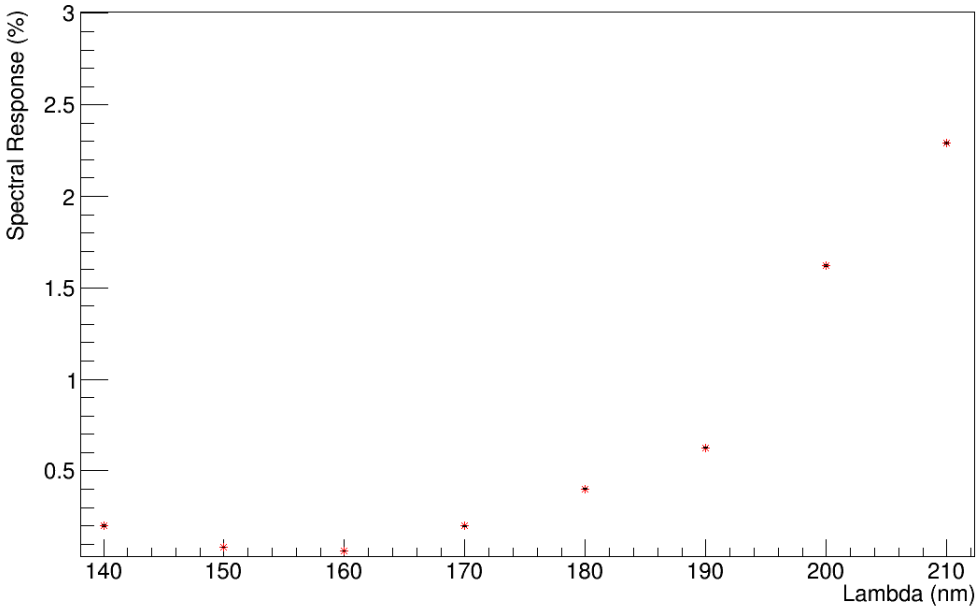

Figure 5.7: *Plot of the MPPC spectral response in the region of interest.*

The results obtained are plotted in figure 5.7. In the spectral region of interest [140,200] nm the response of the MPPC approaches zero for $\lambda < 180\,nm$. Therefore, there are no particular precautions to take for the following measurements.

5.4 Photocathode QE

Although in section 4.3.3 is expressely said that a MgF_2 substrate is preferred, an additional photocathode have been deposited at the Bari facility on a quartz substrate. The photocathode deposited on the MgF_2 substrate is addressed to the final assembly, while the one deposited on the quartz window is addressed to the tests on the pre-prototype because it is more robust. The photocathodes have been, then, transported to the Dafne light facility in a vacuum dryer with a preassure of $\sim$ mbar equipped with silica gel. The tests started two days after the deposition and, for practicality reasons, the photocathodes have been handled without any precaution for the humidity in the air. A degradation of the photocathodes and of their performances is, then, expected. For this motivation, the quantum efficiency of both the photocathodes has been measured at the moment of the production in Bari and also before the tests in Frascati.
With this aim, a PCB grid has been realized to be easily installed on the

flange described in section 5.1, see fig. 5.8. The photocathode, in trans-

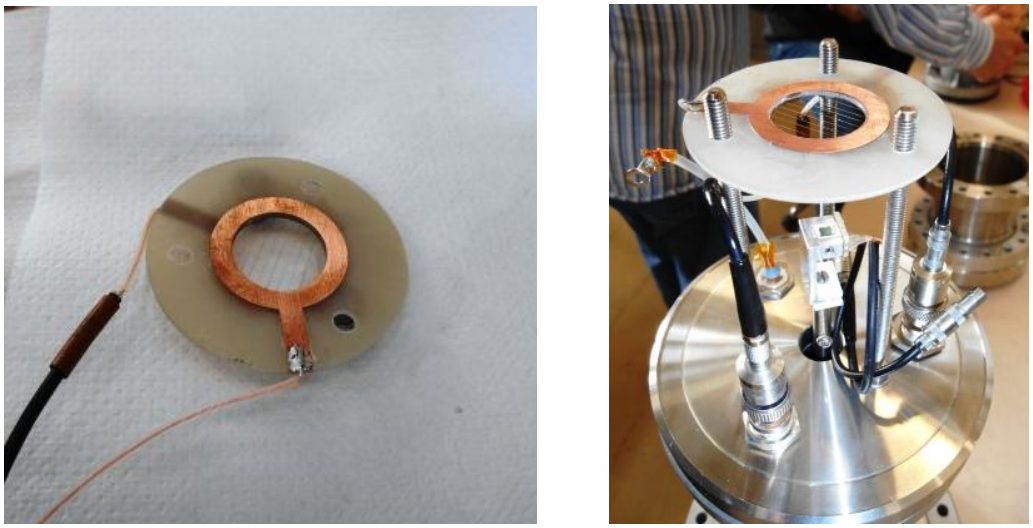

Figure 5.8: *LEFT: The PCB disc used to measure the quantum efficiency of the photocathode. RIGHT: The PCB disc istalled on the flange.*

mission mode, is placed on the top side of the disc. A copper ring on the PCB ensure the electrical contact that is read by the picoammeter. On the back side of the disk a metal grid is set to 90 V with the aim to collect the photoelectrons extracted by the photons coming from the deuterium lamp. Everything is kept at the preassure of $\sim 10^{-}5\,mbar$.
In fig. 5.9 and 5.10[1] are plotted the results of the measurements. In both cases is possible to observe a reduction of the quantum efficiency due to an improper handling of the photocathodes. As already said above, a high accuracy has been used to chose the individual parts and these measurements represent a preliminary test to check their compatibility. The real assembly phase of the VSiPMT will be done in an inhert environment with a controlled humidity in order to avoid the photocathode degradation.

[1]It is possible to observe a difference in the quantum efficiency of the sample 1606 showed here and the sample 1537 showed in fig. 4.25, despite of the two samples have been deposited following the same procedure and using the same materials. The highlighted difference is due to a different geometry adopted during the CsI evaporation process. The sample 1537 was actually mounted directely in correspondence of the crucible containing the CsI powder (optimum geometry), since it was the only sample loaded in the evaporation chamber. In the other case, instead, two photocathodes have been evaporated at the same time requiring a different geometry.

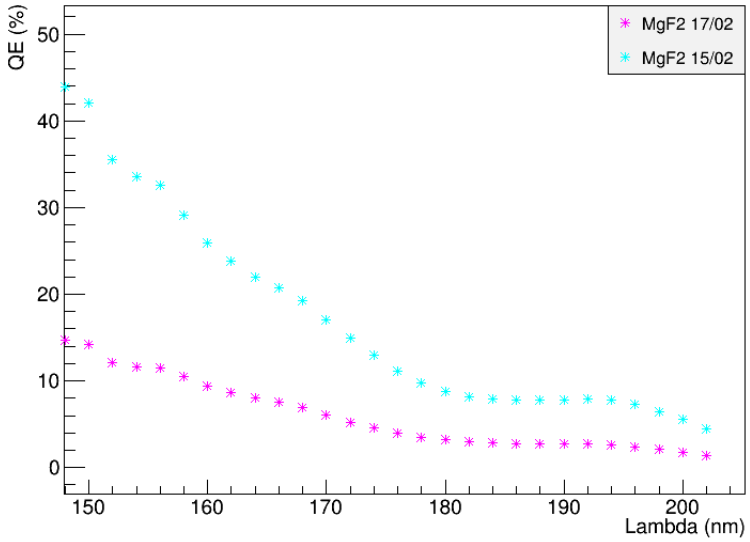

Figure 5.9: *Plot of the quantum efficiency of the photocathode deposited on the MgF_2 window. The measurement has been done on 15/02/2016 in Bari, the deposition-day, and on 17/02/2016 in Frascati, the tests starting day.*

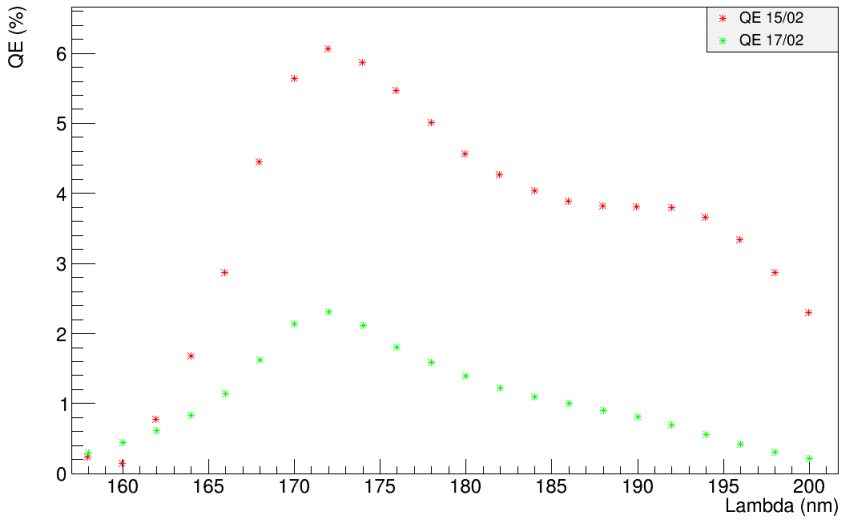

Figure 5.10: *Plot of the quantum efficiency of the photocathode deposited on the quartz window. The measurement has been done on 15/02/2016 in Bari, the deposition-day, and on 17/02/2016 in Frascati, the tests starting day.*

5.5 Pre-prototype operation check

Once the quantum efficiency of the photocathodes has been measured, the one deposited on the quartz window has been housed in the teflon frame to

start the measurements.
The first step was to check the proper operation of the pre-prototype. With this purpose the MPPC output current has been measured in two configurations:

1. the photocathode and the focusing ring are both off;
2. the photocathode and the focusing ring are both at -8.5 kV[2];

The MPPC is at 16 mm distant from the photocathode. The two readout currents are reported in fig. 5.11. As evident from the plot, keeping the

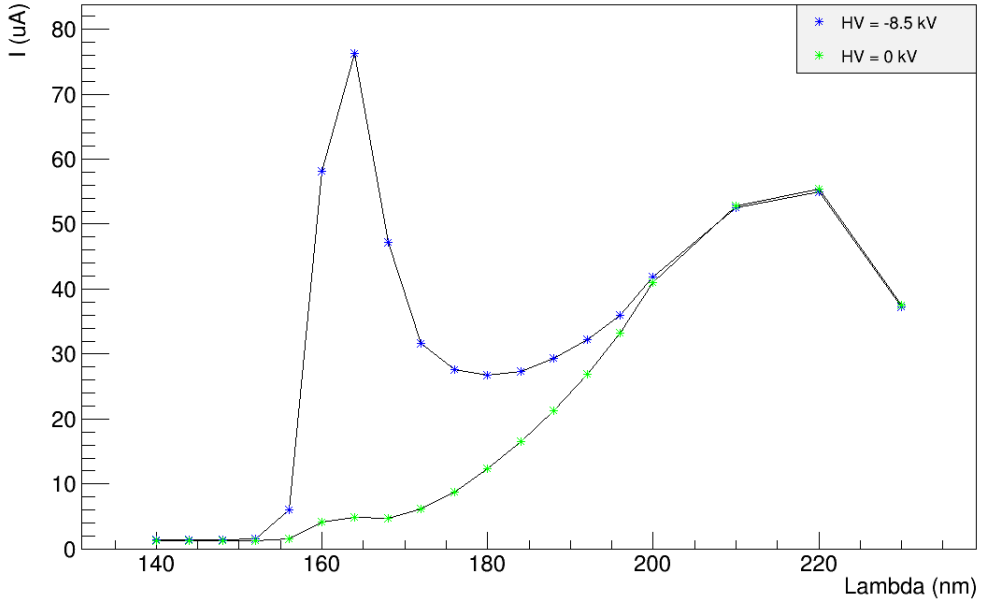

Figure 5.11: *Readout current plot.*

photocathode and the focusing ring at -8.5kV entails an increasing of the readout current in the photocathode sensitive region (blue line).
This result is the most important since it proof the proper operation of the pre-prototype and so it proof that a surface increasing of 57 times is achieved. Currently such an increasing of the sensitive surface can be achieved using SiPMs arrays. The weak point of the array is that a surface increase entails a growth of the dark rate. This measurement is a proof that for the first time a large area device has been realized, succeding into keep not only the

[2]The operating point selection is presented in section 5.9.

SiPMs detection features (as in the arrays case) but also the dark rate of a single SiPM. Therefore, the VSiPMT is equivalent to a SiPM array with a drastically reduced dark rate.
In the following additional measurements are presented to explore the pre-prototype features.

5.6 Dark Count Rate

The VSiPMT dark rate is expected to be essentially due to the MPPC. The dark count rate of the pre-prototype has been measured in two configurations: with the photocathode on and off. The results are reported in table 5.1 Negligible differences have been observed when the photocathode is off,

Thr (pe)	**Dark Rate (cps)**	σ **(kcps)**
0.5	1.45 M	0.12 M
1.5	325 k	32 k
4.5	36 k	1 k
9.5	1.5 k	0.1 k
14.5	72.9	16

Table 5.1: *Table of the MPPC S10943-3360(X) dark count rate at different peak threshold levels with the photocathode on.*

proving that the only contribution to the dark count rate of the overall device is actually given by the MPPC.

5.7 Focusing

In section 4.1 a study for a focusing solution which maximize both the dynamic range both the photon detection efficiency has been presented. In this pre-assembling phase the correctness of the results obtained with the simulations is under test. A focusing ring with the same dimensions adopted in the simulation is kept at the same voltage of the photcathode. Thanks to the micrometric movable support istalled on the flange, the MPPC can be moved in the electric field generated by the photocathode and the focusing ring.
The high voltage supplied to the photocathode has been varied in the range [0, -8.5] kV.
For each value of the high voltage, a scan of the detected light by varying the distance of the MPPC with respect to the photocathode has been done. The

incoming light wavelengt has been set at $\lambda = 164\,nm$ and its photocurrent has been measured with the calibrated photodiode. For each position the pre-prototype readout current has been measured. The results obtained are plotted in fig. 5.12. Despite of the high voltage range for this measurement

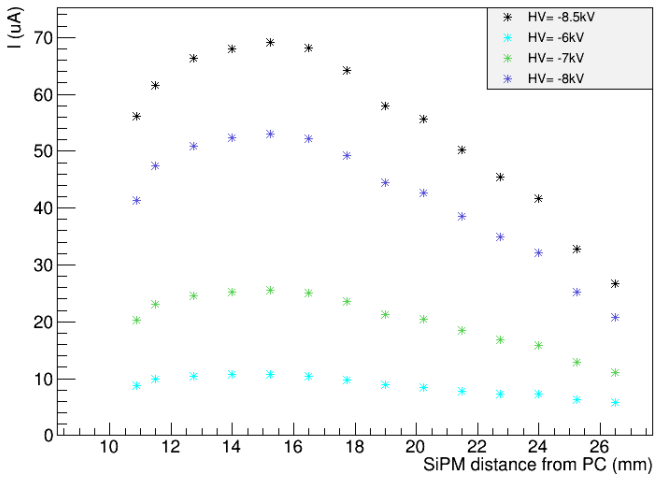

Figure 5.12: *Plot of the pre-prototype readout current vs the MPPC distance from the photocathode, at different HV values and* $\lambda = 164\,nm$.

was [0, -8.5] kV, only the results for HV ranging between -6 and -8.5 kV are plotted because the detected light for HV below those value is negligible.
From this plot a displacement of the waist (the position in which the detected light is maximized) depending on the HV can be observed.
Once explored the different solutions by varying the supplied high voltage and the distance between photocathode and MPPC, HV has been set at its maximum value. The results obtained are plotted in 5.13. As clear from the plot, it exists a plateau region of the waist, when the MPPC distance from the photocathode ranges between 15 and 17 mm. This result is in agreement with the simulations.

5.8 Linearity

A test of the response of the pre-prototype to different incoming light levels has been done. The incoming light wavelenght is set to $\lambda = 164\,nm$. The light intensity is varied by varying the opening of the slit placed after the monochromator (fig. 5.5 part: 3b) and is monitored by the calibrated photodiode.

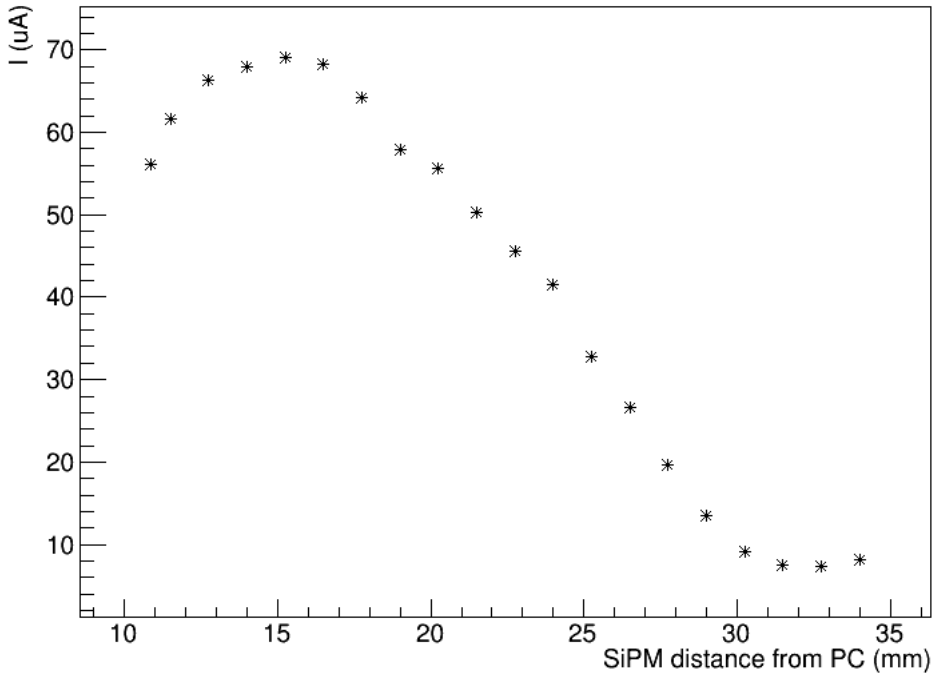

Figure 5.13: *Plot of the pre-prototype current vs the MPPC distance from the photocathode, at HV= -8.5 kV and* $\lambda = 164\,nm$.

The HV is set to -8.5 kV[3] and the MPPC distance from the photocathode is 16 mm.
The results obtained are plotted in figure 5.14. As expected, for low levels of incoming light the device shows a linear trend.

5.9 Operating point

A measurement of the pre-prototype redout current with respect to the supplied high voltage has been done. The distance between phtocathode and MPPC is 16 mm and the incoming light wavelenght is $\lambda = 164nm$. The light level for the measurement has been chosen to be in the middle of the linear range of the device by setting the slit opening as in the previous paragraph. The high voltage supplied to the photocathode and to the focusing ring has been varied in the range [0, -8.5] kV.
The results obtained are plotted in fig. 5.15. The aim of this measurement

[3]The operating point selection is presented in section 5.9.

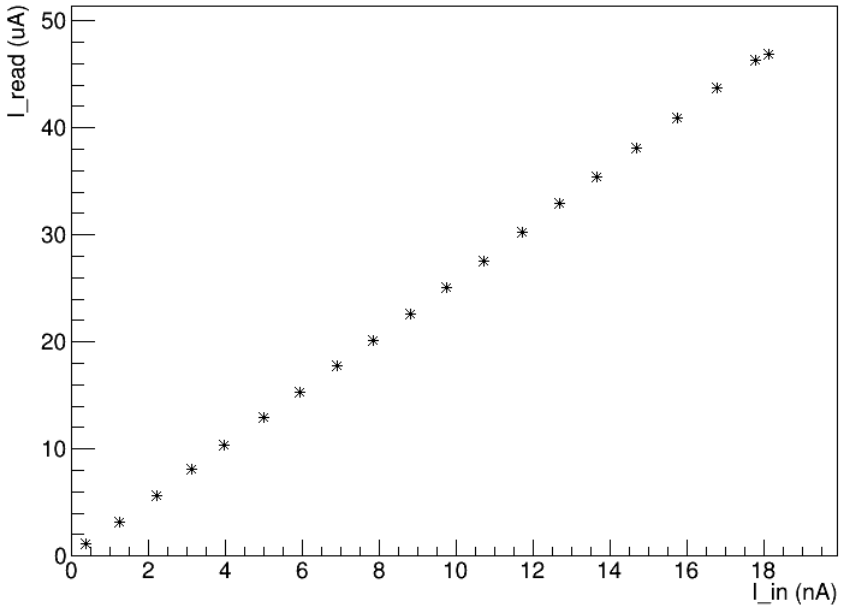

Figure 5.14: *Plot of the pre-prototype response to different incoming light levels.*

was to find the operating point of the overall device. As for the measurement on the industrial prototype (sec. 3.3.4), a plateau region starting at $\sim -3kV$ was expected. Looking at the plot 5.15 is clear that even going to -8.5 kV the plateau region is not reached. This means, as already explained in sec. 2.3 and 3.3.4, that only a fraction of the photoelectrons arriving on the MPPC surface is actually entering in the silicon bulk. Therefore, the readout current value is not at its maximum.
The only possibility to need such a high voltage to correctly operate the device is that the SiO_2 layer deposited on the MPPC surface is thicker than necessary. Since the SiO_2 thickness is a detail that is not expressed by the companies, an additional measurement has been done to clarify the unexpected result.
A measure of the thickness of the SiO_2 layer has been done by using a reflectance spectrofotometric technique. It is a non-invasive analysis technique that consists into illuminating the surface under analysis with a well known light source and recording the spectral response of the surface.
The ratio of the reflected light with respect to the incoming light is said reflectance (R [%]).
By making a scan of the reflectance of the MPPC surface with respect to the

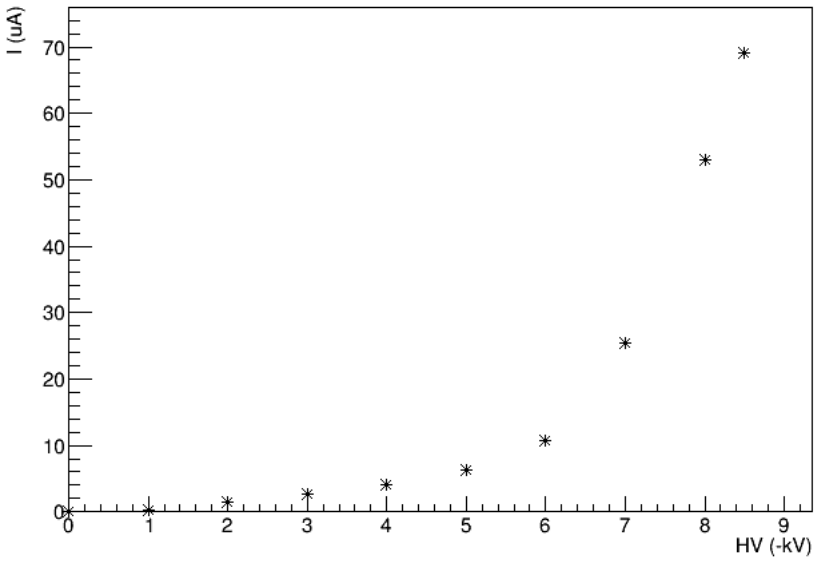

Figure 5.15: *Plot of the pre-prototype readout current with respect to the photocathode voltage.*

wavelenght, the spectral behavior of the examined surface is defined, see fig. 5.16. It is known that the spectral behavior is characteristic of the material

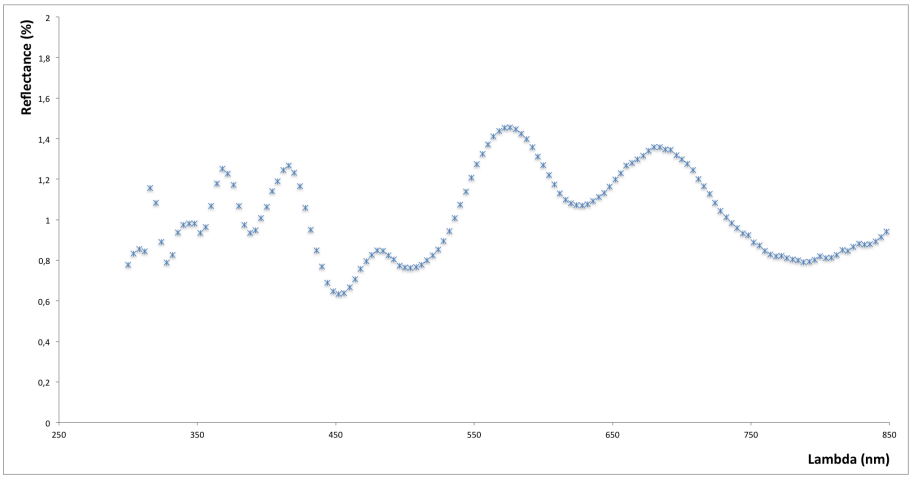

Figure 5.16: *Reflectance plot of the MPPC in the visible region.*

and it can be therefore used to determine the thickness of the SiO2 layer

with the equation:

$$t = \frac{\lambda_1 \cdot \lambda_2}{2n(\lambda) \cdot (\lambda_2 - \lambda_1)} \tag{5.2}$$

where t is the SiO_2 thickness, λ_1 and λ_2 are two consecutive peaks that can be seen in fig. 5.16 and $n(\lambda)$ is the refractive index of the SiO_2 layer at a given wavelenght. By using the eq. 5.2 combined with the results in fig 5.16, the SiO_2 layer results to be $\sim 1.2 \mu m$.
If this result is compared to the photoelectron range in Si as a function of its energy obtained with a Geant-4 based simulation (see fig. 5.17) [], it is clear that for a 1.2 μm SiO_2 layer photoelectrons with an energy of about 10 keV are necessary. With this supplementary measurement we can conclude

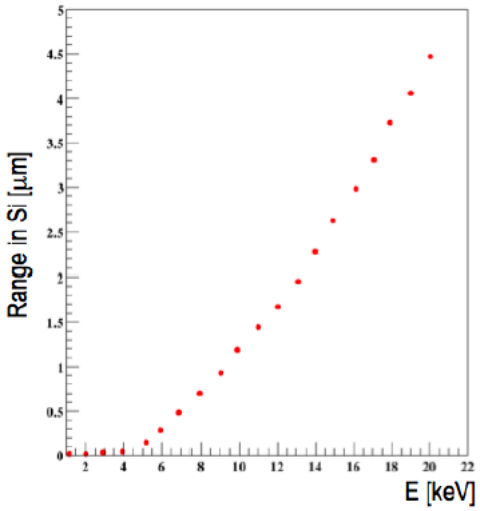

Figure 5.17: *Electron range in Silicon obtained with the Geant-4 simulation tool.*

that despite the MPPC S10943-6630 (X) has very good performances as dark rate, gain and dynamic range, it is not suitable for the VSiPMT application. Neverthless, a final measurement of the spectral responseof the pre-prototype has been done.
For this measurement the high voltage is set at its maximum (-8.5 kV) and the MPPC distance from the photocathode is kept at 16 mm. The intensity of the incoming light is set in the middle of the linear range of the device and is measured by the calibrated photodiode. The results are shown in figure 5.18. The spectral response of the pre-prototype is as expected. It is evident the first cut-off at $\sim 160\, nm$ due to the quartz window and also the second one at $\sim 200\, nm$ that is proper of the CsI photocathode. Despite of the

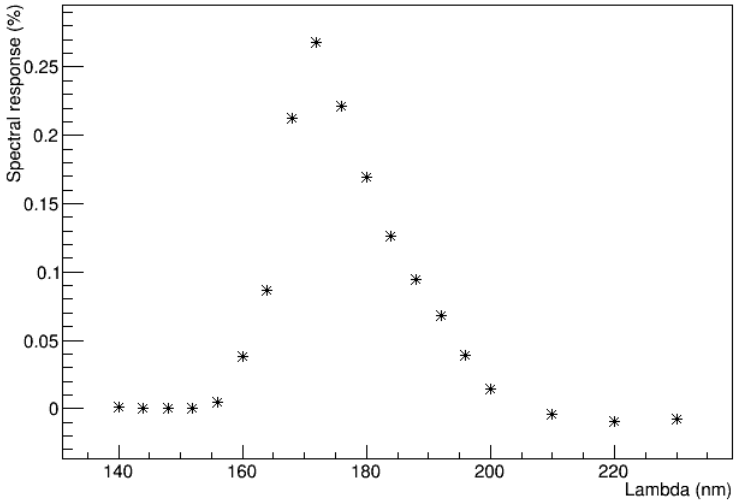

Figure 5.18: *Plot of the preprototype spectral response.*

degradation of the photocathode and the unsuitableness of the MPPC, it has been possible to determine the general characteristics of the preprototype. These will be adopted as benchmark for the final assembly of the VSiPMT.

5.10 New developments

The reflection-mode VSiPMT

During the pre-prototyping phase a new configuration of the overall device has been tested, taking advantage of the mobility of the several parts which compose the VSiPMT.

The idea is to use the photocathode in reflection mode in order to have a higher quantum efficiency, indeed during the tests on different samples of photocathode (see section 4.3.3) the quantum efficiency of the same sample was measured both in reflection that in transmision mode. As expected, even if the photocathode film is very thin the quantum efficiency is higher in reflection mode than in transmission, see fig. 5.19[35]. In figure 5.20 there are shown the conceptual designs of both the reflection and transmission mode VSiPMT. On the right side of the picture there is the conceptual design of the standard configuration of the VSiPMT, extensively described in this thesis. On the left side there is the new configuration. In this case the SiPM is directely mounted on the entrance window and faces the photocathode that acts in reflective mode. In the section 5.3 the possibility of having

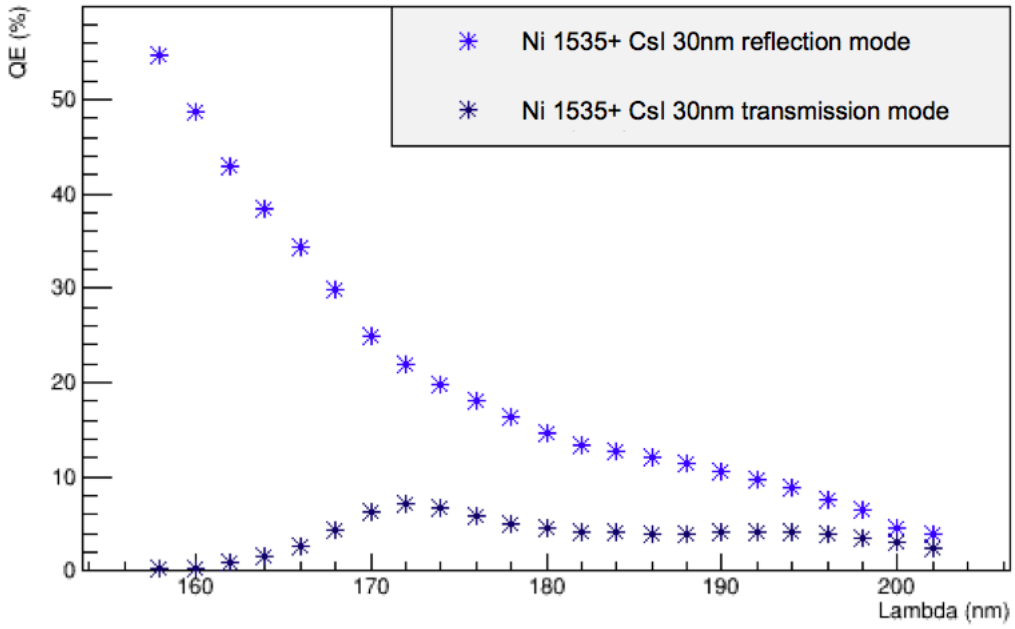

Figure 5.19: *Quantum efficiency plot of the 1535 sample in reflection and transmission mode.*

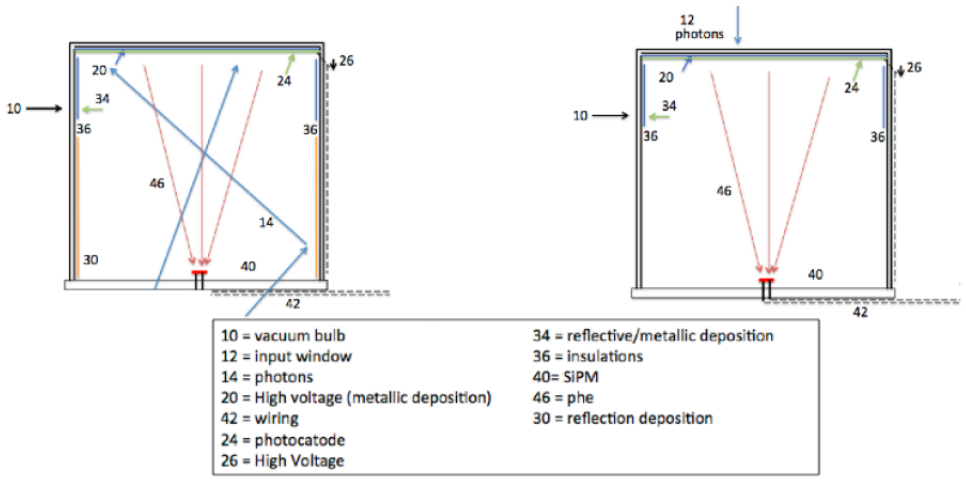

Figure 5.20: *LEFT: Reflection mode VSiPMT. RIGHT: Transmission mode VSiPMT.*

prepulses generated by photons that are not absorbed in the photocathode was debated. In this new configuration this possibility is expected to become negligible, since the photons come from behind the SiPM.

The structure in fig 5.4 has been readapted to obtain a preprototype of the reflection mode device, see fig. 5.21. The MPPC is mounted on a black

Figure 5.21: *Top and side view of the pre-prototype in reflection mode configuration.*

teflon fork at 16 mm distance from the photocathode. The fotocathode and the focusing ring both face the incoming light direction and are kept at their maximum voltage (-8.5 kV).
Measurements of the linearity and of the photon detection efficiency with respect to the wavelenght have been done. In fig. 5.22 the readout current with respect to the high voltage is plotted. In the plot the shadow area due to the teflon fork and the MPPC cables is not taken into account. This means that the values in figure are an underestimation of the real ones, as a confirmation of an expected higher values with respect to the ones measured in transmission mode (fig. 5.15). In figure 5.23 a plot of the spectral response of the reflection-mode preprototype with HV = -8.5 kV has been done. As evident, being in reflection mode entails not only a higher efficiency with respect to the transmission mode configuration (see fig. 5.18) but it also allows to cover larger range of wavelenght since there isn't any cut-off due to the window material. Figure 5.24 shows the linearity plot of the reflection mode VSiPMT pre-prototype. The high voltage was set to -8.5 kV and the $lambda = 164\,nm$. Also in this case, as for transmission mode VSiPMT pre-prototype, a linear trend of the readout current is observed for low levels of incoming light.

The diamond photocathode

The CsI is a highly hygroscopic material, as already said above. This

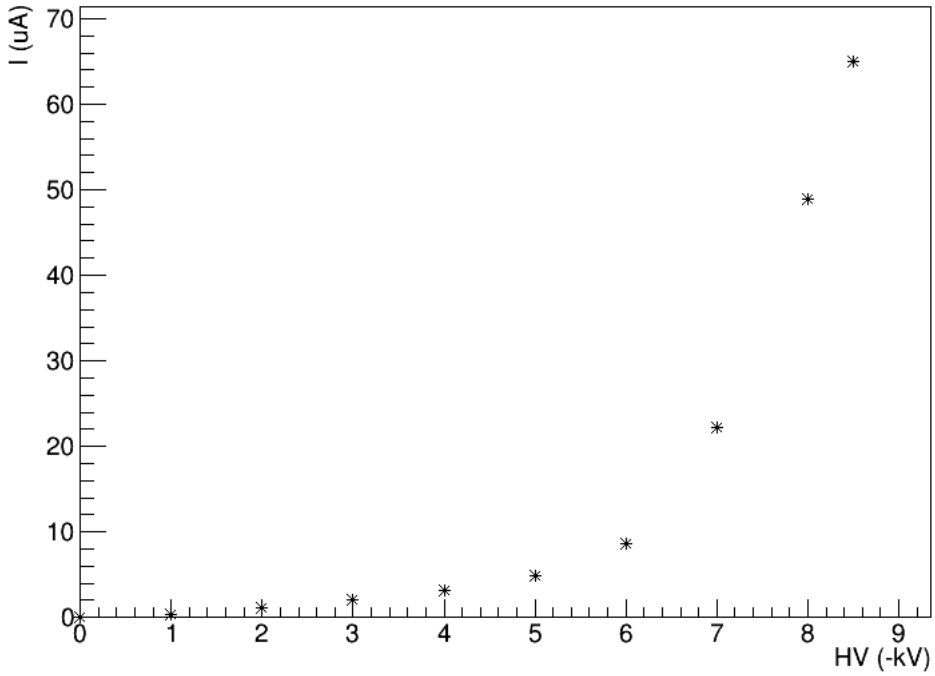

Figure 5.22: *Readout current vs HV plot of the reflection mode VSiPMT pre-prototype, with* $\lambda = 164\,nm$.

characteristic involves the necessity to handle the photocathode in an environment with a controlled humidity. This is not always possible, particularly during the tests. As a consequence a degradation of the film and so of its performances in terms of quantum efficiency can occur, as shown in section 5.4.

A new solution for a fully air transportable photocathode is under study in parallel with the realization of the first VSiPMT with 25 mm diameters photocathode.

This new solution consists in the realization, in collaboration with the CNR seat in Bari, of an highly efficient and stable photocathodes based on photoelectron emission from NEA surface of hydrogenated nanodiamond (ND) particles [36], [37]. The idea, patented by the University of Bari and CNR, is to apply a pulsed spray technique to deposit layers on a selected substrate starting from ND powder dispersed in a solvent. The advantage into using sprayed ND compared to CsI, is not only the higher QE and its stability at air exposure, but also the capability of NEA diamond to enhance the efficiency more markedly toward the visible region.

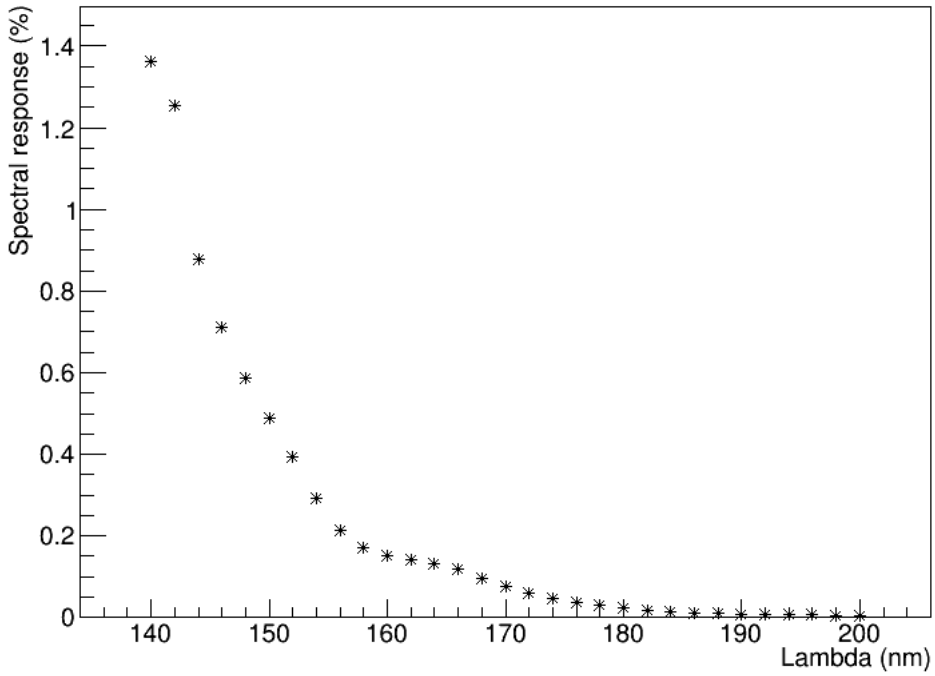

Figure 5.23: *Spectral response plot of the reflection mode VSiPMT pre-prototype.*

Up to now, only three samples of ND photocathodes have been prepared in the CNR-Bari laboratories for the VSiPMT application purpose. They have been tested both in reflection and in transmission mode. In fig. 5.25 and 5.26 a quantum efficiency plot of the ND photocathodes both in reflection both in transmission mode is shown. As for CsI, also here the reflection mode exhibits better performances with respect to the transmission mode. In this case, in addition to the presence of the entrance window cut-off there are two more contributions since this was a first costless attempt for a transmission mode ND photocathode:

1. the substrates used for the photocathode depositionhave been recovered by the samples deposited during the study for the optimization of the conductive layer so they are not optimized;

2. the powder used consists in ND particles with a diameter of 250 nm, far away from a fair thickness in case of a uniform covering.

The latter point is particularly important for the transmission mode photocathodes. The ND particles size should be lower or comparable with the

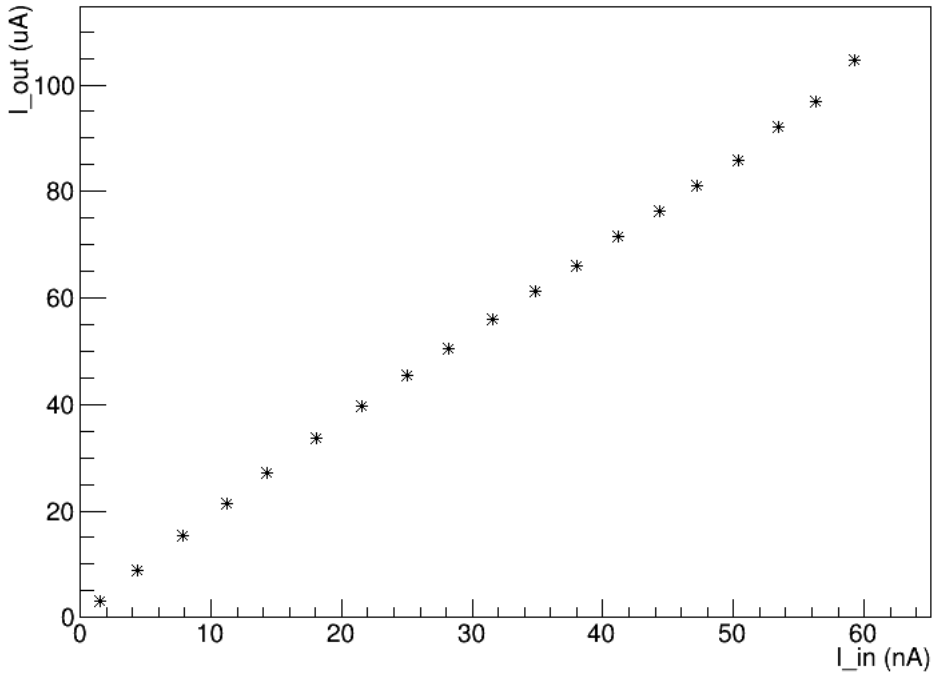

Figure 5.24: *Linearity plot of the reflection mode VSiPMT pre-prototype.*

diffusion length of the photoelectrons so that their thermalization in the bottom of the conduction band is at the surface material, where they can escape for the NEA character.
This point is currently under study and will be analyzed more extensively soon.

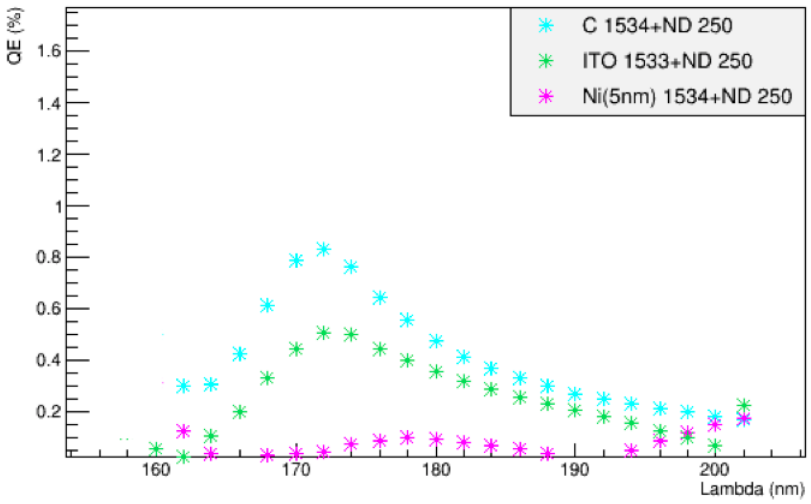

Figure 5.25: *Quantum efficiency of the ND photocathodes in transmission mode.*

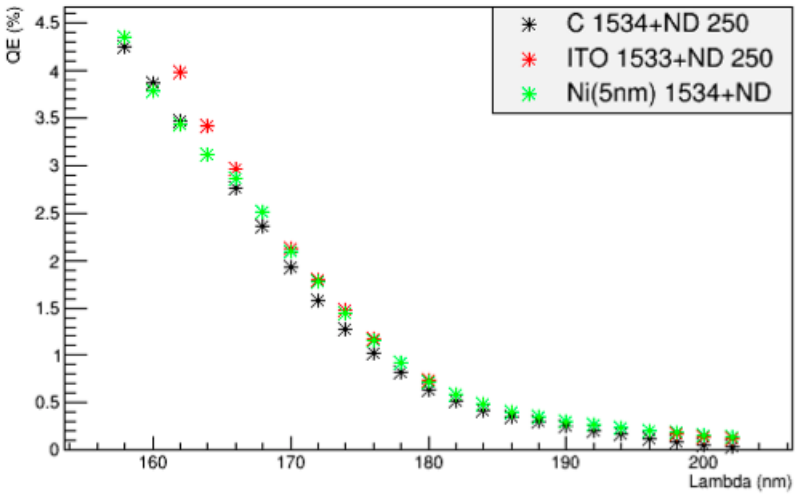

Figure 5.26: *Quantum efficiency of the ND photocathodes in reflection mode.*

Conclusions

The VSiPMT Project born in the University of Naples in 2007 as a valiant alternative to PMTs. The simple substitution of the dynode chain with a SiPM allows to reach a very high gain totally provided by the pixels working in geiger mode. This has many advantages, such as: excellent photon counting, high gain with low voltage, negligible power consumption, high speed, compactness and simplicity.
The project went on with a theoretical study of feasibility combined with Geant4-based simulations to find the range of the electrons in the SiPM.
The first proof of feasibility arrived in 2012, when the response of a special SiPM was tested with an electron beam extracted at the TTT3 accelerator available in the Physics Department of the University of Naples.
The results obtained convinced Hamamtsu Photonics, a world leader company in photodetector manufacturing, to realize for us two VSiPMT prototypes to start to explore the potentialities of the device.
The characterization of the first two prototypes of VSiPMT put up exceptionally encouraging results. The devices exhibit outstanding properties and performances beyond expectations. The substitution of the dynode chain of standard PMTs with a SiPM slashed the power consumption of the device and at the same time considerably improved the resolution on the single photoelectron response, the peak to valley ratio and the TTS.
Neverthless, both the prototypes pointed out a dynamic range shorter than expected, due to a wrong focusing. Actually, to be precise it's necessary to say that no dedicated study has been performed about focusing. In fact, the prototypes under test have been realized with the primary aim of testing the working principle of the device and hence its feasibility.
So at the end of these characterizations we owned two devices with amazing resolution, photon counting capabilities and very fast response. Neverthless, on the other side, the two devices were no usable because of the small size (3 mm diameter photocathode) and the reduced dynamic range.
Anyway there was plenty of room to improve these two features. Indeed, those were the starting point for the realization of a new generation of

VSiPMTs. For this purpose was done a SiPM census of different companies and series. A SiPM with a larger number of pixels (striking a balance with the fill factor) was adopted. In addition, SimION-based simulations were done to find an optimized focusing for the maximization of the effective number of fired SiPM cells.
Finally, this last year was dedicated to the study and realization of a semitransparent photocathode to assemble the VSiPMT prototype. This activity was conducted at the deposition facility of the CNR and Physics Department in Bari. Many parameters were in the running, but at the end of November was found a very good configuration of materials and thicknesses in orther to obtain a high quantum efficiency semitransparent photocathode.
Once that everything was ready all the parts (photocathode, focusing ring and SiPM) have been assembled together in a manufactured adjustable configuration that we called pre-prototype. This pre-prototype have been tested in February in the DaΦne Light Facility at LNF (Frascati National Laboratories). The measurement on the pre-prototype are aimed at testing the reliability of the simulations for the focusing. The results of the test were good in terms of focusing. The measured distance of the SiPM from the photocathode that maximize the number of fired pixels is in agreement with the simulations.
Unfortunately, this session of measurements pointed out that the selected SiPM was not adapted for the VSiPMT application since an antireflective layer thicker than necessary was deposited on the Silicon. This entails the necessity of photoelectrons with an energy, and so an operating high voltage, higher than desired.
Although the high voltage supplied to the photocathode was higher than desired other tests have been done to explore the overall behaviour of the device. The most important result obtained is expressed in fig. 5.11 where is possible to see the difference in the readout current when the photocathode is off and when the high voltage is supplied. This difference, concentrated in the region of sensitivity of the photocathode, means that the exceeding current is due to photoelectrons coming from the photocathode. This represent a very significative milestone in the project because it prooves that for the first time the sensitive area of the SiPM has been enlarged of more tha 50 times and, in addition, the dark counts rate remains that typical of a single SiPM. This is equivalent to reduce the dark-rate/mm^2, that up to now has been one of the main issue for the SiPM manufacturers.
A usable version of the 25 mm diameter VSiPMT will be soon assembled and tested to be compared to an equivalent PMT.

Technological impact

The VSiPMT Project is aimed at the realization of an innovative high-gain, silicon-based photodetector we invented.

The substitution of the dynode chain of standard PMTs with a SiPM would slash the power consumption of the device and at the same time would considerably improve the resolution on the single photoelectron response, the peak to valley ratio and the TTS.

Photodetectors performances represent a critical issue in the current generation of high-energy astroparticle physics experiments, aimed at the study of very high-energy (GRB, AGN, SNR) or extremely rare phenomena (dark matter, proton decay, zero neutrinos-double beta decay, neutrinos from astrophysical sources).

Many experiments in this rapidly emerging field are based on the detection of the Cherenkov or fluorescence light produced after the passage of charged particles through transparent media like air, water or ice. For these applications, the quality of the experimental results is crucially related to the performances of the adopted photodetectors, for which high efficiency and photon counting capability are mandatory. Moreover, the use of such a device with negligible power consumption, would be particularly appropriate to harsh environments experiments such as: underwater, underice and space experiments. Thus, with such features this device is expected to represent a real breakthrough in the field of photodetectors and it would represent a solid solution for the next generation experiments in astroparticle physics research.

In addition, an enormous advantage from this device will be taken by the medical field, with the possibility to realize a new generation of operating and diagnostic instrumentation like in PET, medical equipment for physical check-ups and diagnosis as in-vitro inspection (Radioimmunoassay and Enzyme immunoassay, as well as luminescent, fluorescent, Chemiluminescent Immunoassay, Laser Microscopy).

Moreover, the development of VSiPMT will push further also the development of SiPM technology. Indeed, to improve the VSiPMT performances the following points need to be improved: the shape optimization of the SiPM (to encrease the photoelectron collection efficiency and reduce the dark count rate), the reduction of the SiO_2 layer for reducing the necessary voltage between the photocathode and the silicon detector, the optimization of the pixel size. Since Hamamatsu already showed a great interest in this project and this R&D path, could be interesting to arrange a consortium of european companies (PMT, SiPM and getters producers) to start a mass production for the next generation of astroparticle physics experiments both in space and on heart.

Bibliography

[1] Iams H., Salzberg B. The secondary emission phototube. *Radio Engineers, Proceedings of the Institute of*, 23(1):55–64, 1935.

[2] Zworykin V., Morton G., Malter L. The secondary emission multiplier-a new electronic device. *Radio Engineers, Proceedings of the Institute of*, 24(3):351–375, 1936.

[3] Engstrom R. et al. Rca photomultiplier manual. *RCA Electronic Components, Harrison, NJ*, 1970.

[4] Einstein A. *A Heuristic Viewpoint Concerning the Production and Transformation of Light*. 1929.

[5] Saleh B. Mc teich fundamentals of photonics, 1991.

[6] Hamamatsu Photonics K. Photomultiplier tubes: Basics and applications. *Edition 3a*, 2006.

[7] Enterprises E. Understanding photomultipliers, 2011.

[8] Saleh B. E., Teich M. C. Semiconductor photon detectors. *Fundamentals of Photonics*, pages 644–695, 2007.

[9] Miller S. Ionization rates for holes and electrons in silicon. *Physical Review*, 105(4):1246, 1957.

[10] Hamamatsu Photonics K., et al. Opto-semiconductor handbook.

[11] Avalanche photodiode, a user guide, understanding avalanche photodiode for improving system performance. URL `http://www.excelitas.com/downloads/app_apd_a_user_guide.pdf`.

[12] McKay K., McAfee K. Electron multiplication in silicon and germanium. *Physical Review*, 91(5):1079, 1953.

[13] Barbarino G., Mollo C. M., Vivolo D., De Rosa G., de Asmundis R., Russo S. *Silicon photo multipliers detectors operating in geiger regime: an unlimited device for future applications*. INTECH Open Access Publisher, 2011.

[14] Photonics K. H. Photomultiplier tube handbook. *Electron Tube Division*, 2006.

[15] Winston R., O'Gallagher J. Nonimaging concentrators (optics). In Meyers R. A., editor, *Encyclopedia of Physical Science and Technology (Third Edition)*, pages 507 – 522. Academic Press, New York, third edition edition, 2003. ISBN 978-0-12-227410-7. doi: http://dx.doi.org/10.1016/B0-12-227410-5/00483-X. URL `http://www.sciencedirect.com/science/article/pii/B012227410500483X`.

[16] Piemonte C. Sipm technology at fbk. *IPRD10, Siena*, 2010.

[17] BARBARINO G. Single-photons count device based on photocathode and geiger solid-state technology for the multiplication of photoelectrons, January 15 2015. URL `http://www.google.com/patents/WO2015004689A1?cl=en`. WO Patent App. PCT/IT2014/000,174.

[18] Barbarino G., De Asmundis R., De Rosa G., Fiorillo G., Gallo V., Russo S. A new high-gain vacuum photomultiplier based upon the amplification of a geiger-mode p–n junction. *Nuclear Instruments and Methods in Physics Research Section A: Accelerators, Spectrometers, Detectors and Associated Equipment*, 594(3):326–331, 2008.

[19] Sommer A. H. Brief history of photoemissive materials. In *SPIE's 1993 International Symposium on Optics, Imaging, and Instrumentation*, pages 2–17. International Society for Optics and Photonics, 1993.

[20] Spicer W. E., Herrera-Gomez A. Modern theory and applications of photocathodes. In *SPIE's 1993 International Symposium on Optics, Imaging, and Instrumentation*, pages 18–35. International Society for Optics and Photonics, 1993.

[21] Spicer W. Negative affinity 3–5 photocathodes: Their physics and technology. *Applied physics*, 12(2):115–130, 1977.

[22] Sommer A. H. Photoemissive materials. preperation, properties and uses. *Huntington: Krieger, 1980*, 1, 1980.

[23] Barbarino G., de Asmundis R., De Rosa G., Mollo C. M., Vivolo D. Vsipmt for underwater neutrino telescopes. *Nuclear Instruments and Methods in Physics Research Section A: Accelerators, Spectrometers, Detectors and Associated Equipment*, 725:162–165, 2013.

[24] Joram C., Rudge A., Séguinot J. Proof of principle of g-apd based hybrid photodetectors. *Nuclear Instruments and Methods in Physics Research Section A: Accelerators, Spectrometers, Detectors and Associated Equipment*, 621(1):171–176, 2010.

[25] Barbato F. Studio della risposta di un sipm agli elettroni per la verifica della fattibilità di un nuovo fotomoltiplicatore ibrido a semiconduttore ad alto guadagno. Master's thesis, University of Naples *Federico II*, July 2012.

[26] Barbarino G. et al. Proof of feasibility of the vacuum silicon photomultiplier tube (vsipmt). *Journal of Instrumentation*, 8(04):P04021, 2013.

[27] Barbarino G. et al. A new generation photodetector for astroparticle physics: The {VSiPMT}. *Astroparticle Physics*, 67:18 – 25, 2015. ISSN 0927-6505. doi: http://dx.doi.org/10.1016/j.astropartphys.2015.01.003. URL `http://www.sciencedirect.com/science/article/pii/S0927650515000134`.

[28] Hamamatsu Photonics K., et al. S10943-3050cs datasheet, 2013.

[29] Anderson D., Kwan S., Peskov V. Csi and some new photocathodes. *Nuclear Instruments and Methods in Physics Research Section A: Accelerators, Spectrometers, Detectors and Associated Equipment*, 343(1):109–116, 1994.

[30] Anderson D., Kwan S., Peskov V. Csi photocathode qe and a simple production technique. *Nuclear Instruments and Methods in Physics Research Section A: Accelerators, Spectrometers, Detectors and Associated Equipment*, 326(3):611–612, 1993.

[31] Valentini A., Nappi E., Nitti M. Influence of the substrate reflectance on the quantum efficiency of thin csi photocathodes. *Nuclear Instruments and Methods in Physics Research Section A: Accelerators, Spectrometers, Detectors and Associated Equipment*, 482(1):238–243, 2002.

[32] Akkerman A., Gibrekhterman A., Breskin A., Chechik R. Monte carlo simulations of secondary electron emission from csi, induced by 1–10

kev x rays and electrons. *Journal of applied physics*, 72(11):5429–5436, 1992.

[33] Braem A., Joram C., Piuz F., Schyns E., Seguinot J. Technology of photocathode production. *Nuclear Instruments and Methods in Physics Research Section A: Accelerators, Spectrometers, Detectors and Associated Equipment*, 502(1):205–210, 2003.

[34] Balerna A. et al. Dafne-light infn-lnf synchrotron radiation facility. In *SRI 2009, 10TH INTERNATIONAL CONFERENCE ON RADIATION INSTRUMENTATION*, volume 1234, pages 285–288. AIP Publishing, 2010.

[35] Lu C., McDonald K. Properties of reflective and semitransparent csi photocathodes. *Nuclear Instruments and Methods in Physics Research Section A: Accelerators, Spectrometers, Detectors and Associated Equipment*, 343(1):135–151, 1994.

[36] Nitti M., Nappi E., Valentini A., Bénédic F., Bruno P., Cicala G. Progress in the production of csi and diamond thin film photocathodes. *Nuclear Instruments and Methods in Physics Research Section A: Accelerators, Spectrometers, Detectors and Associated Equipment*, 553(1): 157–164, 2005.

[37] Nitti M. et al. Performance analysis of poly-, nano-and single-crystalline diamond-based photocathodes. *Nuclear Instruments and Methods in Physics Research Section A: Accelerators, Spectrometers, Detectors and Associated Equipment*, 595(1):131–135, 2008.